UNIVERSIDADE FEDERAL DE MINAS GERAIS

Programa de Pós-Graduação em Engenharia Metalúrgica, Materiais e de Minas

Dissertação de Mestrado

Partição de deformação em aços *dual-phase*

Autor: Pedro Henrique Silva

Orientador: Prof. Pedro Henrique Rodrigues Pereira

Setembro/2022

Pedro Henrique Silva

Partição de deformação em aços *dual-phase*

Dissertação apresentada ao Programa de Pós-Graduação em Engenharia Metalúrgica, Materiais e de Minas da Escola de Engenharia da Universidade Federal de Minas Gerais como requerimento para obtenção do grau de Mestre em Engenharia Metalúrgica, Materiais e de Minas.

Área de concentração: Metalurgia física e de transformação.

Orientador: Prof. Pedro Henrique Rodrigues Pereira.

Belo Horizonte

Universidade Federal de Minas Gerais

Escola de Engenharia

2022

Silva, Pedro Henrique.
S586p Partição de deformação em aços *dual-phase* [recurso eletrônico] / Pedro Henrique Silva – 2022.
1 recurso online (113 f.: il., color.): pdf.

Orientador: Pedro Henrique Rodrigues Pereira.

Dissertação (mestrado) - Universidade Federal de Minas Gerais, Escola de Engenharia.

Apêndice: f. 113.
Bibliografia: 99-112.
Exigências do sistema: Adobe Acrobat Reader.

1. Engenharia Metalúrgica - Teses. 2. Aço de alta resistência – Teses. 3.Método dos elementos finitos. – Teses. I. Pereira, Pedro Henrique Rodrigues. II. Universidade Federal de Minas Gerais. Escola de Engenharia. III. Título.

CDU: 669(043)

Ficha catalográfica elaborada pela Bibliotecária Letícia Alves Vieira - CRB-6/2337

Biblioteca Prof. Mário Werneck - Escola de Engenharia da UFMG

FOLHA DE APROVAÇÃO

UNIVERSIDADE FEDERAL DE MINAS GERAIS
ESCOLA DE ENGENHARIA
Programa de Pós-Graduação em Engenharia Metalúrgica, Materiais e de Minas

A dissertação intitulada **"Partição de Deformação em Aços Dual-phase"**, área de concentração: Metalurgia Física e de Transformação, apresentada pelo candidato **Pedro Henrique Silva**, para obtenção do grau de Mestre em Engenharia Metalúrgica, Materiais e de Minas, foi aprovada pela comissão examinadora constituída pelos seguintes membros:

Dr. Pedro Henrique Rodrigues Pereira
Orientador (UFMG)

Dr. Paulo Roberto Cetlin
(UFMG)

Dr. Paulo José Modenesi
(UFMG)

Dr. Geraldo Lúcio de Faria
(UFOP)

Dr. Dagoberto Brandão Santos
(UFMG)

Coordenador do Programa de Pós-Graduação em Engenharia Metalúrgica, Materiais e de Minas/UFMG

Belo Horizonte, 29 de setembro de 2022

UNIVERSIDADE FEDERAL DE MINAS GERAIS

Programa de Pós-Graduação em Engenharia Metalúrgica, Materiais e de Minas

Master's degree dissertation

Strain partitioning in dual-phase steels

Author: Pedro Henrique Silva

Advisor: Prof. Pedro Henrique Rodrigues Pereira

September/ 2022

Pedro Henrique Silva

Strain partitioning in dual-phase steels

Master's degree thesis presented to the Graduate Program of Metallurgical, Materials and Mines Engineering of the School of Engineering of the Federal University of Minas Gerais, as requirement to the Master's degree in Metallurgical, Materials and Mines Engineering.

Concentration field: Physical and Transformation Metallurgy.

Advisor: Prof. Pedro Henrique Rodrigues Pereira.

Belo Horizonte

Universidade Federal de Minas Gerais

Escola de Engenharia

2022

AGRADECIMENTOS

A realização deste trabalho não seria possível sem a ajuda de grandes pessoas e grandes profissionais.

Agradeço ao professor, e amigo, Pedro H. Rodrigues Pereira pela orientação, paciência, motivação, por ser um guia e uma fonte de inspiração.

Ao professor Paulo Roberto Cetlin pela oportunidade de integrar seu grupo de pesquisa, pelos conselhos, ensinamentos e colaboração ao longo deste trabalho.

Ao professor Dagoberto Brandão Santos, por todo o apoio na preparação de amostras e realização das análises metalográficas, pela colaboração no desenvolvimento do trabalho, paciência e disposição nas muitas vezes que precisei de ajuda.

À professora Berenice Gonzalez, pela assistência na realização dos ensaios mecânicos além da abordagem inspiradora em sala de aula.

Ao professor Witor Wolf, pela prontidão e apoio nas medições de ultramicrodureza.

Aos técnicos Thiago e Leonardo pelo apoio na realização dos ensaios mecânicos.

À Patrícia, pelas imagens e análises no MEV impecáveis, pelo humor, carisma e excelente companhia.

Aos amigos e companheiros de laboratório Davi, Renata, Guilherme, Carol, Raphael, Natanael, Olavo, Yasmim, Lucas, Adriano, Diogo, Victor, Malu, Nício e Anderson.

À Nayara, pela ajuda em providenciar o material de estudo deste trabalho.

Aos amigos pesquisadores André, João Victor, Johne e Charles.

À minha irmã, Jéssica, pelo apoio incondicional ao longo do percurso.

Aos meus pais, João Pedro e Neide, pelos pilares que me ajudaram a erguer ao longo da vida.

À minha companheira, Melaine, por tornar o trajeto mais leve e por me inspirar a ser uma pessoa melhor.

Por fim, agradeço à FAPEMIG pelo financiamento, CAPES, CNPq e a todos aqueles que constituem a UFMG e o PPGEM, cujo trabalho provê uma estrutura de excelência para realização da pesquisa mesmo diante de cenários adversos.

RESUMO

O desenvolvimento de ligas avançadas demanda frequentemente a combinação de alta resistência mecânica, para performance, e boa ductilidade para suportar o processamento nas etapas subsequentes à fabricação do material até a geometria final. Importantes avanços têm sido obtidos ao longo das últimas décadas através da combinação de fases com propriedades diferentes como os aços *dual-phase*, compostos fundamentalmente pelas fases ferrita e martensita. A heterogeneidade microestrutural impõe a partição da tensão e da deformação quando o material é submetido a algum carregamento. Nisto se encontram ambos o trunfo e a maior vulnerabilidade dessa combinação: a excelente capacidade de encruamento do material e a ocorrência de falhas prematuras em certas condições de carregamento, como evidenciado na literatura através de ensaios de expansão de furo e operações de estampagem de flanges. Tendo em vista questões relativas ao comportamento de ligas multifásicas e a relação entre os fenômenos associados à deformação em diferentes níveis estruturais, propôs-se avaliar a evolução da deformação de um aço *dual-phase* sob compressão em estado plano de deformação. A metodologia adotada é de caráter integrado, combinando técnicas experimentais (MEV, microdureza, ultramicrodureza, EBSD) e simulação por elementos finitos de um campo microestrutural. A análise foi conduzida de modo a elucidar os fenômenos em diferentes escalas sob a perspectiva da natureza fractal da deformação em corpos de prova submetidos a determinados níveis de deformação equivalente (0,08, 0,15, 0,50, 1,05 e 1,65). Evidenciou-se a formação de bandas de deformação no interior dos grãos, arranjo celular de discordâncias e bandas de cisalhamento em nível micro e macroestrutural. Avaliou-se a abordagem numérica da compressão de uma região da microestrutura situando-a em uma escala de análise apropriada e estabelecendo a interligação com os experimentos. Como consequência do caminho de deformação escolhido, evidenciou-se indicações da ocorrência de refino de grão, via EBSD, por deformação severa localizada da estrutura bifásica, indicada pelo modelo numérico de elementos finitos. Esses resultados elucidam questões importantes sobre a metodologia de estudo da partição de deformação e o comportamento mecânico de aços dual-phase sob alta deformação após um caminho de deformação monotônico e não cíclico.

Palavras-chave: Aços dual-phase; compressão em estado plano de deformação; método dos elementos finitos; volumes representativos; partição de deformação.

ABSTRACT

The tailoring of new alloys often requires improvement in strength, for performance, and ductility to support mechanical processing until the final shape is achieved. Important advances have been obtained in the last decades by designing alloys which combine phases with distinct properties, such as the dual-phase steels, fundamentally composed of ferrite and martensite. The microstructural heterogeneity imposes stress and strain partitioning when the material is submitted to loading. This results in both the greatest accomplishment and detriment of these alloys: the excellent strain hardening capability and the premature failure at certain loading conditions, as evidenced in the literature by means of hole-expansion testing and stretch-flange forming operations. Considering the mechanical behavior of multiphase alloys and the interlacing of strain related phenomena in different scales, we investigate the strain progression of a DP steel under plane strain compression. The method employed in this study is based on a coupled approach, combining experimental (SEM, microhardness, ultramicrohardness, and EBSD) and finite element method simulation of a representative microstructural field of view. The analysis was conducted in a way that elucidates strain related phenomena in different scales under a fractal perspective of specimens submitted to certain levels of equivalent strain (0.08, 0.15, 0.50, 1.05, 1.65). Strain bands and a cellular dislocation arrangement were observed within the grains. Crossing several grains, shear bands were noted in a micro-scale, and larger shear bands of a different origin were observed in a larger scale of analysis. With this empirical background, the numerical approach of a microstructural field of view was discussed and situated in terms of scale. Plane strain compression allowed considerably higher strain levels to be obtained than uniaxial tension. There were indications of local grain refinement by EBSD within shear bands due to local severe plastic deformation, which is suggested by the finite element numerical model. These results elucidate questions regarding the 2D-RVE finite element approach and the mechanical behavior of dual-phase steels under large strain after a monotonic non-cyclic loading path.

Keywords: Dual-phase steels; plane strain compression; finite element analysis; representative volume element (RVE); strain partitioning.

List of Figures

List of Tables

DEFINITIONS AND ABBREVIATIONS

DP	Dual phase
AHSS	Advanced high strength steel
YS	Yield strength
UTS	Ultimate tensile strength
UE	Uniform elongation
KAM	Kernel average misorientation
EBSD	Electron backscatter diffraction
SEM	Scanning electron microscope
SE	Secondary electrons
FE	Finite element
FEM	Finite element method
VE	Volume element
RVE	Representative volume element
MVF	Martensite Volume Fraction
GND	Geometrically necessary dislocation
df	Ferrite grain size
dm	Martensite island size
TEM	Transmission electron microscope
SPD	Severe plastic deformation

Table of Contents

1- INTRODUÇÃO

Um dos pilares do progresso humano é o desenvolvimento de materiais com propriedades físicas, químicas e mecânicas que atendam a requisitos que se tornam progressivamente mais exigentes ao longo do tempo. No tocante ao comportamento mecânico, o endurecimento por deformação é um elemento fundamental. O entendimento dos mecanismos subjacentes envolvidos nesse processo pode ser considerado um dos pilares no projeto de ligas com melhores propriedades mecânicas.

De modo geral, a busca por melhores propriedades mecânicas implica em aumento de resistência mecânica e aumento de ductilidade. O desafio é precisamente o incremento simultâneo dessas propriedades que, frequentemente, são antagônicas. Em outras palavras, é mais simples obter ganhos de resistência mecânica às custas da perda de ductilidade, e vice-versa, do que melhorar ambas as propriedades. Nas últimas décadas, esse desafio tem sido enfrentado recorrentemente através do desenvolvimento de ligas que combinam fases com propriedades mecânicas diferentes. Um exemplo disso são os aços *dual-phase*, entre outros aços avançados de alta resistência mecânica.

Aços avançados de alta resistência mecânica (da sigla em inglês AHSS, *advanced high strength steels*) são um conjunto de aços desenvolvidos pela indústria siderúrgica em resposta à crescente demanda automobilística nos quesitos de segurança veicular e economia de combustível [1]. Os aços *dual-phase* são uma família de aços AHSS constituídos (geralmente) por uma matriz ferrítica e ilhas de martensita. A combinação dessas fases é obtida a partir de composições químicas simples e processamento termomecânico [2].

Esses aços geralmente apresentam alto limite de resistência, alta razão limite de resistência por limite de escoamento, alta capacidade de encruamento comparado com aços convencionais de alta resistência mecânica, ausência de patamar de escoamento, e capacidade de endurecimento por envelhecimento estático e dinâmico [1].

Microestruturas heterogêneas, como ferrita-martensita, impõe, por natureza, complicações no entendimento da partição de tensão e deformação entre as fases. Isso é fundamental para a performance dessas ligas tanto na aplicação quanto no processamento do material até a geometria final, conforme já demonstrado sob certos caminhos de deformação [3,4], a exemplo daquele observado em operações de flangeamento de bordas [5,6]. Aços *dual-phase* costumam falhar prematuramente nessas condições [7].

Com isso em mente, estudou-se a partição de tensão e deformação em um aço *dual-phase* (DP600) através de uma abordagem integrada (empírica e numérica). A análise foi feita a partir de uma perspectiva fractal [8] com o intuito de elucidar a relação entre os fenômenos de deformação em diferentes escalas estruturais usando microscopia eletrônica de varredura, microdureza, ultramicrodureza e difração de elétrons retroespalhados (EBSD, *electron backscatter diffraction*). Arbitrou-se avaliar o caminho de deformação de compressão em estado plano de deformação para facilitar o ajuste do modelo numérico com os dados experimentais. Com o arcabouço empírico, uma análise por elementos finitos foi realizada em um campo microestrutural representativo para elucidar a partição de deformação e permitir uma avaliação crítica dessa abordagem numérica.

Esses resultados permitem um entendimento amplo da partição de deformação em microestruturas heterogêneas de aços *dual-phase* e fomentam a discussão de importantes aspectos relativos à abordagem de elementos finitos por volumes representativos.

1.1- INTRODUCTION

One of the pillars of human progress is the development of materials with physical, chemical, and mechanical properties that suit the increasing requirements for new as well as old demands and endeavors. One of the key elements regarding mechanical behavior of materials is work hardening. The understanding of the underlying phenomena can be considered one of the corner stones to materials design aiming at betterments in mechanical performance.

When it comes to mechanical performance, increase in strength and ductility is a recurrent goal. The challenge is the simultaneous improvement of both since these properties can often be improved at each other's expenses. In the last decades, this challenge has been met through the design of alloys that combine phases with contrasting mechanical properties. Examples such as the dual-phase steels can be found among the advanced high strength steels.

Advanced high strength steels (AHSS) are a set of steels developed by the steel industry in response to demands from the automotive industry regarding passenger safety and fuel economy [1]. The term dual-phase steel refers to a subset of AHSS constituted by a soft ferrite matrix and hard martensite islands. This combination of phases is obtained by simple chemical composition and thermomechanical processing [2].

Dual-phase steels generally present high ultimate tensile strength (UTS), high ultimate strength to yield strength (YS) ratio, high strain hardening characteristics compared to conventional high strength steels, absence of yield point elongation, and the capacity of being strengthened by dynamic and static strain ageing [1].

Such heterogeneous microstructures impose a challenge to understanding the partitioning of strain and stress among the constituent phases. This has implications in both the material's behavior under mechanical processing until the geometry for its usage and its ultimate performance. This heterogeneity has been demonstrated to be crucial especially under certain loading conditions [3,4], such as those of stretch-flange operations [5,6]. Dual-phase steels are known to fail in these conditions often prematurely due to the strain partitioning between ferrite and martensite [7].

In this framework, the stress and strain partitioning in a dual-phase steel (DP600) was studied using a coupled empirical-numerical approach. The analyses were performed

under a fractal perspective [8] to elucidate the interlacing of strain related phenomena in different scales using scanning electron microscopy, microhardness, ultramicrohardness, and electron backscatter diffraction. With this empirical background, 2D-based finite element simulations were performed on a representative microstructural field of view to enhance the understanding of strain progression and to allow a critical assessment regarding specificities of such numerical methodology. The strain path of plane strain compression was chosen to provide a better adjustment to the numerical model.

These results provide an enhanced understanding regarding strain partitioning which is relevant not only to dual-phase steels but to other multiphase alloys. Also, important insights regarding the RVE finite element approach were discussed and may be useful for future studies.

2- AIMS AND OBJECTIVES

This research aims to investigate the influence of strain related phenomena in different scales, or dimensions, establishing the interlacing of these phenomena on a DP600 dual-phase steel's mechanical behavior through physical testing and numerical modeling under plane strain compression using a 2D-based representative volume element (RVE) approach.

The main objectives of this research are outlined as follows:

- Microstructural characterization of the as-received DP600 steel sheets through optical and scanning electron microscopy to determine grain size, martensite volume fraction, morphology and EBSD analysis to assess micro texture of the phases and dislocation arrangement using kernel average misorientation (KAM) maps.
- Mechanical characterization through Vickers hardness and ultramicrohardness to assess mean hardness and individual phase properties in the as-received samples.
- Strain progression and individual phase hardening behavior analysis through EBSD, ultramicrohardness, and microhardness in specimens from interrupted plane strain compression tests in different strain levels.
- Numerical investigation of stress and strain partitioning using an RVE (representative volume element) approach to predict the composite flow curve from individual phase properties and critically assess the approach.

3- LITERATURE REVIEW

3.1- ADVANCED HIGH STRENGTH STEELS

The term advanced high strength steels (AHSS) refers to a group of steels widely used as thin sheets in the production of structural components for automobiles [9] due to the increased improvement in both mechanical resistance and ductility [10], enhanced formability and superior crashworthiness compared to conventional steels [1].

There are several types of steels which are considered advanced high strength steels, namely: dual-phase (DP), transformation induced plasticity (TRIP), twinning induced plasticity (TWIP), ferrite-bainite (FB), complex phase (CP), martensitic, hot-forming (HF), and quenching and partitioning (Q&P) steels. Their properties are defined by their complex microstructures, chemical composition of the phases, morphology, volume fraction, distribution, and size, as well as the stability of the metastable constituents [1].

The distinction among advanced high strength steels involves specifying both yield strength (YS) and ultimate tensile strength (UTS) usually in the format XX aaa/bbb [1], according to the World Auto Steel association, where XX refers to the type of steel, aaa is the minimum yield strength in MPa and bbb is the minimum ultimate tensile strength, also in MPa. For dual-phase steels, it is usual to use the nomenclature as DP/bbb, where bbb is the minimum ultimate tensile strength required to belong to such DP class. Figure 1 presents a representative chart relating ductility (elongation) and UTS per class of AHSS, conventional, and austenitic stainless steels.

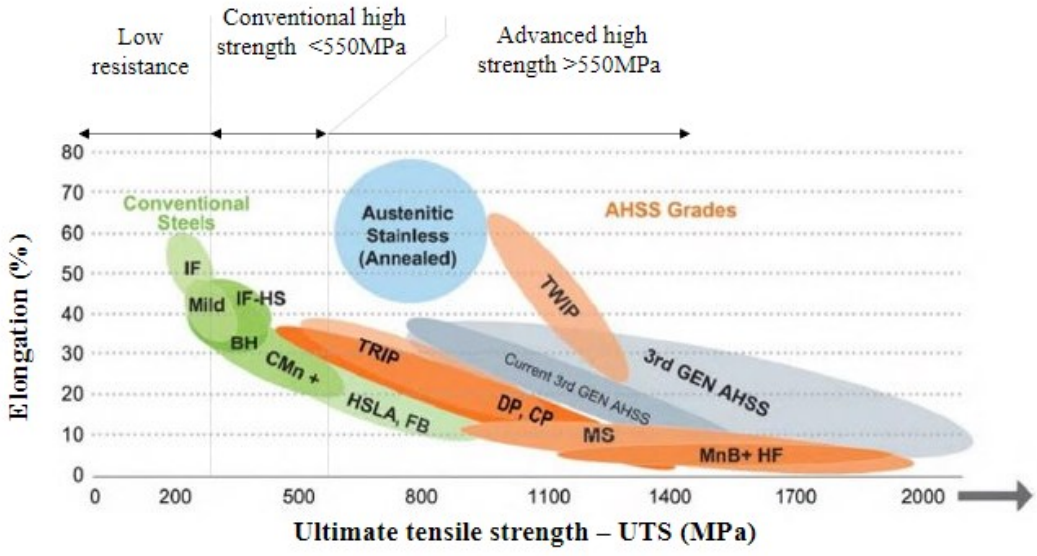

Figure 1 - Diagram: UTS x Elongation (adapted from [9] and [11]).

A brief analysis of Figure 1 shows a clear tendency of diminishing ductility with the increase of the ultimate tensile strength. One may observe the interstitial free (IF) steels in the far left of the chart presenting the highest elongations, but lowest mechanical strength (UTS). These steels contain extremely low amounts of alloying elements and are constituted by a purely ferritic structure. With increased alloying elements content and hardening mechanisms such as precipitation and solid solution hardening leads to alloys with a bit higher strength such as mild steels, which contain lower to higher volume of cementite, and high strength interstitial free steels (IF-HS). This slight increase in mechanical resistance is obtained at the expense of ductility, as it can be observed also with the bake hardened and C-Mn steels. Both the martensitic (MS) and the MnB+HF (which are boron-based hot formed alloys) steels display the highest UTS and lowest elongations and are in the far-right. It is noteworthy that most of the advanced high strength steels are dislocated towards the center of the chart, such as DP, TRIP, CP, and TWIP steels, which means that their microstructures provide a good combination of high strength and good ductility. This can be achieved through grain refinement and by the combination of different phases with distinct physical properties. Third generation AHSS, such as the quenching and partitioning (Q&P) steels [12], that are currently under development, have complex microstructures combining ferrite, martensite, and austenite.

BOUAZIZ et al. [13] present a review in which they discuss the driving forces and the development of AHSS for automotive applications. The authors highlight the demand for better crashworthiness, which translates to energy absorption capacity and anti-intrusion performance, and the demand for weight reduction to achieve lower levels of greenhouse gas emission. TAMARELLI [10], HILDITCH et al. [9] and KEELER et al. [11] also state the relevance of mass production viability and aesthetics requirements.

Regarding crashworthiness there are two main indexes which represent performance, namely: the average force (F_{avg}, Equation 1), corresponding to the energy absorption performance, and the maximal force ($F_{max,}$ Equation 2), related to the anti-intrusion performance [13]:

$$F_{avg} = K\sqrt{\sigma_{UTS}}\, x\, t^2 \tag{1}$$

$$F_{max} = K\sqrt{\sigma_{YS}}\, x\, t^{1,75} \tag{2}$$

where σ_{UTS} is the ultimate tensile strength, σ_{YS} is the yield strength, t is the thickness of the specimen and K is a geometric constant.

A brief analysis of Equations 1 and 2 reveals that both indexes can be improved by increasing UTS and YS. One may also observe that by increasing UTS and YS while reducing the thickness of the specimen may not compromise crashworthiness [13]. This insight drives the development of new alloys for the automotive industry. However, it must be emphasized the necessity to maintain or even increase formability, so that the material can be shaped to geometries which are occasionally complex for its application.

3.2- DUAL-PHASE STEELS

Dual-phase steels are a class of steels developed in the first generation of AHSS which combine high ultimate tensile strength and adequate formability for mass production [14]. These steels are produced by relatively simple thermomechanical process with relatively simple chemical composition [2]. A wide set of mechanical properties can be obtained [2] due to the presence of a relatively soft phase (ferrite) and a considerably harder phase (martensite) [14].

According to RASHID [15], this class of steels was developed in the 1960s concurrently in the United Kingdom at the British Iron and Steel Research Association and in the United States at the Inland Steel Corporation. The first aimed at developing an annealing process to obtain steels with UTS above 500 MPa. The latter aimed at producing steels with UTS greater than 1000 MPa. Still according to RASHID [15], neither of them recognized or researched the potential for improved formability, which was only triggered in the 1970s due to the driving forces discussed in the previous section.

In the following sections, some aspects of the microstructure and processing of these steels will be discussed, and an analysis of mechanical properties based on literature data will be presented.

3.2.1 - PROCESSING AND MICROSTRUCTURE

The simplest processing route to obtain a dual-phase ferrite-martensite microstructure is an inter-critical annealing (Figure 2a) to partially austenitize the material followed by a rapid cooling to transform the austenite in martensite [14]. Another possibility is the complete austenitizing followed by a controlled cooling to an inter-critical temperature, in order to allow some ferrite to form and finally quenching to transform the remaining

austenite in martensite. This route is known as step quenching (Figure 2b). A third possible route is the intermediate quenching [16–19], which consists of an annealing treatment for complete austenitization, followed by quenching and subsequent inter-critical annealing followed by another quench (Figure 2c).

The main difference among these routes is the microstructure which precedes the final quench to the ferrite-martensite dual-phase structure. It is noteworthy that in all these routes it is possible that small portions of another constituent, such as bainite or retained austenite are present.

In Figure 2, the corresponding microstructures according to the processing routes are presented. Darker areas correspond to martensitic regions, while lighter areas correspond to ferrite grains. The most refined structure can be observed in the intermediate quench route (Figure 2c). This is because martensite is heated to the intercritical phase field which provides several nucleation sites for ferrite and austenite [17,18]. In the intercritical annealing (Figure 2a), the material is heated to the intercritical region and austenite nucleation takes place on grain boundaries and triple points, where previously pearlite colonies were located. These austenitic regions transform to martensite after quenching. Finally, in Figure 2b, a blocky type of structure can be observed. In this route, a completely austenitic structure enters the intercritical phase field and ferrite starts to nucleate mostly in grain boundaries. These ferrite grains grow into the austenite grains, especially through regions with negative manganese segregation [20] and interconnectivities are created [17,18] in which case, a banded resulting microstructure can be observed.

It is interesting to note that something similar to the step-quenching route is commonly applied in the industry, in which, however, thermomechanical processing is involved [21]. Instead of a mostly dislocation free austenite, deformed grains enter the intercritical phase field. The higher density of nucleation sites favors a more refined microstructure.

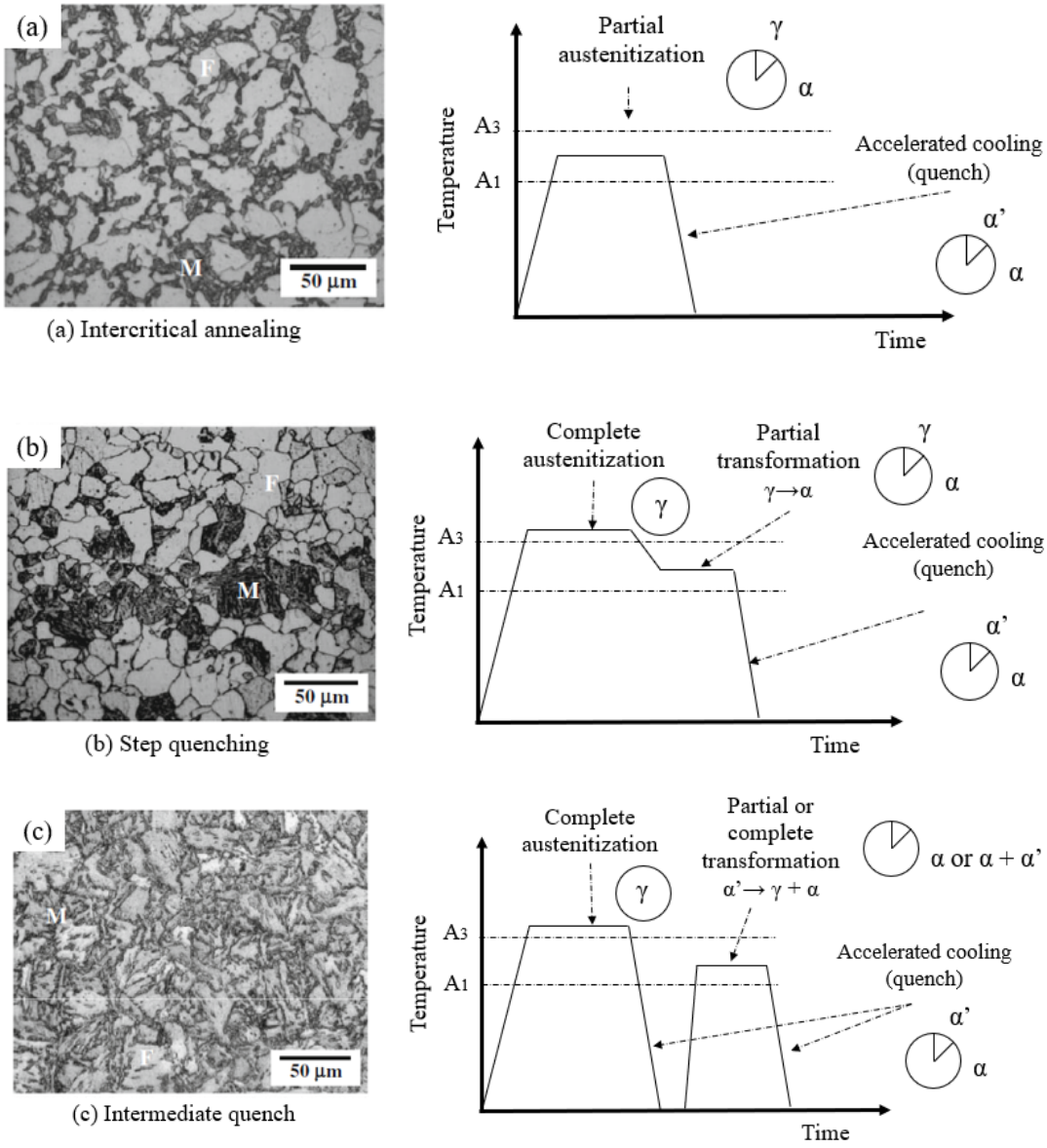

Figure 2 - Microstructure per processing route: 2a) Intermediate quench; 2b) Intercritical annealing; 2c) Step quenching (adapted from [18]).

Some of the relevant variables in dual-phase steels processing are chemical composition, annealing time, annealing temperature, heating rate (for ultra-fine-grained DP), cooling rate, and initial microstructure (microstructure right before the final treatment, which produces the dual-phase microstructures). All these variables, except for the cooling rate, will determine the microstructure which precedes the formation of the dual-phase ferritic-martensitic structure which seems to be, as pointed out by DAS and CHATTOPADHYAY [18] and SHIN et al. [22], the governing factor in this transformation in conjunction with cooling rate. The effect of these variables can be summarized as:

- Intercritical annealing temperature is a determining factor of the martensite volume fraction (MVF) [17,23,24] that will be obtained after cooling. Also, the carbon partitioning between ferrite and austenite during the intercritical annealing is crucial to the Ms temperature and hence, for martensite carbon content and morphology (plate or laths) [17]. Lath morphology is more common for lower temperatures [17].
- Annealing time influences the fraction of austenite that will be available for the transformation (this effect is naturally limited by the fraction obtained in the lever rule, according to the phase diagram), carbon diffusion, and grain growth as well.
- Heating rate has influence in grain growth in ultra-fine-grained dual-phase steels. Higher heating rates imply in smaller critical nucleation radius which will result in finer structures after cooling provided that the intercritical annealing time is insufficient for significant grain growth [25].
- The effect of the initial microstructure in the intercritical annealing can be mainly attributed to the nucleation sites, as previously discussed.
- Chemical composition determines the stability fields of the phases, hence, the range of transformation temperature (Ac_1, Ac_3, Ms, and Mf), and the shape of the start and finish transformation curves in the continuous cooling transformation diagram (CCT).
- Finally, cooling rate influences transformation temperatures (Ar_1, Ar_3, and Ms). An increased cooling rate will lower these transformation temperatures [26]. Also, cooling rate, initial microstructure, and chemical composition will determine the final products of transformation.

3.2.2- MECHANICAL BEHAVIOR

3.2.2.1- INFLUENCE OF MICROSTRUCTURAL CHARACTERISTICS

The mechanical behavior of dual-phase steels is basically characterized by a continuous stress-strain curve (without yield point elongation), high UTS/YS ratio, and high strain hardening coefficient [1]. Several researchers have studied over the last 50 years the effect of many variables, such as martensite volume fraction (MVF) [17,19,23,24,27–33], ferrite grain size (d_f) [24,29,30], martensite island size (d_m) [30], and morphology [16,18,19,34] on the mechanical behavior of the dual-phase steels. In this section, the effect of MVF, d_f, d_m, and morphology will be discussed based on published data summarized in Table 1 [18,19,23,28–38]. At first, a more simplistic approach will be adopted to assess the data.

In the following sections, when other techniques and approaches are being discussed, further insights will be presented.

Table 1 – Chemical composition, martensite volume fraction, ferrite grain size, martensite grain size, yield strength, ultimate tensile strength and uniform elongation from multiple reference works [18,19,23,28–38].

Material (%wt.)	MVF (%)	df (μm)	dm (μm)	YS (MPa)	UTS (MPa)	UE (%)	Reference
0.052C; 0.9Mn; <0.01Si	6	-	-	216	481	-	RAMOS et al. (1979)
	10	-	-	227	527	-	
	15	-	-	216	549	-	
0.11C; 0.78Mn; 0.28Si	15	-	-	259	614	-	RAMOS et al. (1979)
	25	-	-	276	778	-	
	35	-	-	284	732	-	
0.1C; 2Si	14	-	-	427	745	16.7	KIM; THOMAS (1981)
	22	-	-	407	765	14.9	
	22	-	-	524	931	5.4	
	50	-	-	510	958	11.5	
	40	-	-	441	862	10.3	
	40	-	-	386	993	5.1	
	64	-	-	538	1027	9.4	
	60	-	-	503	986	6.9	
	60	-	-	634	1055	4.4	
0.11C; 1.45Mn; 0.45Si; 0.16Mo; 0.41Al	24.5	-	-	301	683	18.5	MARDER (1982)
	64.6	-	-	576	1062	7	
0.098C; 1.45Mn; 0.58Si; 0.075V	18.3	-	-	320	661	18	MARDER (1982)
	59.8	-	-	479	958	8.5	
0.12C; 1.63Mn; 0.055Si; 0.034Al; 0.054V; 0.06Zr	16	7.3	-	324	634	19	SZEWCZYK; GURLAND (1982)
0.034C; 0.22Mn; 0.01Si; 0.048Al	3.3	91	21.8	172.4	279.2	-	CHANG; PREBAN (1985)
	3.3	59.1	16.9	187.5	294.4	-	
	3.3	35.9	24.3	235.1	325.4	-	
	2.8	28.1	13.9	275.8	337.2	-	
	3.6	20.9	13.7	271.7	328.9	-	
	2.6	15.3	5	277.9	329.6	-	
	3.6	15.5	11.3	285.4	327.5	-	
	2.6	17.2	5.2	286.8	327.5	-	
0.07C; 0.32Mn; 0.01Si; 0.035Al	11.8	8.2	3.1	416.4	490.2	-	CHANG; PREBAN (1985)
	12	11.8	5.3	352.3	486.1	-	
	12.7	12.9	5.7	320.6	450.2	-	
	10.2	68.1	23.2	197.9	358.5	-	
	14.2	13.2	6.4	333.7	489.5	-	
	16.2	19.4	12.6	276.5	425.4	-	
	16.9	60.8	38	211.7	393.7	-	
0.17C; 0.36Mn; 0.02Si; 0.06Al	23	6.2	2.9	599.8	758.4	-	CHANG; PREBAN (1985)
	34.9	8.5	6.1	515.7	769.5	-	
	31.8	9.7	6.1	459.2	698.2	-	

Material (%wt.)	MVF (%)	df (µm)	dm (µm)	YS (MPa)	UTS (MPa)	UE (%)	Reference
0.17C; 0.36Mn; 0.02Si; 0.06Al	34.4	8.2	5.5	491.6	762.6	-	CHANG; PREBAN (1985)
	30.6	15.6	21.6	388.2	667.4	-	
	28.6	59.5	32	238.6	575.7	-	
	24.4	58.6	15.6	231.7	477.1	-	
0.23C; 0.35Mn; 0.01Si; 0.049Al	42.8	6.5	5.9	755.7	988	-	CHANG; PREBAN (1985)
	51.3	6.8	8.8	685.3	1055.6	-	
	47.6	7.4	7.7	624.7	949.4	-	
	38.8	51	64.7	320.6	612.3	-	
	40.5	55.1	62.3	369.6	637.8	-	
	51.6	8.8	9.9	655.7	983.9	-	
	49.8	12.9	24.2	519.2	899.1	-	
	40.7	67.4	64.6	262	635	-	
	44.3	55.8	70.2	311	626	-	
0.12C; 0.87Mn; 0.25Si; 0.08V; 0.02Al	26.4	36.3	18.3	341.1	758.1	10.6	JIANG et al. (1995)
	24.5	21.9	11	340.4	785.6	10.5	
	25	18	9.9	355.1	812.5	11	
	24.6	12.3	9.4	355.9	839.5	11.8	
	25.8	8.4	6.7	368.8	884.1	11.9	
	25.1	5.6	5	394.7	951.5	12.5	
	34	34.7	20.9	369.4	818	9.4	
	35.6	20.1	14.4	388.9	884.5	9.8	
	34	17.2	13.1	385.9	886.7	9.3	
	35.5	13	10.2	398.1	930.2	10.3	
	35.8	9.8	8.4	412.7	973.4	10	
	36.3	7.7	7.1	421.3	1012.3	10.9	
	43.6	33	21	407.6	888.1	8.5	
	43.1	21.6	15.5	424.8	929.2	8.2	
	45.9	17.4	12.3	431.1	960.5	9	
	44	12.9	11.2	444.9	996.6	9.2	
	45.5	10.6	9.3	459.8	1064.3	9	
	46	8.6	8.4	469.8	1089.7	9.4	
0.166C; 1.03Mn; 0.14Cr; 0.24Si; 0.04Mo	55	-	-	645	1012.33	6.39	SARWAR; PRIESTNER (1996)
	55	-	-	570	924.09	6.39	
	55	-	-	600	1014.76	6.39	
	48.9	-	-	670	1068.63	5.87	
	27	-	-	360	703.78	5.87	
	27	-	-	357	645.57	5.75	
	27	-	-	365	694.16	5.75	
	32	-	-	305	690.85	8.09	
	32	-	-	270	667.34	8.09	

Material (%wt.)	MVF (%)	df (µm)	dm (µm)	YS (MPa)	UTS (MPa)	UE (%)	Reference
0.166C; 1.03Mn; 0.14Cr; 0.24Si; 0.04Mo	30.7	-	-	450	834.65	5.94	SARWAR; PRIESTNER (1996)
	30.7	-	-	495	838	5.94	
	29.4	-	-	525	892.16	5.34	
	29.4	-	-	516	871.28	5.34	
0.165C; 1.32Mn; 0.44Si; 0.56V	32.9	2.14	1.05	574.6	838.1	11.03	BAG et al. (1999)
	37.5	1.8	1.07	649.2	919.1	13.97	
	45	1.51	1.2	671.4	947.6	15.07	
	51.7	1.33	1.44	685.7	930.2	16.03	
	55.9	1.3	1.64	971.4	907.9	14.04	
	59.3	1.3	1.85	624.4	847.6	14.04	
	61.9	1.2	2.7	684.5	823.8	11.03	
	77.6	1.1	3.9	838.1	971.4	7.53	
	45.2	-	-	677.8	942.9	9.04	
	53.8	-	-	693.7	944.4	9.04	
	58.5	-	-	711.11	947.6	8.08	
	66.8	-	-	779.4	942.9	6.99	
0.32C; 0.88Mn; 0.99Si; 0.9Ni; 0.9Cr	30.5	-	-	337	695	-	AHMAD et al. (2000)
	59	-	-	622	1050	-	
	78.8	-	-	506	1239	-	
	91.4	-	-	497	1247	-	
	97	-	-	540	1685	-	
0.12C; 1.59Mn; 0.58Si; 0.13Al; 0.60Cr; 0.11V	32	-	-	541	892	9.5	DAS; CHATTOPADHYAY (2009)
	32	-	-	533	843	8.2	
	32	-	-	635	931	7.2	
0.11C; 0.53Mn; 0.07Si; 0.03Ni; 0.03Cr	21.3	-	-	481.8	920.1	7.5	MOVAHED et al. (2009)
	23.5	-	-	485.1	952.8	4.6	
	29.6	-	-	488.3	988.8	9	
	46.7	-	-	511.2	1067.3	9.7	
	70.9	-	-	547.2	1054.2	5.6	
0.08C; 0.65Mn; 0.3Si	13	10.8	-	352	550	15	BERGTRÖM et al. (2010)
	13	10.8	-	366	548	15	
0.11C; 0.90Mn; 0.4Si	18	8.4	-	404	643	13	BERGTRÖM et al. (2010)
	18	8.4	-	404	635	12	
0.13C; 1.50Mn; 0.2Si; 0.015Nb	25	5.7	-	540	822	10	BERGTRÖM et al. (2010)
	25	5.7	-	534	804	10	
0.15C; 1.50Mn; 0.50Si; 0.016Nb	48	3.8	-	733	1117	8	BERGTRÖM et al. (2010)
	48	3.8	-	920	1013	8	
0.062C; 1.15Mn; 0.020Si; 0.55Cr; 0.028Al	18	6.8	-	359.1	613.1	-	ROSENBERG et al. (2013)
	22.2	7.2	-	416.1	626.3	-	
	25	6.5	-	424.8	678.8	-	
	35.2	5.7	-	477.4	775.2	-	

Material (%wt.)	MVF (%)	df (µm)	dm (µm)	YS (MPa)	UTS (MPa)	UE (%)	Reference
0.090C; 1.32Mn; 0.014Si; 0.020Cr; 0.044Al; 0.055Nb; 0.042V; 0.014Ti	25.7	4.1	-	420.4	744.5	-	ROSENBERG et al. (2013)
	31.7	3.4	-	424.8	744.5	-	
	39.1	2.9	-	442.4	775.2	-	
0.181C; 1.24Mn; 0.013Si; 0.014Cr; 0.042Al	43	7.2	-	486.1	937.2	-	ROSENBERG et al. (2013)
	59.2	5.9	-	595.6	1033.6	-	
	78.2	4.6	-	919.7	1243.8	-	
0.05C; 5Mn; 3Al	60.6	-	-	517	805	8.5	ZHANG et al. (2014)
0.10C; 5Mn; 3Al	76.1	-	-	644	984	7	
0.15C; 5Mn; 3Al	89.3	-	-	785	1199	6	
0.08C; 1.83Mn; 0.42Si; 0.18Cr	39.79	-	-	471	675	11.68	ZHANG et al. (2015)
	44.21	-	-	445	753	10.9	
	58.21	-	-	456	795	10.69	
	66.31	-	-	509	830	9.45	
	81	-	-	554	880	5.93	
	17.36	-	-	240	538	22.82	
	22.94	-	-	294	616	19.95	
	53.49	-	-	370	747	17.15	
	71.09	-	-	487	863	11.06	
	81.38	-	-	527	882	8.15	
0.18C; 1.25Mn; 0.2Si	28.1	5	3.6	441	736	20.58	ASHRAFI et al. (2016)
	34.1	4.6	3.7	511	800	18.3	
	39	4.1	3.8	520	828	17.9	
	48.9	3.7	4.6	528	826	14.87	
0.094C; 3.4Mn; 0.003Si	15	5.67	1.18	260	693	16.3	LAI et al. (2016)
	17	-	-	260	737	16	
	19	5.27	1.65	282	767	14.3	
	28	4.72	2.07	379	930	12.3	
	37	3.84	2.61	474	1058	10.8	
	11	-	-	265	644	17.8	
	16	5.16	1.04	287	719	15.2	
	21	5.63	1.54	304	777	13.7	
	33	4.43	2.59	376	767	10.5	
	35	4.31	2.78	432	949	8.4	

- Martensite volume fraction

The effect of MVF, which is the most basic feature of a dual-phase microstructure, has been widely studied. Figures 3a, 3b, and 4 relate MVF to UTS, YS, and UE, respectively. Initially, it was believed that there was a linear relationship between MVF and UTS [24]. However, it was soon realized that this was only true in some cases up to a certain fraction of martensite [23,28] and the slope of the initial curve was also variant according to the alloy system [16]. These observations are consistent with the datum points displayed in Figure 3a. Despite the high dispersion, there is a clear tendency of increasing UTS with increasing MVF. This is a natural consequence of the increase of the harder phase content. The notably high dispersion can be attributed to the wide variety of alloy systems, grain size, and morphology of microstructure in these studies.

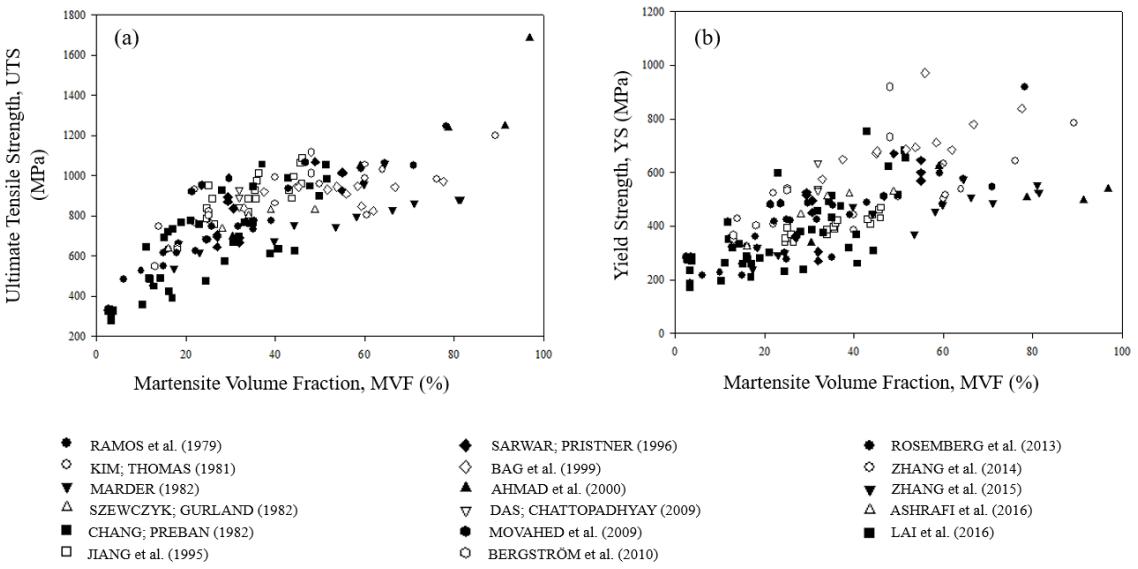

Figure 3 - a) MVF x UTS; b) MVF x YS [16–19,23,27–38].

A similar behavior is observed in Figure 3b. The yield strength is directly proportional to the MVF. In the following sections it will be shown that the yielding in dual-phase steels is mainly determined by ferrite. A higher MVF implies a higher density of geometrically necessary dislocations in ferrite which are created because of the volume expansion involved in martensitic transformation. Furthermore, a higher MVF means there will be a higher density of phase boundaries, which provide more resistance to dislocation glide than grain boundaries [39,40].

Figure 4 shows UE as a function of MVF. The distribution of data resembles the UTS x UE curve, which is natural since UTS tends to increase with increasing MVF. The clear

tendency here is that a higher uniform elongation tends to occur for lower MVF. However, it is also clear that there are possibilities of achieving reasonably high UE with relatively high MVF if compared, for instance, with conventional high strength steels. This is noteworthy considering that higher martensite volume fractions generally result in higher UTS. As previously mentioned, this is precisely one of the main advantages of the dual-phase steels: the combination of high UTS with relatively high UE.

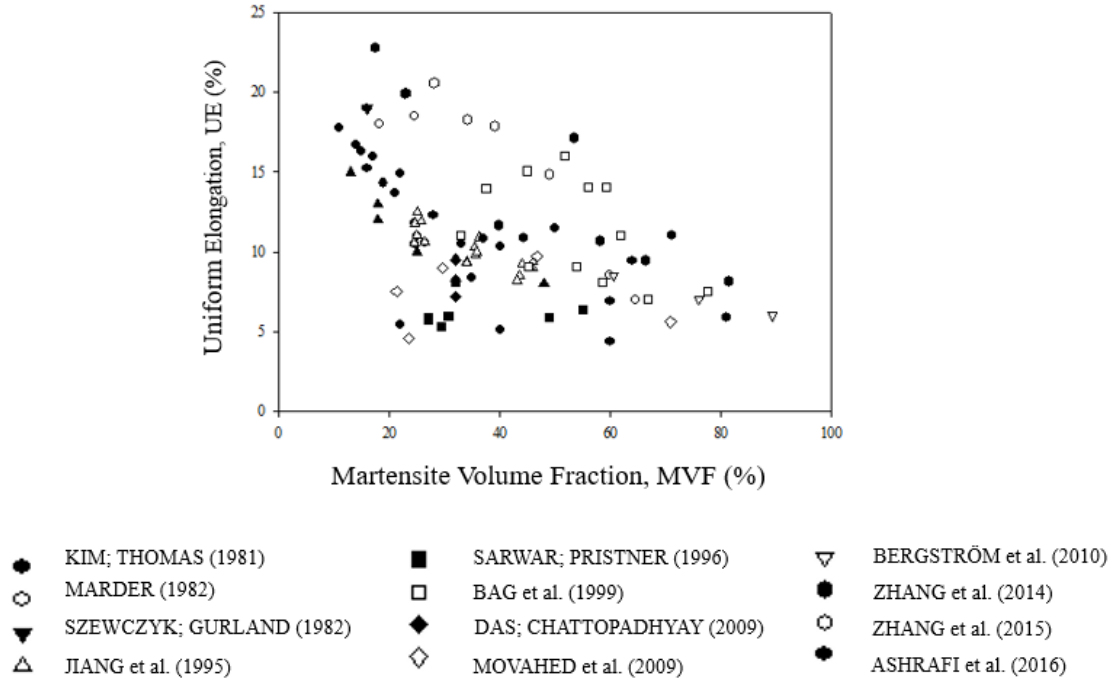

Figure 4 - MVF x UE [16–19,23,27,28,30,32,34,36,38]

- Grain Size

Several studies which regard the effect of grain size on dual-phase steels have been published. They can be divided into three groups: the ones that study regular grain size structures [29,30,36] (or non-submicrometric grain structures), the ones that study ultra-fine-grained (UFG) structures [22,25,41–43] – or submicrometric grain structures - and the ones with bimodal structures [44,45], which are basically a mixture of coarse and ultra-fine grains. The discussion here regards the first two groups, and they are considered without distinction. Figure 5a shows the influence of ferrite grain size (d_f) on YS and Figure 5b shows the relation between d_f and UTS.

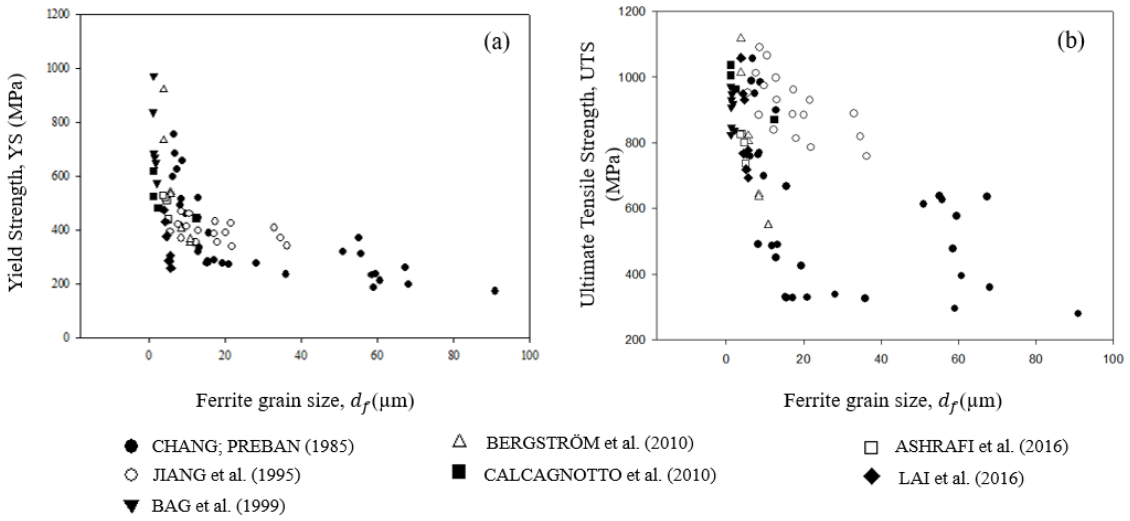

Figure 5 – (a) df x YS; (b)df x UTS [17,27,29,30,33,36]

CHANG and PREBAN [29] assessed the influence of ferrite grain size (d_f, measured as mean free path in ferrite) on YS and UTS and verified the validity of a Hall-Petch relationship [46,47] – Equation 3:

$$\sigma = \sigma_0 + k d_f^{-1/2} \tag{3}$$

The authors documented that the slope k varies with MVF for both YS and UTS and the intercept σ_0 is independent of MVF for YS, but dependent on MVF for UTS.

JIANG et al. [30] also verified the validity of a Hall-Petch equation between ferrite grain size and flow stress. However, the intercept σ_0 and the slope k were found to depend on deformation and martensite particle size besides MVF. The authors reported greater influence of MVF on the slope than on the intercept. According to their analysis, the intercept corresponds to the average flow stress of the ferrite matrix, and the slope is related to the back stress. Figures 6a and 6b show a plot of $d_f^{-1/2}$ versus UTS and YS, respectively, reported by JIANG et al. [30]. The linear relationship is clear, and the fitting is excellent. Each group of datum points corresponds to the same alloy subjected to a certain intercritical annealing temperature with the aim to obtain varying MVFs. The bottom line corresponds to a set of samples of about 25% MVF, whereas the middle and the upper ones correspond to sets of 35% and 45% martensite volume fraction, respectively. Hence, the slope increases with increasing MVF. BERGSTRÖM et al. [36] emphasize the importance of grain size in dual-phase steels stating that the flow stress is about seven times more sensitive to ferrite grain size than that for single phase ferrite.

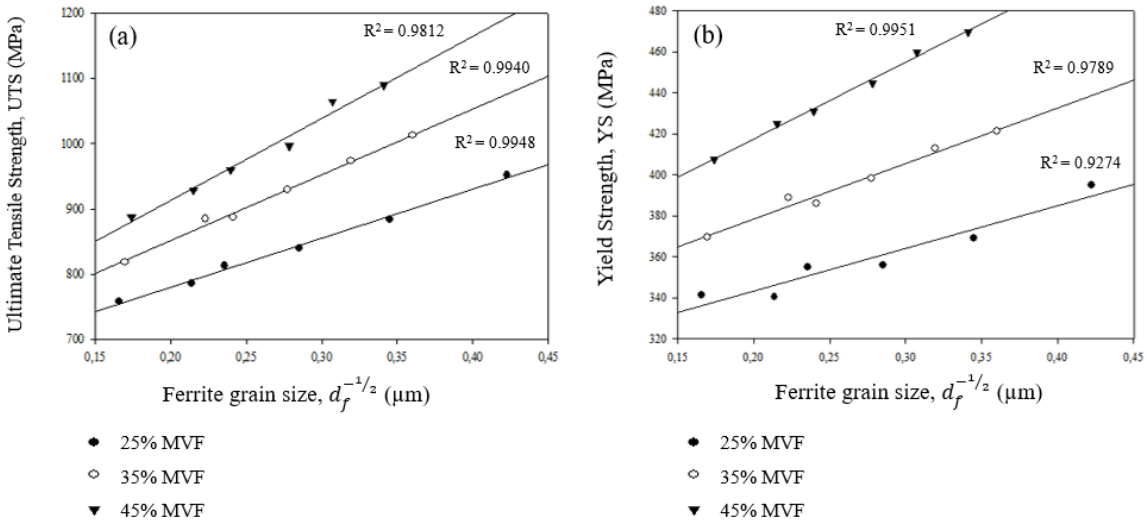

Figure 6 – Hall-Petch relationship in dual-phase steels for sets of different martensite volume fractions (adapted from [30]).

Figure 7 relates d_f and UE. The observation of all datum points seems to indicate that smaller ferrite grain size results in lower uniform elongation. However, it is worth mentioning that in the experiments carried out by BERGSTRÖM et al. [36], ASHRAFI et al. [27], and LAI et al. [33], the samples with higher MVF also had the smallest ferrite grain sizes. The samples of CALCAGNOTTO et al. [48] had roughly the same martensite content. So, what we are looking at here may be the result of two interlinked variables and an isolated observation of these datum points may be insufficient to draw relevant conclusions.

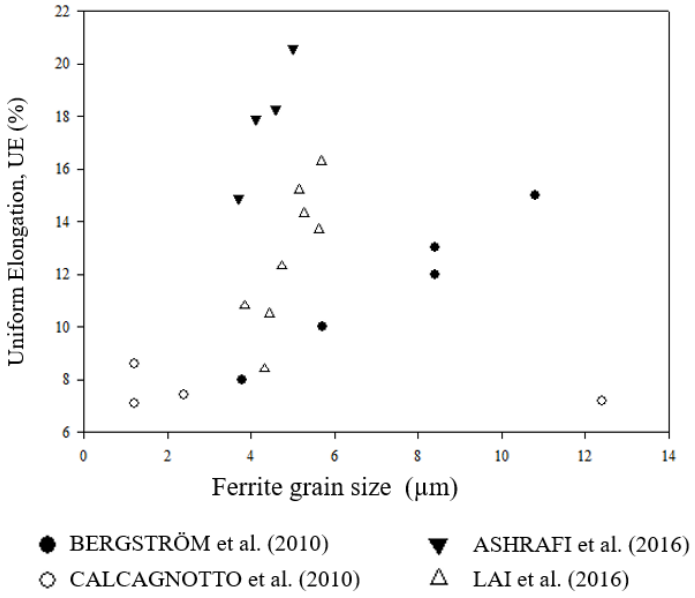

Figure 7 – UE x d_f [27,33,36,48].

Regarding martensite island size, Figures 8a and 8b relate this variable to YS and UTS, respectively. There seems to be a similar trend to the one observed in respect to the influence of ferrite grain size on UTS and YS. JIANG et al. [30], however, account its influence in the intercept and slope of the Hall-Petch equation obtained using ferrite grain size. CHANG and PREBAN [29] account for martensite colony size in a Hall-Petch type yield strength dependence to martensite volume fraction. In this case, d_m is considered in the Hall-Petch slope and coefficient. The problem presented by the authors is the difficulty in obtaining the average distance from the head of a dislocation pile-up to the closest dislocation source in an adjacent grain. Also, the model assumes that martensite deformation is negligible, which is not reasonable.

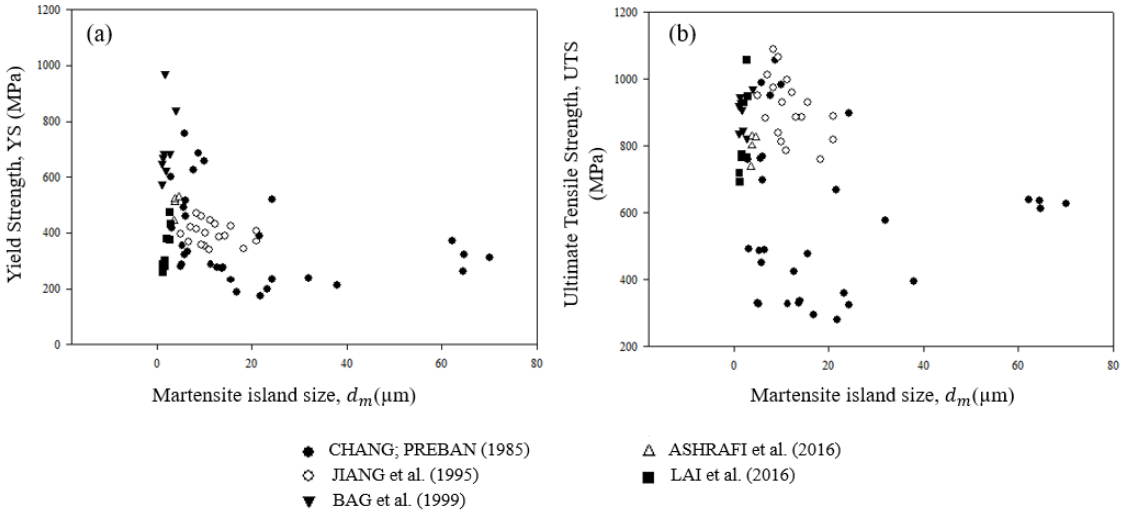

Figure 8 – (a) d_m x YS; (b) d_m x UTS [17,27,29,30,33].

Figure 9 relates martensite island size and uniform elongation. Few of the reviewed articles present measurements of both these parameters. However, it is possible to see that decreasing d_m leads to higher uniform elongation. The two groups of data presented in Figure 9 form two clusters which differ fundamentally in chemical composition (in white: 0.094%C; 3.4%Mn; 0.003%Si. In black: 0.18%C; 1.25%Mn; 0.2%Si) and initial microstructure (microstructure before intercritical annealing that produces the dual-phase structure; in white: spherodized microstructure; in black: cold-rolled ferrite-pearlite). Since ferrite accommodates most strain as martensite accommodates most stress, smaller and more homogeneously distributed martensite islands favor, at least to some degree, a better distribution of strain thus leading to higher uniform elongation.

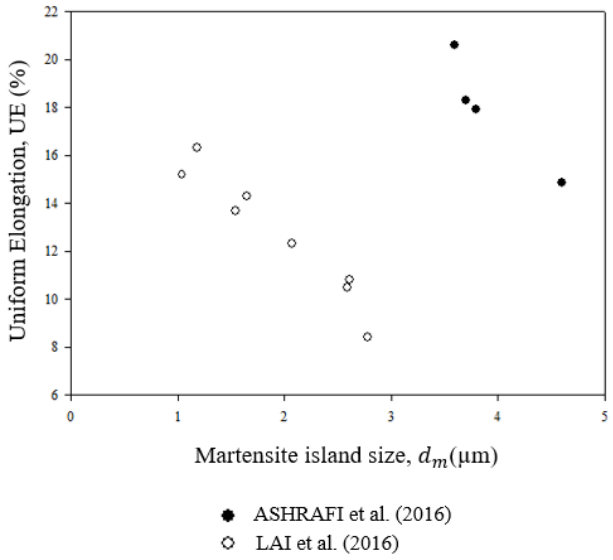

Figure 9 – dm x UE [27,33].

- Morphology

In a previous section, it was argued that the initial microstructure (prior to the intercritical annealing) determines the final microstructure (after intercritical annealing and partial martensitic transformation) primarily due to the influence on how nucleation proceeds. Here, the initial microstructure (IM) will be used to refer to the microstructure prior to the intercritical annealing which is the main factor that determines the morphology of the final dual-phase structure instead of the final morphology *per se.* The main differences in morphology are summarized as follows:

- An initially martensitic structure provides a high density of nucleation sites [18] along lath boundaries and results in fine and fibrous martensite in the ferrite matrix [16].
- In an initially ferritic-pearlitic structure, austenite nucleates along carbide/ferrite interfaces and grows. Quenching leads to a globular microstructure [16].
- When the initial structure is austenitic, intercritical annealing leads to the nucleation of ferrite in austenitic grain boundaries [16] as well as in regions of lower manganese concentration due to segregation. Consequently, the microstructure is dependent on austenitic grain size and tends to be coarser than the ones obtained from martensitic or ferritic-pearlitic structures [16].
- If the sample is deformed, more defects are introduced which implies in a higher density of nucleation sites. Hence, in general, deformation will lead to a more

refined microstructure. Also, if austenite is strained by rolling, for instance, grains will be flattened and elongated which will favor a fibrous microstructure [34].

Figures 10a, 10b, and 11 relate IM and UTS, YS and UE, respectively. The numbers in the *x* axis correspond to the initial microstructures listed below the figures, namely: ferrite-pearlite (1), martensite (2), austenite (3), deformed austenite (4), cold-rolled ferrite-martensite (5), cold-rolled ferrite-pearlite (6), and spherodized microstructure (7). The bubble plot was adopted to allow a visualization of martensite volume fraction along with morphology data. The larger the bubble, the larger the MVF. In this plot, by picking bubbles of similar sizes, hence, similar MVF, relevant differences can be found in UTS, YS and UE by varying the initial microstructure prior to intercritical annealing. Hence, it is clear that morphology does play an important role. See, for instance the red bubbles with initial microstructures "1", "2", and "3" [18]. The similar size indicates similar MVF. These structures showed distinct behaviors regarding UTS (Figure 11a), YS (Figure 11b) and UE (Figure 12).

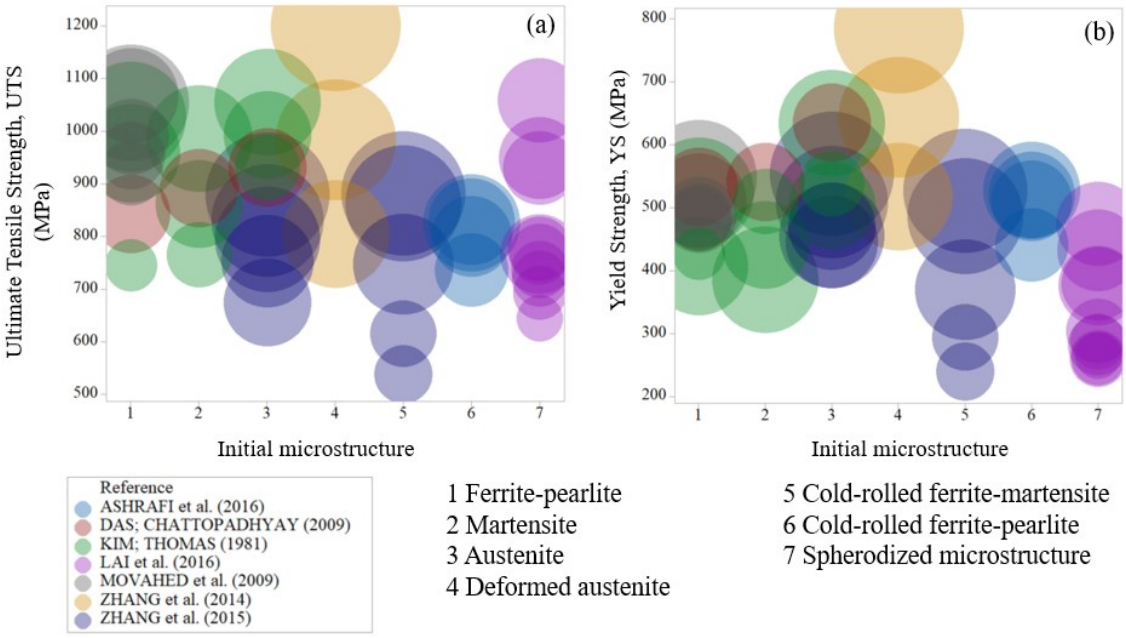

Figure 10 – Bubble plot: (a) Initial microstructure x UTS; (b) Initial microstructure x YS. Bubble size regards martensite volume fraction (MVF). The larger the bubble, the larger the MVF [16,18,19,23,27,30,32,33].

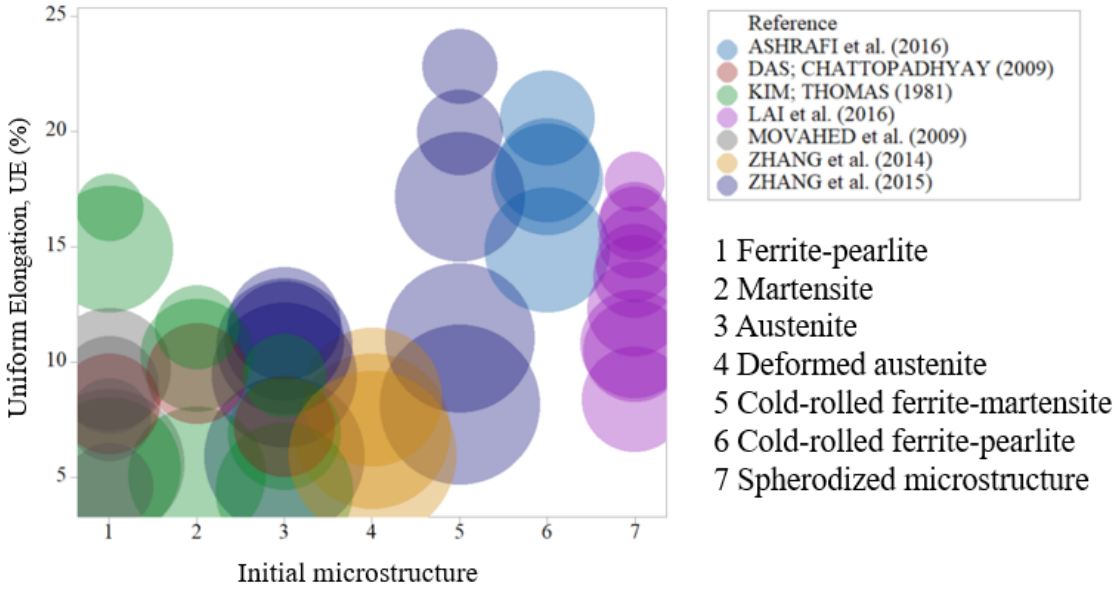

Figure 11 – Bubble plot: Initial microstructure x UE [16,18,19,23,27,30,32,33]. Different colors highlight different literature sources. Bubble size is relative to martensite volume fraction (MVF).

Some of the observations drawn from these studies are:

- KIM and THOMAS [16] compared a coarse structure with a fine and fibrous and a globular one and verified that the coarse structure had much lower ductility but higher strength then the latter ones. The difference in ductility was attributed to a change in failure mechanisms from the fine to the coarse structure. The authors observed premature failure due to cleavage crack initiation and propagation in the ferrite matrix. The reasons for the higher strength, however, were not stated.
- SARWAR and PRIESTNER [34] studied the effect of warm rolling of the two-phase (ferrite and austenite) mixture and the presence of epitaxial ferrite ("ferrite formed by transformation of austenite by epitaxial growth on retained ferrite during cooling from intercritical annealing temperature" [49]) in the final structure. They verified that warm rolling results in a fibrous martensitic structure with increased strength along the rolling direction, but the presence of epitaxial ferrite produces a decrease in strength concomitant with an increase in ductility.
- BAG et al. [17] state that dual-phase steels containing similar amounts of finely dispersed ferrite and martensite exhibit the optimum combinations of high strength and ductility.
- DAS and CHATOPADHYAY [18] also report fine and fibrous martensite morphology having the best combination of strength and ductility.

CONCLUDING REMARKS

The effects of MVF, grain size, and morphology were assessed based on some of the data available in the literature. A somewhat similar analysis can be found in recent review articles [2,50]. A summary is presented in a dispersion matrix in Figure 12. It has been shown that there is an approximately linear relationship between MVF and UTS and MVF and YS. Ferrite grain size relates to UTS and YS following a Hall-Petch equation. Morphology also plays a role in determining the alloy's mechanical behavior. A wide comparison throughout reported data in the literature naturally finds more complexity due to the diversity of multiple variables. This results in the high dispersion noted in the plots of Figure 12.

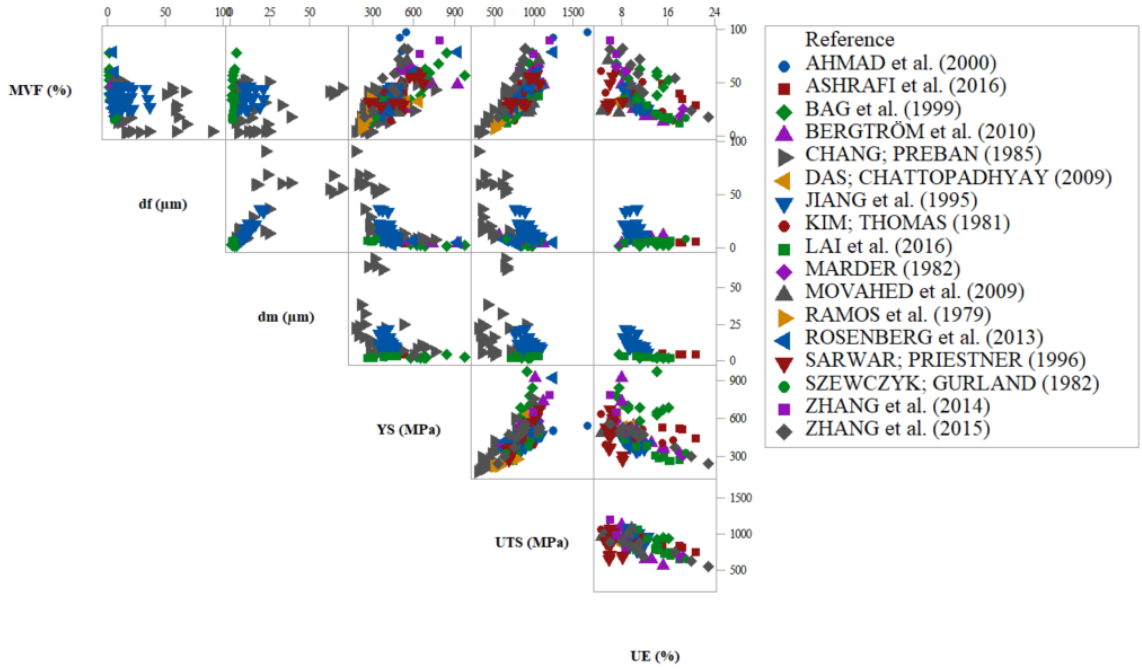

Figure 12 - Dispersion matrix: MVF, d_f, d_m, UE, YS and UTS [16–19,23,27–38].

3.2.3- DEFORMATION MODELS

In this section, some models developed as attempts to understand and predict the behavior of multiphase materials are presented. First, Ashby's theory for deformation of non-homogeneous materials [51] and the concept of geometrically necessary dislocations (GNDs) are discussed. Second, the rule of mixtures, which is used to describe the behavior of composite materials accounting for stress and/or strain partitioning, is examined in detail [52]. Finally, Tomota's theory of stages of deformation based on continuum mechanics is analyzed.

- Ashby's theory

In the 1960s, Ashby presented a micromechanistic based model in which he introduced the concept of geometrically necessary dislocations to describe the behavior of non-homogeneous materials [51]. The author defines a non-homogeneous alloy as "one in which gradients of deformation are imposed by the microstructure" [51]. The accumulation of dislocations occurs for two reasons: one is consequence of them trapping one another in a random way, the other is a consequence of the requirement for compatible deformation in the presence of the microstructurally imposed strain gradients. The first refers to the statistically stored dislocations while the second refers to the geometrically necessary ones. It should be however noted that these dislocations are not physically different.

In Ashby's work, some calculations are performed considering hypothetical structures. Furthermore, the author develops expressions for the density of geometrically necessary dislocations (ρ_G), assuming equiaxed, plate-like, and needle-like domains. For instance, for equiaxed particles, Equation 4 is obtained:

$$\rho_G = \frac{8f\gamma}{\boldsymbol{b}d} \tag{4}$$

where *f* is the volume fraction of cube shaped particles, *d* is particle size, **b** is magnitude of the burgers vector and γ is the shear strain. Equation 4 gives a crude measure of the density of GNDs in the form of loops.

Another important concept presented in Ashby's theory is the geometric slip distance (λ_G), which is characteristic of the microstructure. For plates, this distance equals the length "l" of the plate and for equiaxed particles, r/f, where r is the radius of the spherical particle and *f* the volume fraction of particles.

The general expression for the accumulation of GNDs is described by Equation 5:

$$\rho_G = \frac{1}{\lambda_G}\frac{4\gamma}{\boldsymbol{b}} \tag{5}$$

A direct application of Ashby's model in dual-phase steels is perhaps limited since it considers non-deformable particles and martensite does deform [52]. However, the

concepts presented by the author are valuable and have been extensively used by other researchers to explain the substructure of dislocations in ferrite of dual-phase steels [48,53–55].

Figure 13a shows a kernel average misorientation (KAM) map built using EBSD analysis and Figure 13b shows the corresponding calculated density of GNDs in the research of CALCAGNOTTO et al. [48]. The density varies from around 2.5 x 10^{14} m^{-2} near martensite islands to 2.5 x 10^{13} m^{-2} in the ferrite interior. In this case, the method for GND calculation uses Equation 6.

$$\rho_{GND} = \frac{2\vartheta}{ub} \tag{6}$$

where ϑ is the misorientation angle; u is the unit length and b is the module of the Burgers vector. The geometrically necessary dislocation density (ρ_{GND}) is expressed in dislocations per unit length.

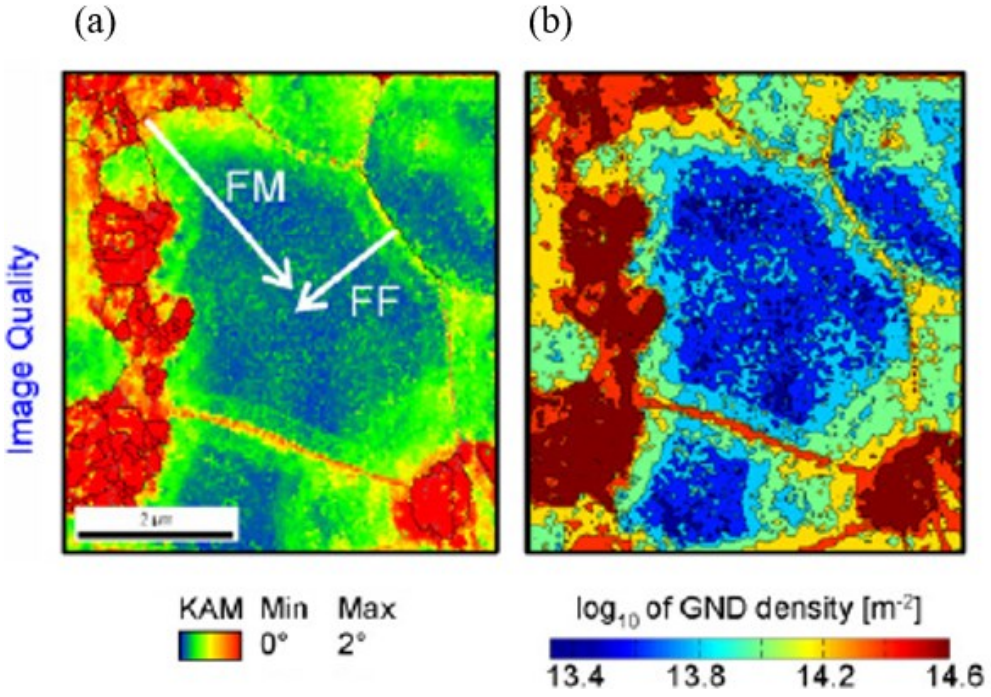

Figure 13 – (a) Kernel average misorientation (KAM) map centered in a ferrite grain; (b) Corresponding calculated density of geometrically necessary dislocations. FF: ferrite-ferrite boundary; FM: ferrite-martensite boundary [48].

- Law of mixtures

The law or rule of mixtures is reported to have been first proposed by Voight in 1889 [56]. It is an expression that relates mechanical properties of a composite material in terms of the bulk properties and the relative amounts of the constituent phases [56]. Equation 7, for instance, relates the yield strength (σ_{YS}) of the composite as a sum of the contribution of the individual constituents and their respective volume fractions (f).

$$\sigma_{YS} = \sum_{i=1}^{n} (f_i \sigma_{YS,i}) \tag{7}$$

There are different variations of the rule of mixtures according to the basic assumptions, such as equal stress or equal strain among the phases and the intermediate law of mixtures. The first two are extreme conditions while the third, as the name suggests, is an intermediary condition.

A relevant model based on the law of mixtures is proposed by MILEIKO [57] to describe the behavior of a composite material constituted by a ductile matrix and a more resistant fiber. The basic assumption of the model is homogeneous deformation, hence, equal strain between the phases (Figure 14).

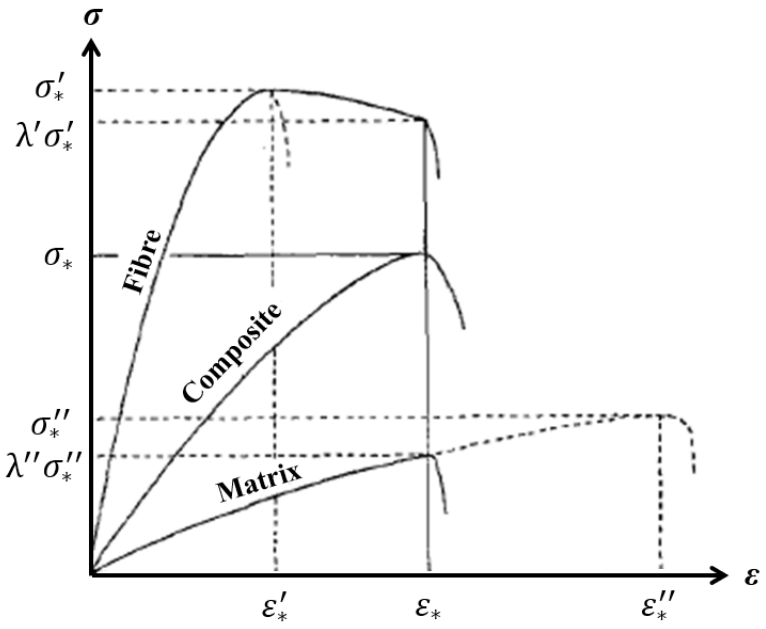

Figure 14 – Schematic representation of the flow curves of the matrix, fibre, and resulting composite by the equal-strain rule of mixtures [57].

Mileiko's theory was used by DAVIES [24] to assess the influence of martensite volume fraction on the strain hardening coefficient in dual-phase steels and found good agreement with the experimental results, despite the necessary assumption of equal strain in the model. BHADESHIA and EDMONDS [58] compared Mileiko's theory with Tomota's model, which will be presented in the following section. Both were in good agreement with the presented data, but Tomota's model seems to show a better fitting (Figure 15).

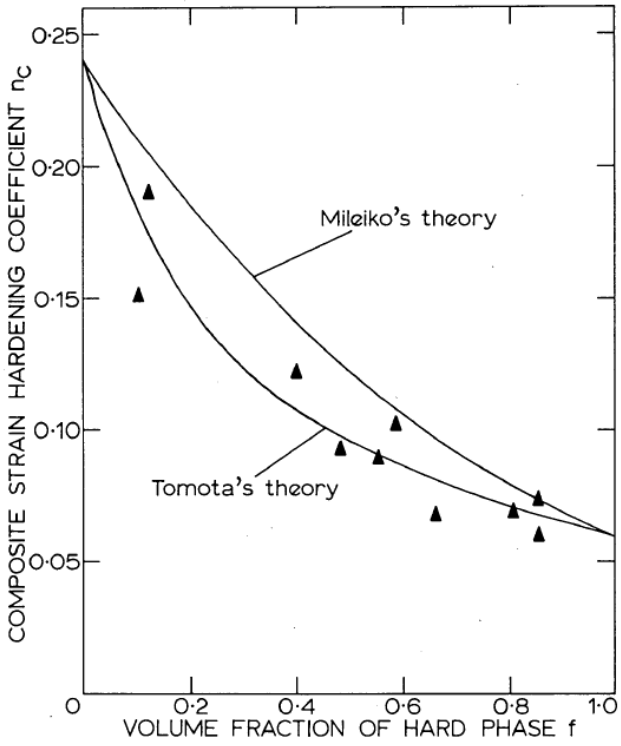

Figure 15 – Comparison between the curves of composite strain hardening coefficient as a function hard phase volume fraction made between Tomota's theory and Mileiko's theory [58].

The intermediate law of mixtures is well explained by GOEL et al. [59], but was first proposed, according to the authors, by TAMURA et al. (1973). Both stress and strain of the individual components and the alloy can be written in the form of Equations 8 and 9:

$$\sigma_C = V_{fm}\sigma_m + V_{ff}\sigma_f \quad (8)$$

$$\varepsilon_C = V_{fm}\varepsilon_m + V_{ff}\varepsilon_f \quad (9)$$

where σ is the stress, *Vf* is volume fraction and ε is deformation. The indexes *c*, *m,* and *f*, correspond to the composite structure, martensite, and ferrite, respectively.

The stress and strain partitioning depends also on a slope 'q', defined as the ratio of stress to strain transfer according to Equation 10, without which Equations 8 and 9 are meaningless:

$$q = \frac{\sigma_m - \sigma_f}{\varepsilon_m - \varepsilon_f} \tag{10}$$

This term basically defines the strain partitioning. Figure 16 shows schematically how the composite curve is obtained from Equations 7, 8, and 9.

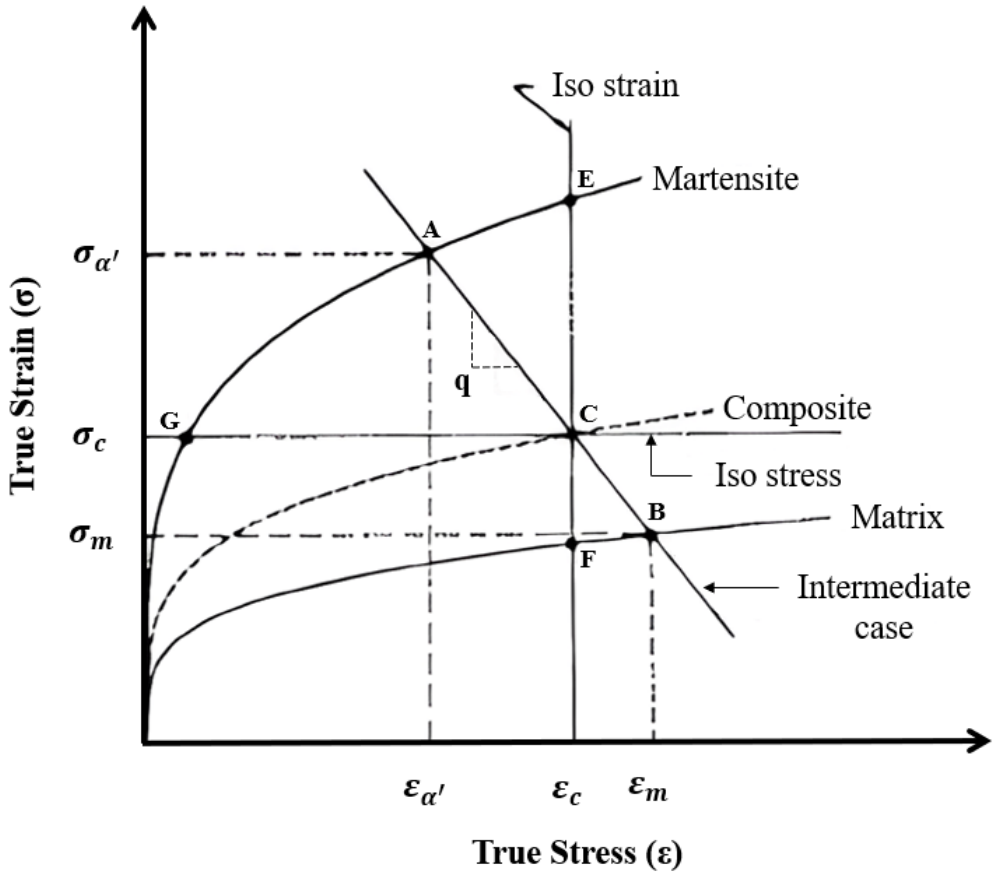

Figure 16 – Schematic representation of the intermediary law of mixtures illustrating the matrix, martensite and resulting composite flow curves. The slope "q" is the ratio of stress to strain transfer [59].

It is important to highlight that the stress to strain transfer ratio "q" varies as the composite structure is deformed [60].

- Tomota's theory

Tomota's theory [61] was proposed based on a ferrite-austenite steel in tensile deformation. Its fundamental aspect is the separation of deformation in three stages with two transition points. In the first stage, the two phases deform elastically. After the yield point of the softer phase, plastic deformation begins in one, but elastic deformation continues in the harder phase. In the third stage, marked by the yielding of the harder phase, both phases deform plastically. This approach is concerned with the distribution of stress in an averaged manner [61]. Figure 17 presents a result of this model comparative

to the law of mixtures with equal stress and equal strain assumptions. One may observe that it is quite like the equal strain condition, except for the second stage of deformation.

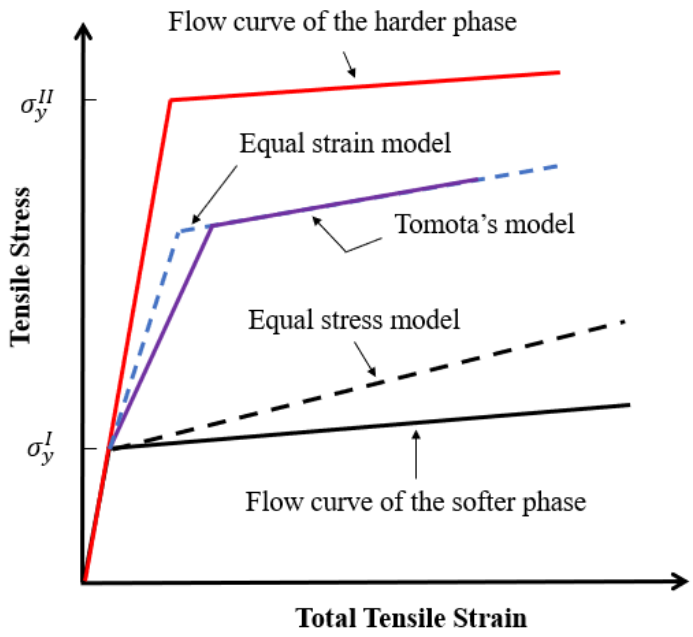

Figure 17 - Schematic flow curves of the softer phase, the harder phase, the composite using the equal stress mode, equal strain model and Tomota's model. Adapted from [61].

Besides the aforementioned models, several others have been proposed over the years such as the semi-mechanistic model by GOEL et al. [59] and a dislocation-based model by BERGSTRÖM et al. [36]. Goel's model was developed for dual-phase steels with retained austenite but can be applied to other materials, such as austenitic and ferritic-austenitic stainless steels. The authors derived expressions for the composite flow curves considering the work hardening of ferrite, martensite, and retained austenite and load transfer between the phases using an intermediate law of mixtures. The work hardening of ferrite includes the normal behavior plus the extra work hardening due to the accommodation of the strain generated in the quenching process and the strain-induced martensite.

Bergström's model [36] is based on a derived relationship for the density of dislocations as a function of strain and a non-homogeneity parameter which specifies the fraction of ferrite taking active part in the plastic deformation process. The authors assessed the model with experimental results for dual-phase steels with 13, 18, 25, and 48% of martensite volume fraction and verified that the larger the MVF, the smaller the volume fraction of ferrite that initially takes part in the plastic deformation. This is pointed out as an explanation for the high energy absorption capacity of dual-phase steels.

3.2.4- MICROSTRUCTURAL EVOLUTION

In this section, the microstructural evolution of a dual-phase steel during deformation will be briefly discussed based on the transmission electron microscope (TEM) images of different straining stages presented by KORZEKWA et al. [53]. It should be clarified that there are mathematical models, besides the ones mentioned in the previous section, which allow the modelling of the material's flow behavior, based on the Hollomon [62], Ludwik [63], Swift [64], and Voce [65] equations – thus phenomenological models. For dual-phase steels, it has been demonstrated that the strain hardening occurs in more than one stage [53]. Therefore, more than one strain hardening exponent is needed to obtain an appropriate fitting of the curve. One of the approaches which allows a clear visualization is the Crussard-Jaoul plot [66,67], which basically consists in plotting the logarithm of the strain hardening rate as a function of the logarithm of true plastic strain (Figure 18). Each line segment shows a different slope, which determines a different deformation stage.

KORZEKWA et al. [53] present TEM images of tensile specimens of dual-phase steels deformed up to 1%, 2%, 7%, and 14% true strain, which correspond to stages two and three of strain hardening (Figure 18). A pre-strain image is also presented, revealing a higher density of dislocations in ferritic regions close to martensite islands than in the center (Figure 19). This is attributed to the volume change and martensite transformation shear involved in the martensitic transformation [53]. The presence of these unpinned dislocations is appointed as responsible for the low and continuous yield stress in dual-phase steels [15,53].

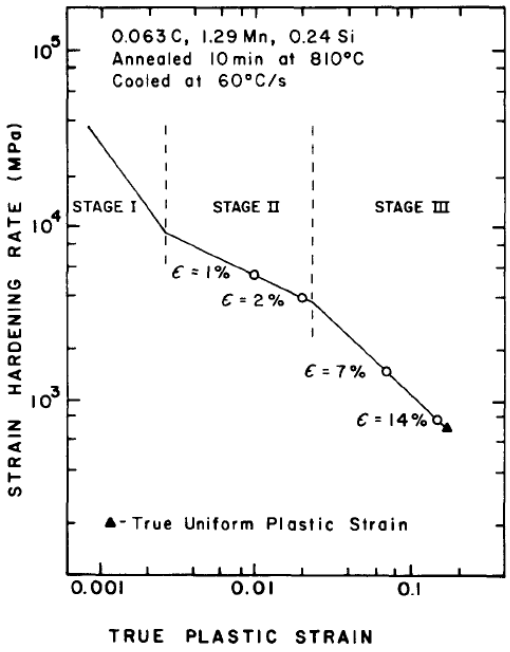

Figure 18 – Crussard-Jaoul plot: true plastic strain *versus* strain hardening rate highlighting stages of deformation I, II, and III by the different slopes [53].

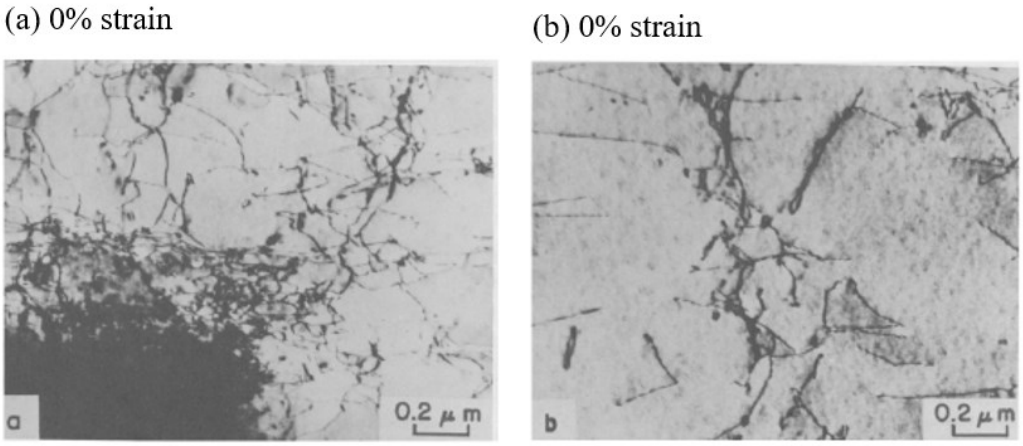

Figure 19 – TEM: single ferrite grain in dual-phase steel; (a) high dislocation density close to martensite; (b) lower dislocation density far from martensite [53].

Figures 20a–f show the dislocation structures in different levels of straining (1%, 2%, 1%, 2%, 7%, and 14%, respectively). The substructures revealed in Figures 20a, 20b, 20c, and 20d, which correspond to stage II, consist of "gradients in dislocation density and configuration across the matrix ferrite grains" [53]. In Figures 20a and 20b dislocation walls are detected. Figures 20c and 20d show dislocation tangles. The progression of deformation leads to the development of cellular substructures (Figures 20e and 20f). Initially the cells are not well defined, but they evolve in stage III to completely occupy the ferrite [53]. An interesting observation, though, is that the authors report variation of

cell size within the grain, being smaller near martensite (0.4μm) than away (0.7μm). Furthermore, no significant variation of cell size is reported to occur from ε ≈ 7% to 14%.

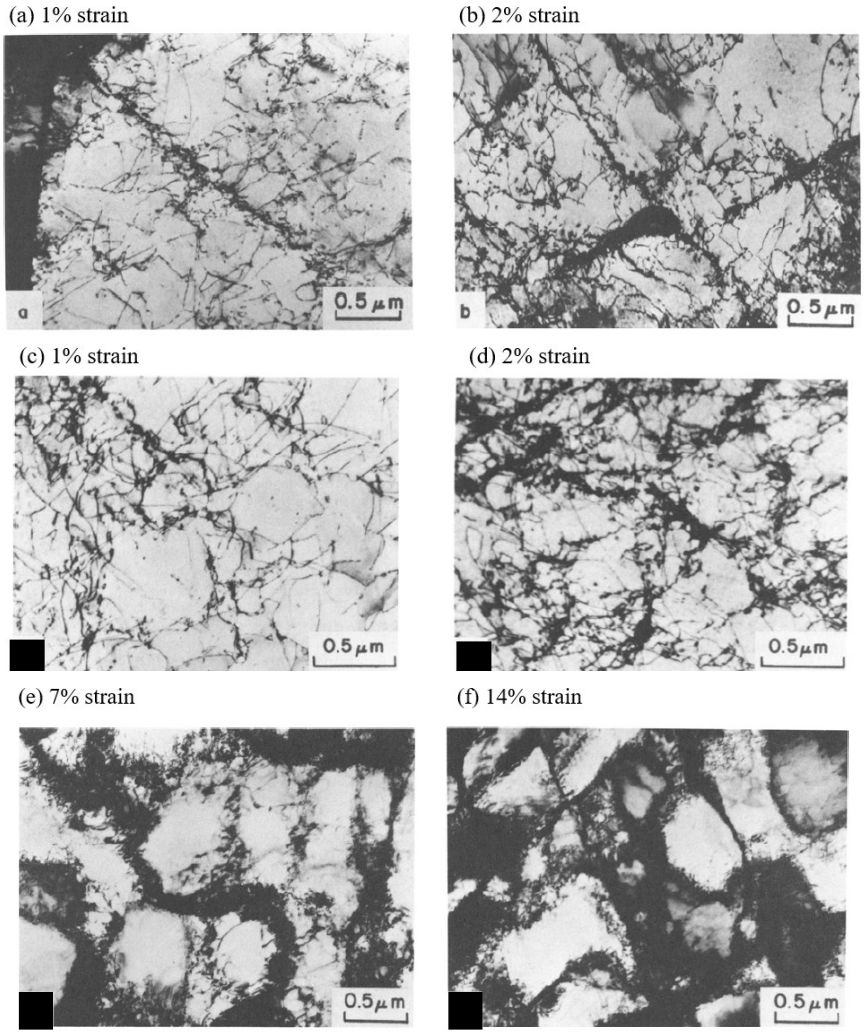

Figure 20 – TEM: (a) dislocation walls in ferritic grain during the second stage of deformation, 1% true strain; (b) dislocation walls during the second stage of deformation, 2% true strain; (c) dislocation tangles during the second stage of deformation, 1% strain; (d) dislocation tangles during the second stage of deformation, 2% strain; (e) dislocation cells during the third stage of deformation, 7% true strain; (f) dislocation cells during the third stage of deformation, 14% true strain [53].

The progression of dislocation substructure with strain can be related to the deformation stages shown in Figure 18. First, in terms of strain hardening, stage I presents a rate of decrease which diminishes in stage II and increases in stage III. KORZEKWA et al. [53] argue that the increase in dislocation density and the heterogeneous distribution raises the flow stress and results in only a moderate decrease in strain hardening with increasing strain. In stage III, the substructure is rather stable and dynamic recovery takes place. Thus, the flow stress does not increase much and the rate of strain hardening decreases with a steeper slope [53].

3.5- APPLICATIONS IN THE AUTOMOTIVE INDUSTRY

After briefly discussing fundamentals of dual-phase steels, in this section we present a basic idea regarding applications in the automotive industry. The main reference for this is the Future Steel Vehicle (FSV) report by KEELER et al. [11], World Auto Steel, which aims to assist automotive engineers by providing technical guidelines for the project of automobiles envisioning reducing fuel consumption and greenhouse gas emissions while maintaining or increasing safety requirements at reasonable cost.

The distribution of steels applied in automobile body structures according to this report is presented in Figure 21. It is revealed that dual-phase steels correspond to about 32% of all the selected steels being 10% DP1000, 10% DP800 and 12% DP500,600.

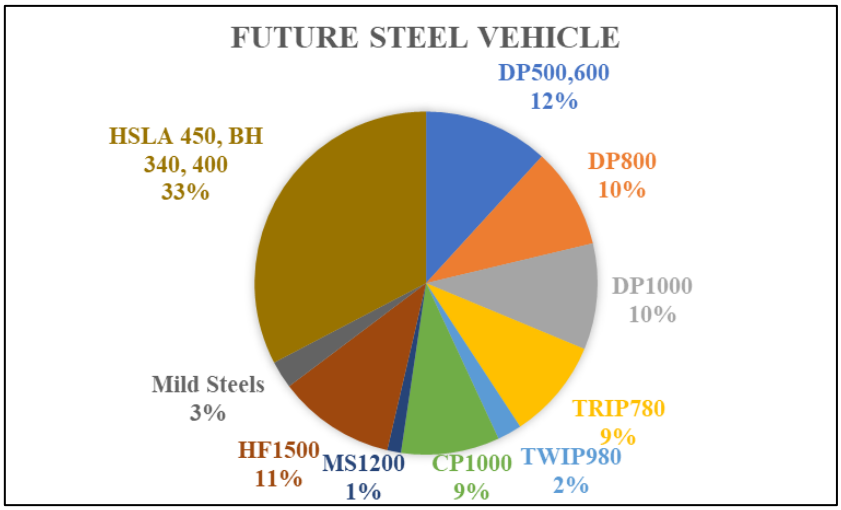

Figure 21 - Future Steel Vehicle: Body structure steels (adapted from [11]).

Some examples of application of dual-phase steels in the body structure of automobiles are the outer roof, outer door, outer body side, package tray, floor panel, inner body side, safety cage components, B-pillar, and engine cradle [11]. Figure 22 shows some components and the dual-phase steels suggested in the FSV program.

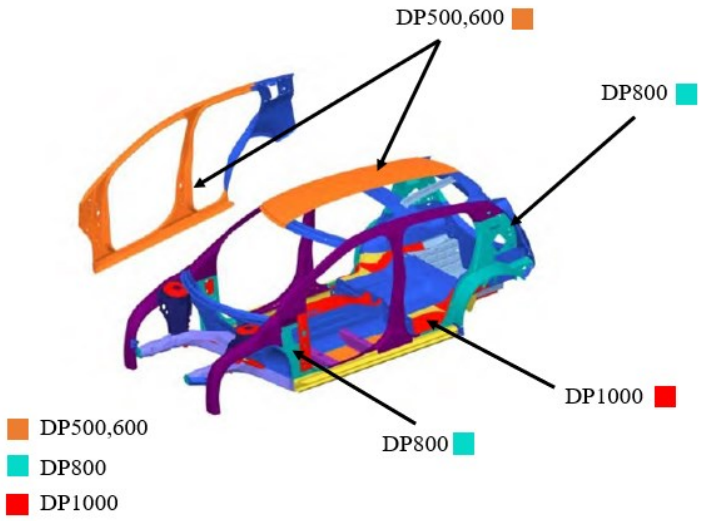

Figure 22 - Future Steel Vehicle: dual-phase steels (adapted from [11]*).*

KEELER et al. [11] also present a simple scheme (Figure 23) grossly separating material requirements in groups of structural components. It can be observed that dual-phase steels meet the requirements of excellent formability and high strength with a good balance of strength, formability, energy absorption, and durability.

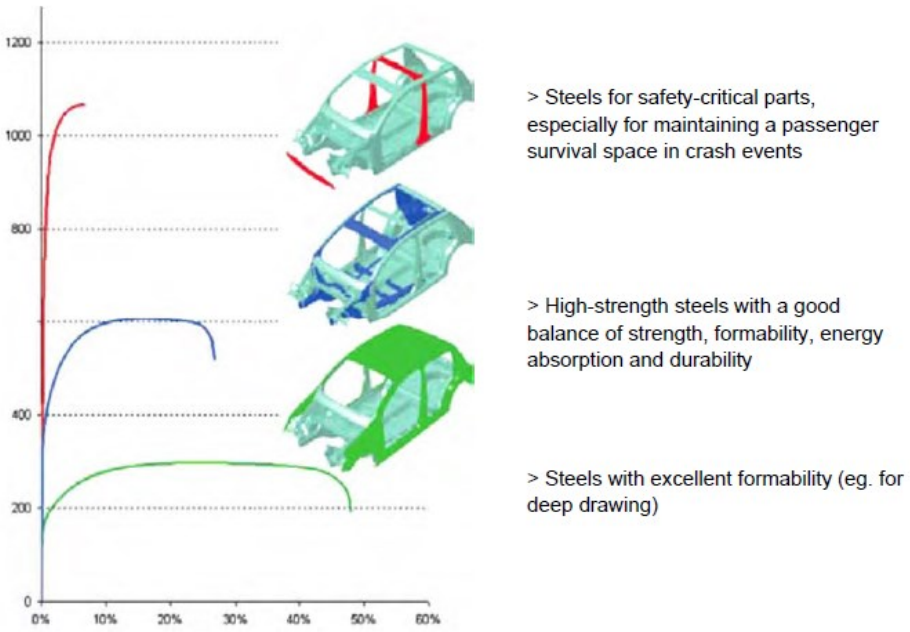

Figure 23 – Materials general requirements according to application in structural parts [11].

3.6- NANOHARDNESS BASED STUDIES

Recent developments in the indentation tests have allowed the use of increasingly smaller indenters and the exploration of the obtained results much further than a simple hardness measurement [68]. GOULDSTONE et al. [68] present a review of these developments in experimentation and modelling of indentation tests.

In this section, some studies, which were fundamentally based on nanohardness tests in dual-phase steels, are reviewed. These works can be divided in three approaches all of which are based on the assessment of the properties of the individual phases: 1) the study of the mechanical behavior *per se* – nanohardness measurements are taken in different positions and the results shed light to microstructural characteristics and to micromechanisms of deformation [39,40,69]; 2) the establishment of correlations between individual phase properties and the macroscopic behavior of the alloy [70–72]; 3) the use of the individual properties to predict macroscopic flow curve from a simple law of mixtures [71,73]. Table 2 summarizes the reviewed papers, which are discussed in the following sections.

Table 2 - Summary of nanohardness based reviewed articles [39,40,69–74]

Authors	Approach	Further details
DELINCÉ et al. (2006)	Mechanical behavior *per se*	Used different size indentations to assess the influence of nanoindentation size effect, grain size effect, natural hardening of ferrite, and reinforcement by martensite.
CHOI et al. (2009)	Prediction of macroscopic flow stress from individual properties and law of mixtures	Applied a reverse analysis to the load-displacement curve to obtain the flow curves of individual phases and predict the macroscopic behavior.
TSIPURIDIS et al. (2011)	Mechanical behavior *per se*	Assessed nanohardness in different regions of the ferrite grains and martensite islands.
GHASSEMI-ARMAKI et al. (2014)	Mechanical behavior *per se*	Assessed nanohardness in different regions of the ferrite grains and martensite islands before and after bulk tensile tests.
TAYLOR et al., (2014)	Establishment of correlations	Established correlations between ferrite hardness and YS, martensite hardness and hole expansion ratio (HER), and martensite/ferrite hardness ratio and HER.

Authors	Approach	Further details
CHENG et al. (2016a)	Prediction of macroscopic flow stress from individual properties and law of mixtures	Obtained mechanical properties of individual phases from a reverse analysis of the load-displacement curves and extrapolated these properties using a law of mixtures to predict the bulk flow curve.
ZHANG et al. (2016)	Establishment of correlations	Established correlations between ferrite center hardness and YS, ferrite center hardness and UTS, martensite hardness and YS, and martensite hardness and UTS
JAHANARA et al. (2019)	Establishment of correlations	Established correlations between martensite nanohardness and martensite carbon content, ferrite nanohardness and YS and ferrite/martensite nanohardness ratio and elongation.

Before diving into these studies individually, it is worth clarifying some aspects regarding the terms nanohardness and ultramicrohardness testing. The first refers to "hardness tests wherein the depth of indentation usually is less than about 50nm (…)" [75]. A nanometric Berkovitch diamond indenter is most commonly used, and the indentation loads usually range from 0.1-100mN. The equipment is more sophisticated than the system used for ultramicrohardness. This latter testing is commonly performed with a standard Berkowitch indenter, and indentation depths ranging from 0.1-1.0μm. The system monitors load and indentation depth [75].

3.6.1- MECHANICAL BEHAVIOR BASED ON NANOHARDNESS MEASUREMENTS

DELINCÉ et al. [69] performed nano and micro indentations in three DP steels obtained from a single grade DP steel processed through swagging (non-radial compression) classified by the authors as coarse grain, fine grain, and very fine grain. The different indentation sizes were obtained not only by different equipment (nano indenter and micro indenter) but also by varying the applied load, and consequently varying the penetration depth. Four critical depths were defined in a model according to the interaction of the plastic zone and some microstructural characteristic lengths, namely: ferrite grain size and mean inter-distance between martensite islands. These critical depths were used to determine the onset and state of full interaction of the indentation plastic zone with ferrite

grain boundaries and martensite islands, which allowed the assessment of different contributions to the material hardening.

The authors observed an initial decrease in hardness with increasing indentation depth which is attributed to geometrical strain gradient plasticity effects. After reaching a minimum level, hardness increased with the beginning of the interaction of the indentation plastic zone and grain boundaries and reached a maximum after the indentation zone of influence corresponded to a representative element of the microstructure, hence when there was an effect of second phase particles. This method was used to compare the mechanical behavior of the three studied DP steels. The main observation was that the increase in ferrite grain size and decrease of martensite volume fraction results in lower maximum hardness. However, the authors argue that differences in hardness could be overestimated in a direct comparison of nanohardness with microhardness measurements. Also, considering equivalent phase properties for the different materials and not considering grain size distribution may incur in some error. These insights were greatly deepened by TSIPOURIDIS et al. [39] and GHASSEMI-ARMAKI et al. [40] who used slightly different methodologies.

TSIPOURIDIS et al. [39] performed ultramicrohardness measurements in different regions of the ferrite grains and martensite islands. The dual-phase steel studied was a laboratory-produced steel with relatively coarse grain size. Measurements in the ferrite grain showed four regions: the center, which was not affected by any boundary (grain or phase boundary), regions affected by ferrite-ferrite boundaries (GB – grain boundaries), regions affected by ferrite-martensite boundaries (PB – phase boundaries) and finally, regions affected by both GBs and PBs. Figure 24 shows the reported mean hardness values *per* region, ranging from higher measurements in martensite, followed by, measurements on phase-boundaries, on grain-boundaries, on ferrite and close to both PB and GB, close to PB, close to GB, and ferrite grain center.

The authors explain these observed differences based on dislocation pile-up and the effectiveness of each boundary type as barriers for dislocation slip transfer [76]. Furthermore, the volume change involved in martensitic transformation induces strain in adjacent ferrite which is not heterogeneously accommodated by GNDs and causes modifications in ferrite yielding behavior [39]. Figure 25 shows a TEM image, which reveals tangled dislocation networks in the vicinity of ferrite-martensite phase boundary [39]. The ferrite center has clearly a lower density of dislocations.

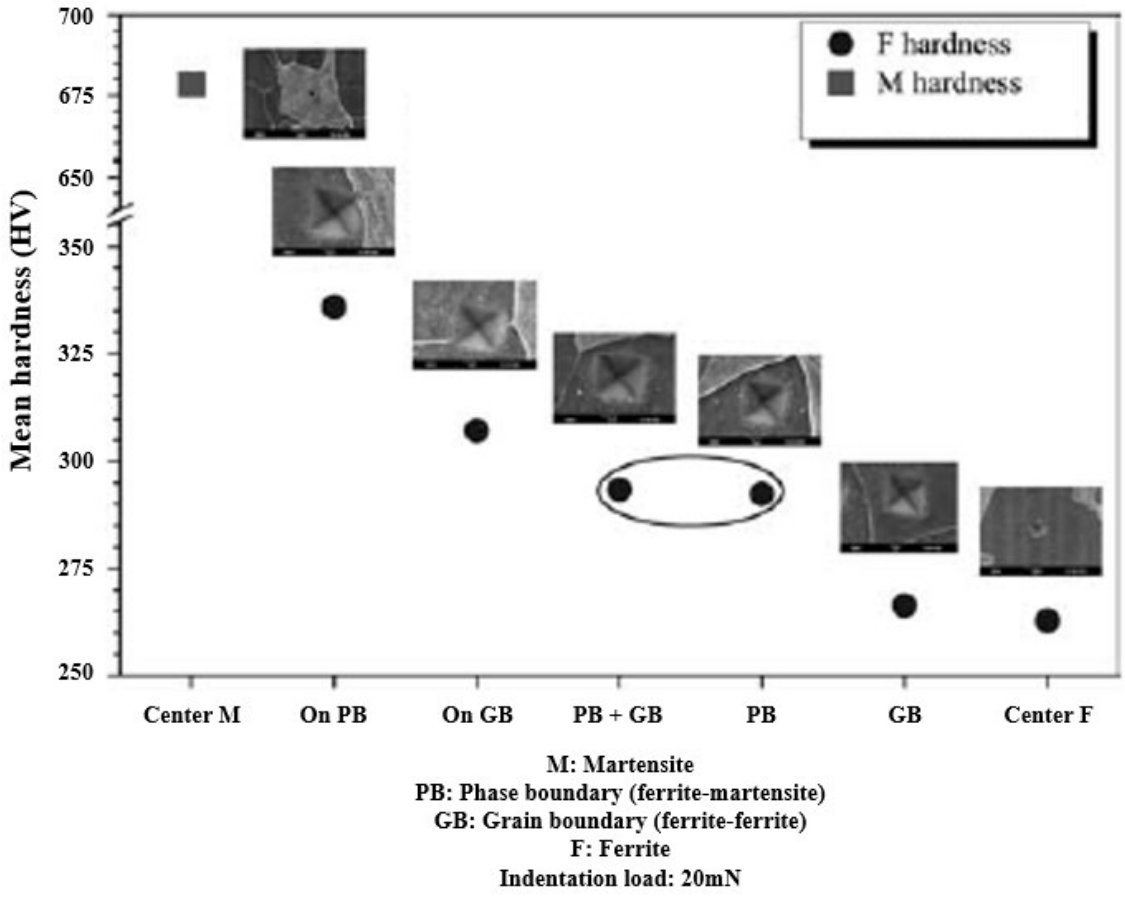

Figure 24 – Mean hardness per region (adapted from [39]).

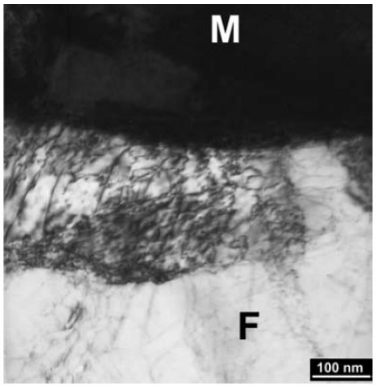

Figure 25 - TEM micrograph of dual-phase steel [39].

GHASSEMI-ARMAKI et al. [40] performed a study on a commercially produced DP980 which was partly like the one previously commented on. In their research, the nanohardness measurements were divided in three groups: 1) inside ferrite, but far from any interface (grain/phase boundary); 2) inside ferrite and close (2-3µm) to a phase boundary; 3) in martensite. The results were also separated in an as-received condition and pre-strained (5% and 7% deformation).

Regarding the as-received condition, hardness values of $3.3 \pm 0.89GPa$ and $3.9 \pm 0.95GPa$ were attained at the center of ferrite grains and near their boundaries, respectively. Figure 26a shows an example of six sites where indents were imprinted. Figure 26b shows the corresponding load/force displacement curves. After 7% tensile strain, new indents were recorded, and the results are presented comparatively in Figures 26c to 26e in cumulative size distributions. The authors report that the ferritic grain center was hardened but the regions close to phase boundaries were softened. Also, measurements of martensite hardness in the as-received and pre-strained conditions indicated martensite work hardening.

The main conclusions that can be drawn from the nanoindentation measurements in these three studies are:

- Hardness and deformation within ferrite are inhomogeneous [39,40]. Initially there is a higher density of dislocations close to phase boundaries and these regions are harder than the center [39,40]. Tensile deformation leads to work hardening of the center but softening of the initially harder regions at least up to 7% strain [40].
- Martensite yielding occurs well before UTS and undergoes considerable work hardening [40].
- Phase boundaries impose higher resistance to the movement of dislocations than grain boundaries [39,76].

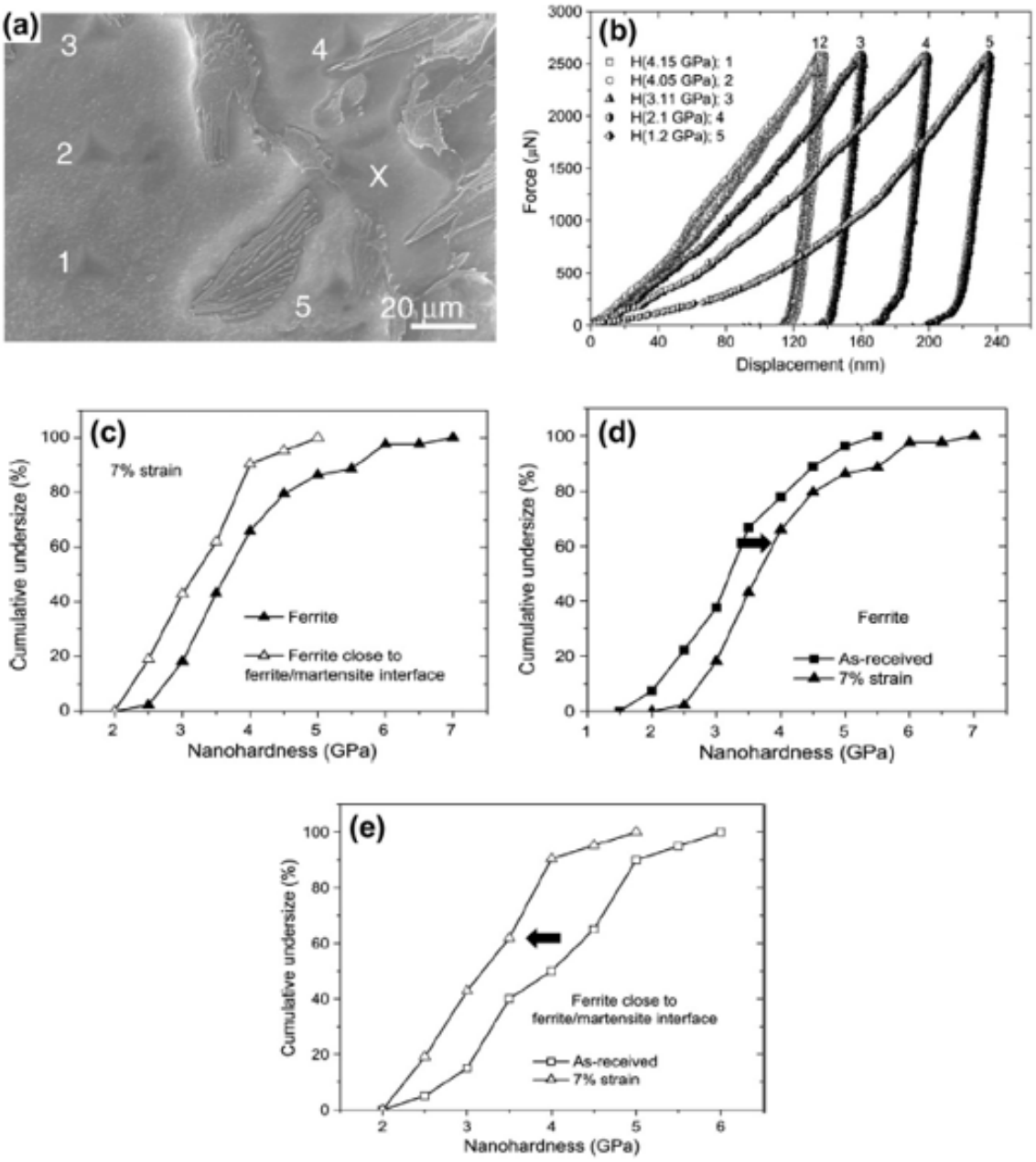

Figure 26 – (a) SEM image of DP steel, 7% uniaxial tensile strain; (b) Force-displacement curves corresponding to the nanoindentations in Fig 28a; (c) Comparison of the nanohardness distribution: ferrite interior and close to phase boundary; (d) Comparison of the nanohardness distribution: ferrite interior as-received and after 7% strain; (e) Comparison of the nanohardness distribution: indentation in ferrite, close to phase boundary as-received and after 7% strain [40].

3.6.2- DETERMINING INDIVIDUAL PHASE FLOW CURVES

Moving on to the second group of studies based on nanoindentation measurements, we have those in which the approach is to determine flow curves of the individual phases. This approach basically aims at extracting the highest amount of information possible from the load-depth curves (Figure 27). The validity of the predicted properties is tested by comparing the bulk tensile curve with the composite flow curve obtained using a simple law of mixtures (equal strain condition).

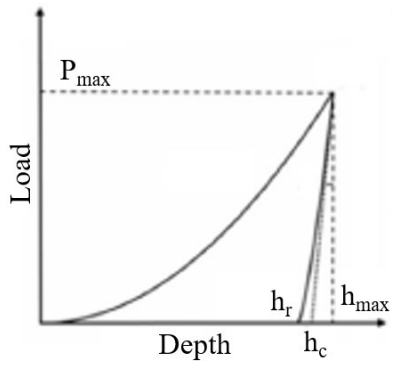

Figure 27 - Load-depth curve [71].

CHOI et al. [73] performed nanoindentations in a ferrite-bainite dual-phase steel using two spherical indenters (550nm and 3.3μm) and attempted to predict the flow behavior from the individual microphase properties. The mathematical procedure to achieve this begins with an empirical relationship between hardness and flow stress proposed by TABOR [77] (Equation 12).

$$H = \frac{P}{\pi a^2} = C\sigma \tag{12}$$

where H is hardness, P is the indentation load, a is the radius of contact, C is a constraint factor, and σ is flow stress. The characteristic deformation (ε) underneath a spherical indenter can be calculated by Equation 13:

$$\varepsilon = 0.2\frac{a}{R} \tag{13}$$

where R is the radius of the indenter's sphere.

The radius of contact (a) can be calculated as a function of the contact depth (h_c), which can be in turn estimated using the approach of OLIVER and PHARR [78] as follows (Figure 28):

$$a^2 = 2Rh_c - h_c^2 \tag{14}$$

$$h_c = h - \omega\frac{P}{S} \tag{15}$$

where h_c is the contact depth, h is the penetration depth, ω is a geometric constant (0.75 for a sphere), and S is the contact stiffness (which equals the slope of the unloading curve).

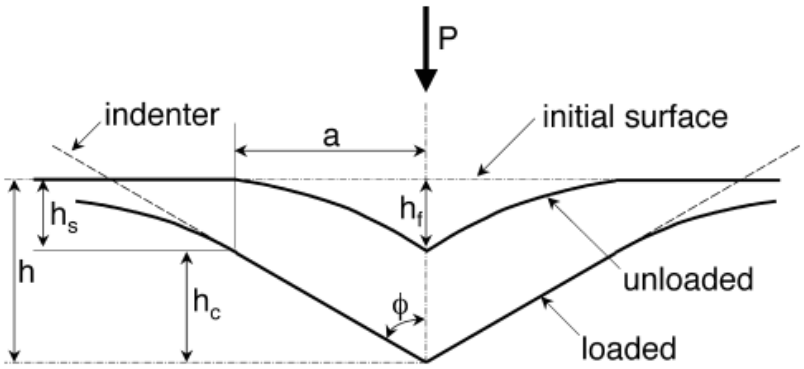

Figure 28 – Representation of the terms in the Oliver-Pharr method [78]. Note: $h_s = \omega P/S$.

Finally, to obtain the representative flow stress the constraint factor (C) must be calculated. The authors resort to Johnson's model [79]. There is a relation between the constraint factor (C) and a non-dimensional plasticity index for each deformation regime (elastic, elastic-plastic, and fully plastic), presented in Equation 16.

$$C = \frac{p_m}{\sigma_{YS}} = \frac{2}{3}\left[2 + ln\left(\frac{(E_r/\sigma_{YS})\tan\beta + 4(1-2\upsilon)}{6(1-\upsilon)}\right)\right] \tag{16}$$

where p_m is the mean load, the term $(E_r/\sigma_{YS})\tan\beta$ is the non-dimensional plasticity index, E_r is the reduced modulus (determined from Poisson's ration and Young's module of both the specimen and the indenter), and β is the slope between indenter and specimen's surface.

The constraint factor is estimated to be ~3 for a fully plastic regime. The term $\tan\beta$ is approximately equal to $\sin\beta$ for a spherical indenter and can be replaced by a/R. The Young's module and Poisson's ration considered are 210MPa and 0.3, respectively, which are typical values of steel. Finally, the representative flow stress σ_{YS} and deformation are obtained iteratively by testing arbitrary values of σ_{YS} on both sides of

Equation 16 until appropriate fitting is achieved. Figure 29 shows the obtained plots of ferrite (a) and bainite (b) representative stress and strain.

There is an obvious influence of indentation size effect so before making inferences about macroscopic phase properties, CHOI et al. [73] applied the model proposed by NIX and GAO [80] – Equation 17 – to address this issue.

$$H = H_0 \sqrt{1 + \frac{R^*}{R}} \tag{17}$$

where H_0 is the macroscopic hardness and R^* is a material length scale for the radius dependence of hardness.

In this case, H and H_0 were replaced by σ and σ_0 (macroscopic stress). The obtained flow curves are shown in Figure 30. The authors extrapolated the data and considered Hooke's law for the elastic regime. In order to obtain the composite flow curve, a simple law of mixtures considering iso-strain assumption is adopted. Figure 31 shows the bulk material tensile behavior and the predicted curve. These results show a reasonable agreement between the curves.

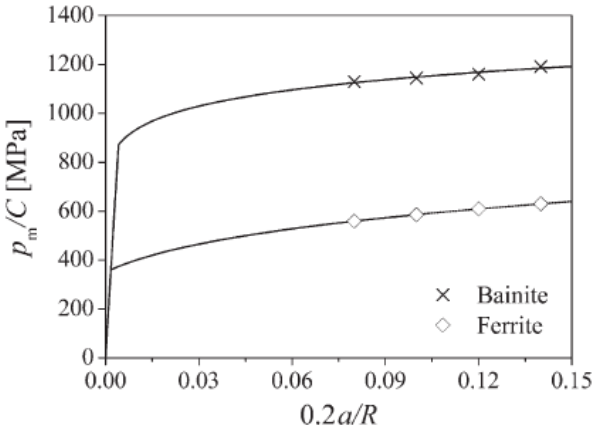

Figure 29 – Macroscopic phase flow stress versus deformation [73].

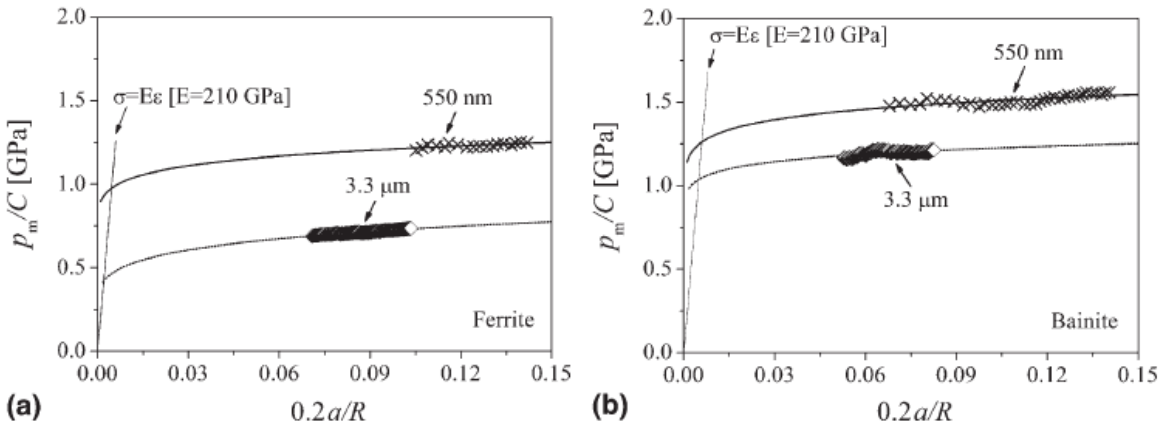

Figure 30 – Representative stress x strain of the constituent phases [73].

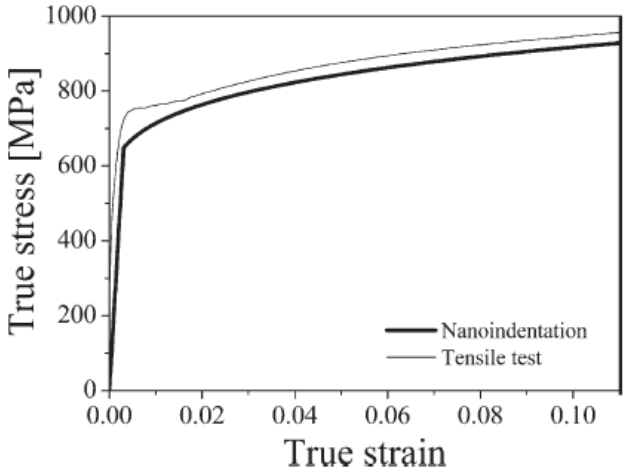

Figure 31 – Tensile test and predicted flow curves of the bulk material [73].

CHENG et al. [71] also used nanoindentation and an inverse calculation method to study individual phase plastic behavior in a dual-phase steel. The main goal of the study was to assess the influence of tempering treatments on the individual phases of a DP980. Conditions assessed are the as received condition (AsR), tempered at 250°C for 60min, and tempered at 400°C for 60min. An iso-strain law of mixtures was applied to validate the obtained individual flow curves of ferrite and martensite which led to good agreement between actual and predicted flow behavior.

The procedure to obtain the stress-strain behavior from the load-depth curve is summarized in Table 3. It basically consists in determining the elastic modulus of the phase (E), the yield strength (σ_{YS}), eliminating the indentation size effect, determining the representative stress, and the hardening exponent (n). Further details can be found in CHENG et al. [81]. Figure 32 displays the obtained results. One may observe a good

fitting between the experimental and predicted curves from the inverse calculation and nanoindentations. It is worth noting that simply applying the law of mixtures does not consider the evolution of damage, hence the predicted curves cannot anticipate failure.

Regarding the effect of tempering, the authors report a reduction in ferrite yield strength of about 6% and martensite yield strength of about 19% for the samples tempered at 250°C. For the heat treatment at 400°C, ferrite yield strength drops about 15% and martensite yield strength, 22%. Neither of these treatments is reported to influence martensite work hardening, but the ferrite's work hardening increases after tempering at 400°C, but decreases after the same treatment at 250°C.

These two studies illustrate considerable advances in the indentation technique and on the knowledge of how to extract much more information of such tests than a simple hardness value. This is of particular importance in finite element analysis, as it is a way of providing the flow curves of the individual constituents for the numerical model. It should be however noted that the predicted curves can be prolonged to infinite strain if no failure model is taken into consideration.

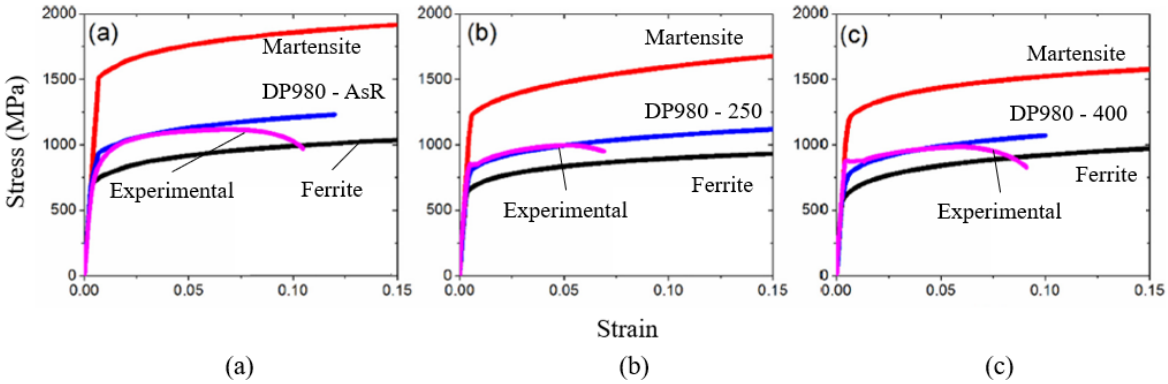

Figure 32 – Flow curves: experimental, calculated ferrite, calculated martensite and predicted composite curve. (a) As-received condition; (b) Tempered at 250°C; (c) Tempered at 400°C [71].

<table>
<tr><td colspan="2">Table 3 – Summary of the inverse calculation used by [71].</td></tr>
<tr><td colspan="2">Elastic modulus</td></tr>
<tr><td>The Oliver-Pharr method: function of unloading slope (S) and contact area (Ac). Eq. 18 is used to calculate the reduced modulus - E_r
Eq. 19 is used to obtain the elastic modulus.
E_i is the indenter's elastic modulus.
υ_i is the indenter's Young's modulus.</td><td>$$E_r = \frac{\sqrt{\pi}\,S}{2\sqrt{A_c}} \quad . \; . \; . \quad (18)$$
$$\frac{1}{E_r} = \frac{1-\upsilon^2}{E} + \frac{1-\upsilon_i^2}{E_i} \quad . \; . \; . \quad (19)$$</td></tr>
<tr><td colspan="2">Yield strength</td></tr>
<tr><td>The Oliver-Pharr method: function of maximum load and contact area</td><td>Rodriguez and Gutierrez correlation: hardness x indentation depth</td></tr>
<tr><td>$$H = \frac{P_{max}}{A_c} \quad . \; . \; . \quad (20)$$
H is hardness, P_{max} is the maximum load, and A_c is the contact area</td><td>$$H = A\sigma_{YS} + B \quad . \; . \; . \quad (21)$$
Constants A and B for an indentation depth of 50nm in ferrite and martensite are available in RODRIGUEZ and GUTIERREZ [82]</td></tr>
<tr><td colspan="2">Representative stress</td></tr>
<tr><td>DAO et al. [83] showed that there is a representative stress ($\sigma_{0.033}$) for a strain $\varepsilon_p = 0.033$ such that Eq. 22, which is independent of the hardening exponent, is valid.
C_i is the loading curvature.</td><td>$$\frac{C_i}{\sigma_{0.033}} = -1.131\left[ln\left(\frac{E_r}{\sigma_{0.033}}\right)\right]^3 + 13.635\left[ln\left(\frac{E_r}{\sigma_{0.033}}\right)\right]^2 - 30.594\left[ln\left(\frac{E_r}{\sigma_{0.033}}\right)\right] + 29.467 \quad . \; . \; . \quad (22)$$</td></tr>
<tr><td colspan="2">Hardening exponent</td></tr>
<tr><td>After having the elastic modulus, yield strength and representative stress determined, Eq. 23 can be applied to obtain the hardening exponent.</td><td>$$\sigma_{0.033} = \sigma_{YS}\left(1 + \frac{E}{\sigma_{YS}}x\,0.033\right)^n \quad (23)$$</td></tr>
</table>

3.6.3- ESTABLISHMENT OF CORRELATIONS

The last group of studies discussed in this section used nanoindentation measurements to correlate the hardness values and the bulk material properties. TAYLOR et al. [70] correlated nanoindentation hardness with tensile properties and hole expansion to assess the importance of the individual phase properties on the macroscopic behavior. Figure 33a correlates Vickers hardness with the average nanohardness and a linear relationship is established between these variables.

Figure 33b shows a strong positive linear correlation between ferrite hardness and yield strength which corroborates the idea that in a composite structure, yielding is governed by the lower-strength constituent [70]. Figures 33c and 33d correlate the hole expansion ratio (HER) of the specimens produced by mechanical punching with martensite hardness and martensite/ferrite hardness ratio, respectively.

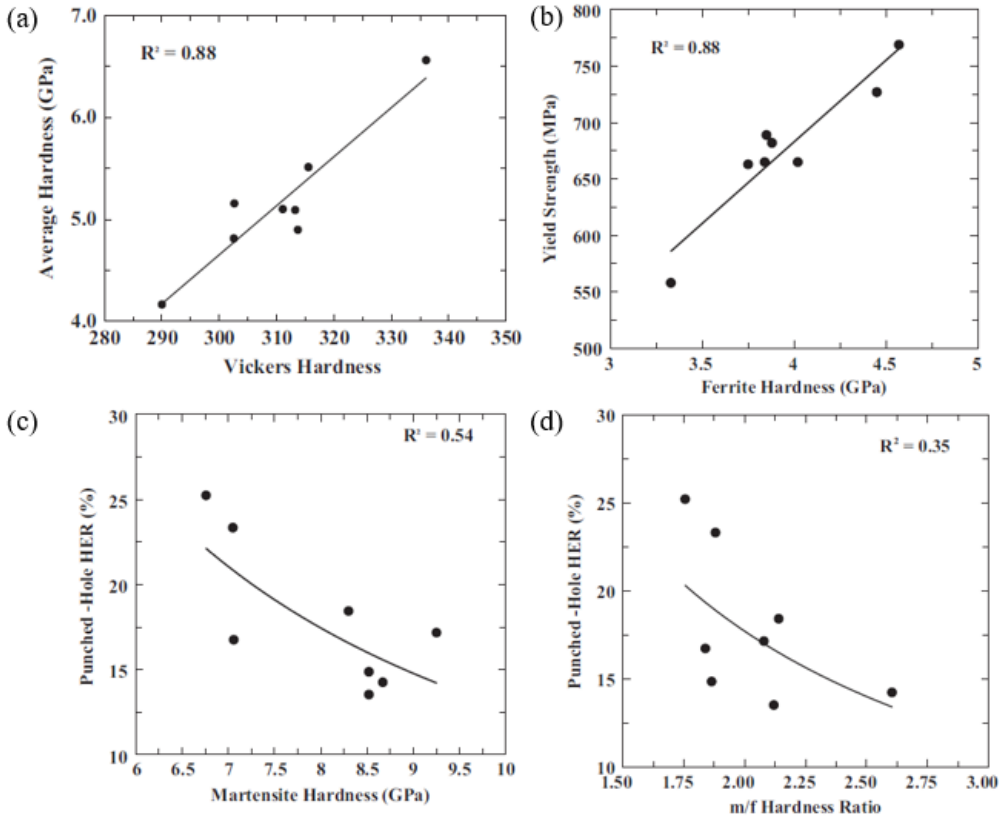

Figure 33 – (a) Vickers hardness x Average nanohardness; (b) Ferrite hardness x yield strength; (c) Martensite hardness x punched-hole HER; (d) Martensite/ferrite hardness ratio x punched-hole HER (adapted from [70]).

A brief analysis of Figure 33d shows that the HER also increases as the martensite/ferrite hardness ratio approaches 1. This leads to one of the main observations made by TAYLOR et al. [70] which is that one way of increasing HER is to increase ferrite hardness while softening martensite. The idea is corroborated by previous studies in which damage progression was outlined [84]. A higher martensite/ferrite hardness ratio implies greater strength disparity between the constituents which may cause higher strain localization and ultimately more damage nucleation in the interfaces [84].

ZHANG et al. [74] also assessed the influence of individual phase properties on a DP980 through the establishment of correlations. The authors subjected their samples to recovery annealing at 250°C, 400°C, and 550°C for 60min. The fourth condition is the as-received state. One may observe in Figure 34a a positive linear correlation between the hardness of ferrite grains center and yield strength similarly to the one reported by TAYLOR et al. [70]. In this work, however, ZHANG et al. [74] also report a positive linear correlation between martensite hardness and the ultimate tensile strength (Figure 34c) and show that there seems to be no clear trend between martensite hardness and yield strength (Figure 34b), and ferrite hardness and ultimate tensile strength (Figure 34d).

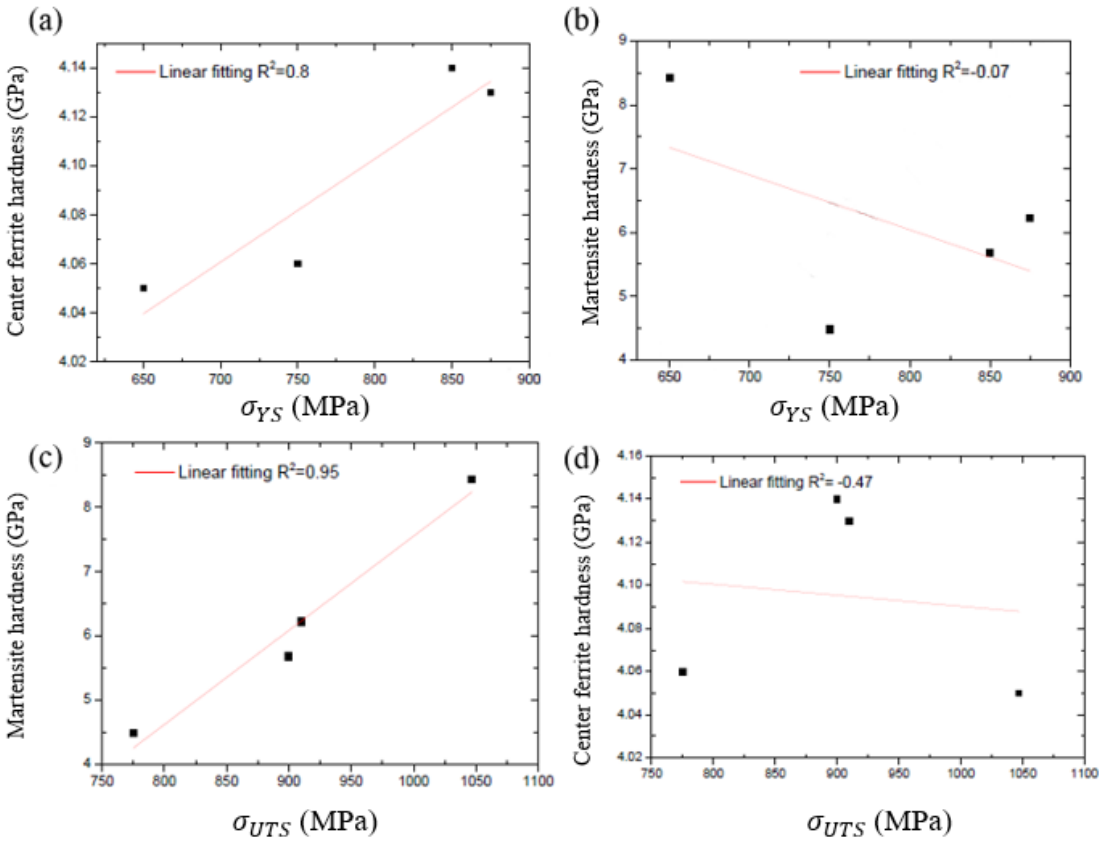

Figure 34 – Correlations: (a) Yield strength x center ferrite hardness; (b) Yield strength x Martensite hardness; (c) Ultimate tensile strength x martensite hardness; (d) Ultimate tensile strength x center ferrite hardness (adapted from [74]).

JAHANARA et al. [72] used a similar approach to study ultrafine grained (UFG) DP steels. The authors correlated nanohardness with yield strenth and ferrite/martensite nanohardness ratio with strength-elongation balance, elongation, and strain hardening exponent (Figure 35). In every case, a positive linear correlation can be observed. The plots of ferrite/martensite nanohardness ratio and the aformentioned variables (strength-elongation balance, elongation and strain hardening exponent), once again, indicate that a smaller strength disparity between the phases favors ductility. Figure 35d relates ferrite/martensite nanohardness ratio with the strain hardening exponent (in this case, $1/m$) for each of the deformation stages. These stages were identified using a modified Crussard-Jaoul analysis. The authors associate stage one with the sliding of geometrically necessary dislocations; stage two, with plastic deformation of ferrite while martensite remains elastic; stage three, with ferrite deformation being restricted by martensite islands; and stage four, with plastic deformation of both ferrite and martensite.

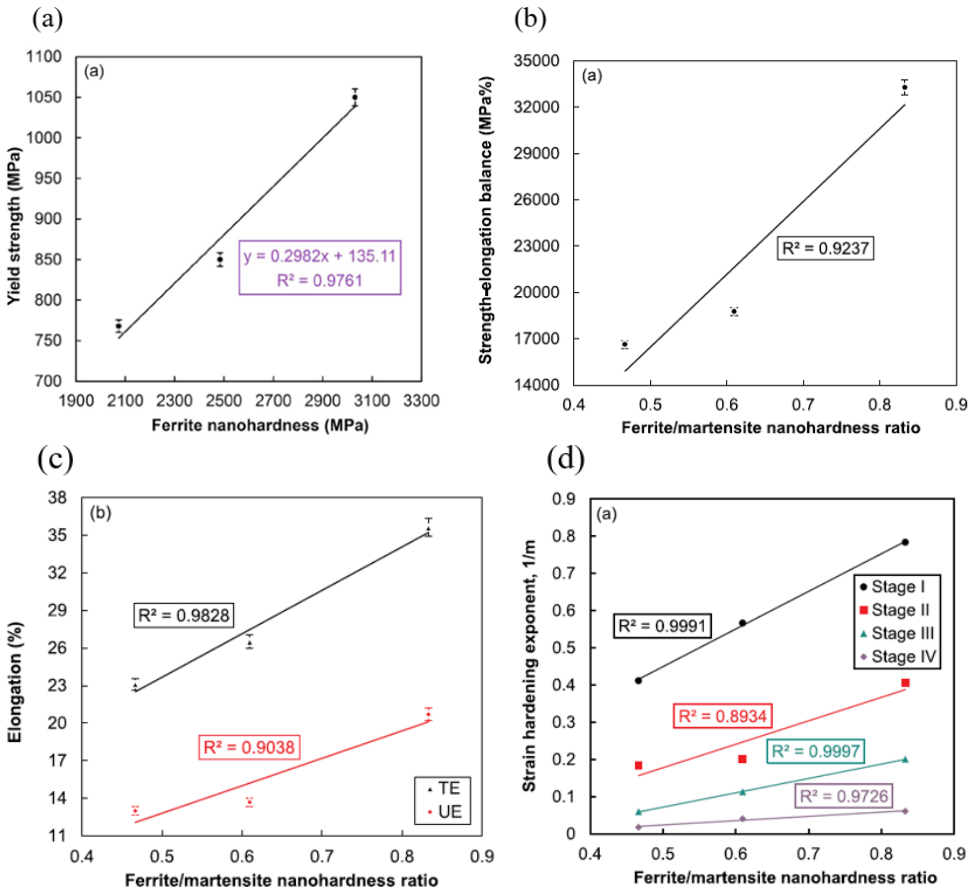

Figure 35 – (a) Ferrite nanohardness x Yield strength; (b) Ferrite/martensite nanohardness ratio x Strength-elongation balance; (c) Ferrite/martensite nanohardness ratio x Elongation; (d) Ferrite/martensite nanohardness ratio x Strain hardening exponent [72].

3.6.4 CONCLUDING REMARKS

In the selected works reviewed in this section, the researchers explore the advances in the technique of indention which made possible to perform measurements in nanoscale. This in turn allowed the probing of the individual grains in the microstructure and the assessment of mechanical behavior inside the crystals. The first insights outlined regard the influence of the boundaries (grain boundaries and phase boundaries), the substructure of dislocations and its evolution with straining. The second group explored the advances in the study of the load-depth curve which allowed the construction of flow curves of the individual constituents. Finally, the third group provided insights regarding especially nanohardness of the phases and macroscopic properties through the establishment of correlations. These observations shed light into the importance of strength disparity between the phases, illustrated by the martensite/ferrite nanohardness ratio, which impacts materials ductility and performance under conditions of stretch-flange forming. One of the things to which this relates is to the carbon content in martensite. Furthermore,

the idea that the onset of yielding is determined by ferrite and that the ultimate tensile strength is predominantly controlled by martensite is reaffirmed.

3.7- FINITE ELEMENT METHOD APPROACH

One of the pillars of materials science and physical metallurgy is the understanding of the relationship between microstructure and properties. Recently, we have witnessed the emergence and increase in the use of multiphase materials, one of them being the dual-phase steels. An important question which arises in this matter is how the constituents in the multiphase materials interact.

In the previous sections we have discussed the mechanical behavior of dual-phase steels relating bulk mechanical testing and microstructural properties, such as grain size, martensite volume fraction and morphology. We have presented some attempts to mathematically model the observed macroscopic behavior and a methodology to assess microstructural properties. The latter can also be used to indirectly evaluate the influence of the evolution of deformation on constituent properties.

In this section, a review of papers which used or were based on a numerical modelling approach with the finite element method (FEM) will be presented. Although there are available studies on composite structures and other multiphase materials the focus of this review was entirely placed on dual-phase ferrite-martensite steels.

First, some considerations regarding the use of mathematical models will be made and the concept of the finite element method will be briefly presented. Second, the concept of representative volume element will be elucidated, and finally, some aspects and insights of the reviewed papers will be discussed.

3.7.1- MATHEMATICAL MODELING AND FINITE ELEMENT METHOD

Mathematical modelling, as defined by NEUMAIER [85], is “the art of translating problems from an application area into tractable mathematical formulations whose theoretical and numerical analysis provides insight, answers, and guidance useful for the originating application”. In this context, the finite element (FE) method is a numerical procedure to solve the mathematical models, which, in turn, translate a physical problem.

The fundamental idea of the FE method is the discretization of a larger and more complex boundary problem, which cannot be solved analytically, into a subset of several discrete and simpler problems [86]. The obtained solutions are approximate solutions and the

process of solving the equations is performed iteratively until certain criteria are met. This process typically involves solving thousands of equations [87].

The procedure of performing a FEM analysis can be summarized in the following steps:

- The definition of the problem.
- Simplifying hypotheses – which are necessary to allow a reasonable computational cost (processing time).
- Definition of the mathematical models that translate the problem.
- Definition of the geometry.
- Meshing – which is the discretization of the geometry into a finite set of elements.
- Definition of boundary conditions.
- Interpreting the results and adjusting the model.

A more detailed description of the process can be found in Figure 36 [87]. Some words of caution are required when interpreting the results. It is worth noticing that the solution is only as good as the mathematical model applied [87]. Hence, no further insight can be expected beyond the information contained in the model [87].

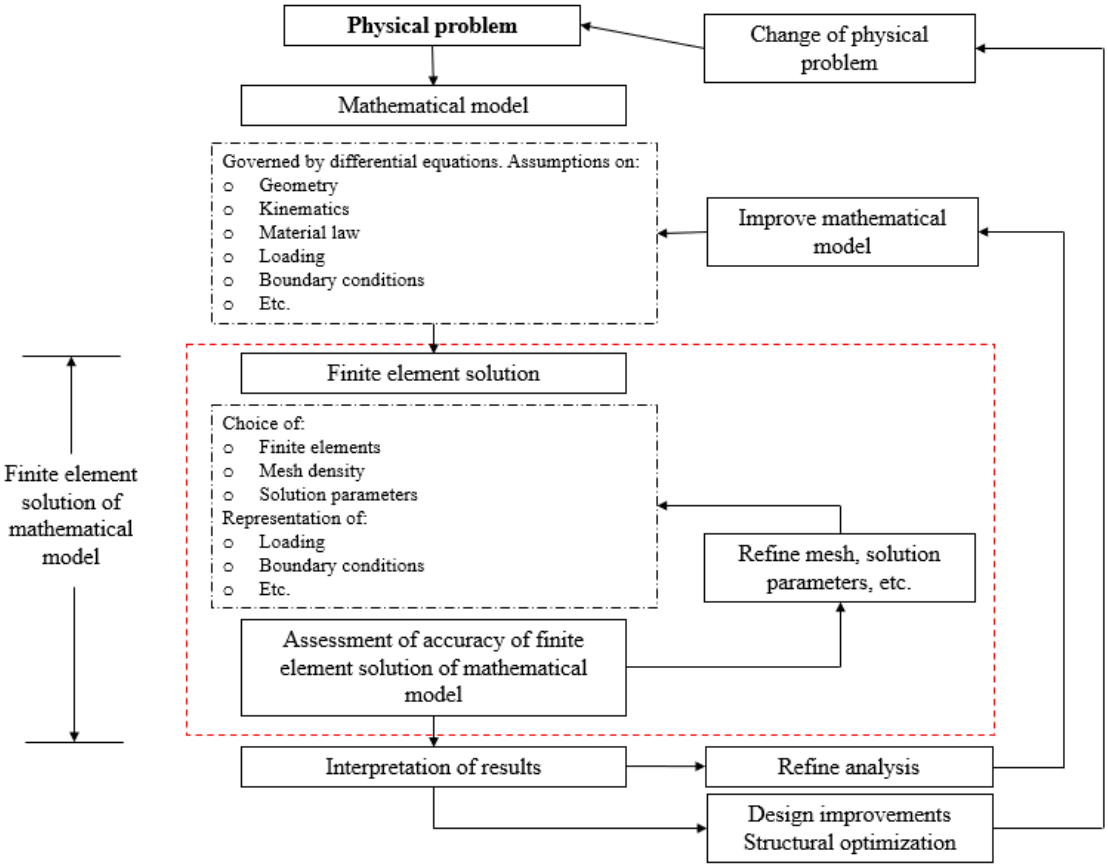

Figure 36 - The process of finite element analysis. Adapted from BATHE [87].

3.7.2- MICROSTRUCTURE MODELLING

The application of the finite element method to microstructures has been explored to provide further insight about the interaction of the phases in multiphase materials. The method allows the researcher to observe the evolution of stress and strain distribution under a certain load, which can help clarify the influence of microstructural features such as morphology, distribution, and individual phase properties. Additional mathematical models, such as damage models, can be implemented to enhance the analysis.

Recently, modifications of the finite element method to improve specific analysis have been used, for instance, the crystal plasticity finite element method (CPFEM) and the extended FEM (XFEM). The first accounts for direction dependent behavior due to crystallographic anisotropy, while the second is used in failure analysis, for it was designed to account for discontinuities. These methods will not be discussed here. For further information, the reader is directed to the specific literature [88,89].

3.7.3- REPRESENTATIVE VOLUME ELEMENTS AND MESH ASSEMBLY

The idea in microstructural modelling is to perform numerical simulations on a small region (field of view) of the microstructure, assess the mechanical behavior and plastic interaction between the phases and be able to predict the macroscopic response. The natural order of this process implies, ideally, in using actual individual phase properties. This is not a trivial task; however, some methods to do that have been previously discussed.

At this point, the concept of representative volume element (RVE) needs to be introduced. According to HILL [90], a representative volume element is a region "structurally entirely typical of the whole mixture on average" and needs to contain enough islands of the second phase [91]. The implication here is that a randomly chosen field of view is not necessarily a representative volume element. It is worth noting that some of the reviewed papers did not show carefulness regarding the choice of the volume element. Although, some evaluated the ideal size considering the number of martensite islands [91], and others averaged the obtained results of several fields of view [92].

The numerical microstructural modeling can be roughly divided in two approaches: one is based on virtual microstructures [93,94], statistically built; the other is based on geometries built with real microstructure images (see Table 3) obtained via SEM, optical microscope or even via EBSD [95,96]. Results are usually compared with the empirical

macroscopic response of the material considering the homogenization method [92] (Equations 24 and 25).

$$\bar{\varepsilon}_{ij} = \frac{1}{V}\int_V \varepsilon_{ij} dV \tag{24}$$

$$\bar{\sigma}_{ij} = \frac{1}{V}\int_V \sigma_{ij} dV \tag{25}$$

where $\bar{\varepsilon}_{ij}$ is true strain in the volume element; $\bar{\sigma}_{ij}$ is true stress in the volume element; V is the volume; ε_{ij} and σ_{ij} are strain and stress, respectively, measured on individual nodes along the extremities of the volume element.

Most methods for mesh assembly use pixel-based images. For instance, a quad-dominated mesh can be easily constructed using each pixel as an element. The color contrast can be used to distinguish the phases. As long as small precipitate particles are not considered, a reasonable mesh can be obtained. This approach, however, can lead to the problem of artificial stress concentration due to the jagged boundaries between the phases [97]. One way to solve this problem is by using vectorized images instead [92,98]. More sophisticated methods have been proposed such as the application of a boundary smoothing algorithm [97].

Virtual microstructures, as the name suggests, are not based on real images. They can be obtained using simple geometrical shapes or they can be statistically generated. Studies which used basic shapes are not discussed here, but they can be useful, for example, to assess the interaction of a single particle with the surrounding matrix [55]. One way to statistically generate a structure is by Voronoi Tessellation [94]. The technique consists in generating randomly distributed "seeds" in a two or three-dimensional space; a polygon or a three-dimensional geometry is then generated from each of these seeds.

Figure 37a shows an example of a virtual microstructure built using a MATLAB algorithm based on Voronoi Tessellation [94]. Figures 37b and 37c show the corresponding finite element mesh [94]. Figure 37d shows a scanning electron microscope image obtained by BARBOSA et al. [95] of a DP600. Figure 37e shows the corresponding mesh, built with the OOF2 software (Object Oriented Finite Element Analysis of Microstructures, by NIST – National Institute of Standards and Technology, USA) [99]. In Figure 37a, the darker areas are martensite, while the blue areas are ferrite. In Figures 37b and 37c, the corresponding colors are white for ferrite and green for

martensite. In Figure 37d, the darker areas correspond to ferritic regions, while the clear areas, martensite. In Figure 37e, martensite is in red and ferrite, in white.

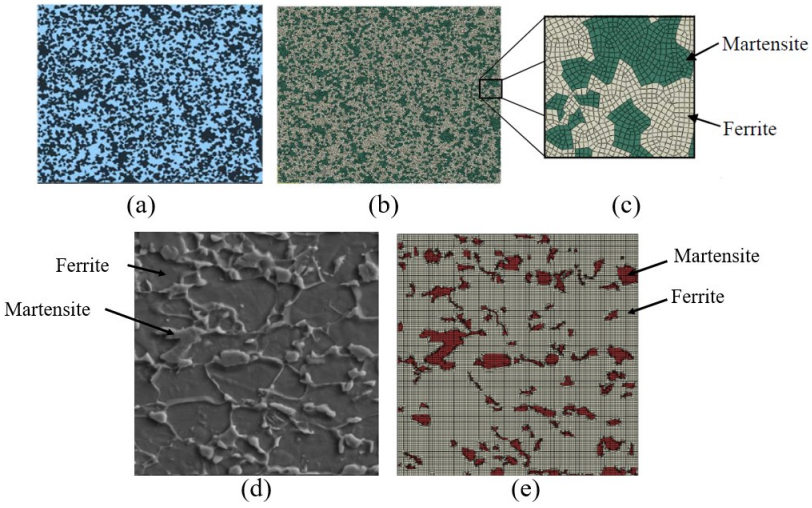

Figure 37 – (a) Voronoi Tessellation image – seeds are randomly placed in a 2D space and polygons are generated from these seeds [94]; (b) FE mesh [100]; (c) Zoom of the FEM mesh [100]; (d) SEM image [95]; (e) FE mesh [95].

3.7.4- A BRIEF DISCUSSION ON MULTIPLE RVE-BASED STUDIES

Tables 4 and 5 present a compilation of some basic information about the reviewed papers containing or fundamentally based on an RVE-FEM approach. One may observe that the mostly used program to build the model and perform the calculations is the commercial software Abaqus. Two dimensional models are still more frequently used due to the lesser computational cost than the three-dimensional models. The approach in this case is usually plane strain and sometimes, plane stress.

The RVE-FEM approach is not a recent endeavor. KARLSSON and SUNDSTRÖM [101] performed simple simulations in the 1970s with what would nowadays be considered an exceedingly coarse mesh (375 elements). Still, they were able to observe an inhomogeneous distribution of strain. Recently, LI et al. [98] performed their simulations using about 165000 elements. Most of the studies simulated a uniaxial tensile loading condition. Some exceptions were interested in the hole expansion behavior [5,102], shear behavior [98], and complex loading paths [93].

Table 4 - Reviewed papers on FEM-RVE approach. **The method used by TASAN et al.* [3] *is a modification of the finite element method and does not involve finite elements or meshing* [3,5,91–96,98,101–106].

Reference	Software	Meshing	Approach	Element type	Loading condition
KARLSON; SUNDSTRÖM (1974)	FEMFAB (developed by JAENSSON and SUNDSTRÖM, 1972)	-	2D plate model from real microstructure	Triangular elements (375 elements)	Uniaxial tensile loading, plane strain
UTHAISANGSUK et al. (2009)	Abaqus	-	3D	-	Hole expansion test
KIM et al. (2010b)	Abaqus	Grid based meshing method after boundary smoothing algorithm	One element layer extruded in the thickness direction from the original plane	C3D8R (~55000 elements)	Uniaxial tensile loading and hole-expansion test
RAMAZANI et al. (2012)	Abaqus	In-house FE generator	2D, real microstructure	CPE, plane strain elements	Uniaxial tensile loading
SODJIT; UTHAINSANGSUK (2012)	-	-	2D, real microstructure	-	Uniaxial tensile loading
RAMAZANI et al. (2013a)	Abaqus	OOF, version 2.4	2D, real microstructure, XFEM, maximum principal stress criterion (MAXPS)	-	Uniaxial tensile loading
RAMAZANI et al. (2013b)	Abaqus	In-house FE generator	2D - real microstructure; 3D - statistically constructed with randomly distributed phases	CPE4R, plane strain (2D); C3D4 - hexahedrons (3D)	Uniaxial tensile loading
TASAN et al. (2014)*	MSC Marc with DAMASK framework	Full-field crystal plasticity using spectral solver (no mesh involved)*	2D, real microstructure	NA	Uniaxial tensile loading
ZHOU et al. (2015)	Abaqus	Abaqus mesh generator after vectorizing the microstructure images	2D, real microstructure	CPE, plane strain; CPS, plane stress; CPEG, generalized plane strain elements	Uniaxial tensile loading
ABID et al. (2017)	Abaqus	MATLAB code based on Voronoi tessellation	2D, virtual microstructure	CPS4R, plane stress	Uniaxial tensile loading
BONG et al. (2017)	Abaqus	-	3D, virtual microstructure	-	Uniaxial tensile loading-unloading-loading and compression-tension test
ÇAVUSOGLU et al. (2017)	-	-	2D, real microstructure	-	Uniaxial tensile loading
BARBOSA et al. (2018)	Abaqus	OOF2	2D, real microstructure	CPE, plane strain; CPS, plane stress	Uniaxial tensile loading
LI et al. (2019)	Abaqus	Abaqus mesh generator after vectorizing the microstructure images	2D, real microstructure	CPS3, plane strain (~165000 elements)	Uniaxial tension and shear loading
ZHENG et al. (2020)	Abaqus	Pixel based	2D, real microstructure	CPE8R, plane strain	Uniaxial tensile loading

Table 5 - Reviewed papers on FEM-RVE approach [3,5,91–96,98,101–106].

Reference	Flow curve model	Focus
KARLSON; SUNDSTRÖM (1974)	Linear deformation hardening: E/100 for ferrite and E/50 for matersite	Interaction between ferrite and martensite on macroscopic straining by assessing the local distribution of strain.
UTHAISANGSUK et al. (2009)	Dislocation based phenomenological model	Study of strech-flangeability in the hole expansion process. A macroscopic simulation is also performed, and damage models are considered.
KIM et al. (2010)	Swift type empirical flow curves. Parameters are determined from empirical functions of chemical composition.	Analysis of the stretch-flange formability and evaluation of the developed algorithm for mesh generation.
RAMAZANI et al. (2012)	Dislocation based phenomenological model	Establishment of a modelling approach for predicting the initial flow curve of DP steels and comparison between uniform and banded structures.
SODJIT; UTHAINSANGSUK (2012)	Dislocation based phenomenological model	Predict the stress-strain curve from the RVE and the dislocation-based model. Different martensite contents and morphologies were assessed.
RAMAZANI et al. (2013a)	Dislocation based phenomenological model	Characterization and modeling of failure initiation of a DP steel.
RAMAZANI et al. (2013b)	Dislocation based phenomenological model	Establishment of a comparison between 2D plane strain and 3D calculated flow curves. A relationship is proposed.
TASAN et al. (2014)*	Crystal plasticity-based model	Establishment of an integrated experimental-numerical methodology (crystal plasticity modelling and μDIC).
ZHOU et al. (2015)	Dislocation based phenomenological model	Numerical simulation of uniaxial stress-strain behavior of DP steels. The influence of the element type, size of the field of view is assessed.
ABID et al. (2017)	Elastic-viscoplastic behavior; Materials parameters are obtained from regression of micro-pillar compression data.	Assessment of size and morphology effects of martensite and ferrite on mechanical behavior.
BONG et al. (2017)	Super Dislocation model: Single crystal constitutive equations; Continuum model: Swift type equations; Crystal plasticity model: parameters acquired from a basic polycrystal phase model	Critically assess the RVE-based approach by comparing different RVE modelling techniques and assess the capability of capturing loading path changes.
ÇAVUSOGLU et al. (2017)	Dislocation based phenomenological model	Attempt to predict the macroscopic flow curves of a DP600, DP800 and DP1000 from RVE numerical simulations.
BARBOSA et al. (2018)	Dislocation based phenomenological model	Attempt to predict the macroscopic flow curve of a DP600 from RVE numerical simulations using plane strain and plane stress conditions.
LI et al. (2019)	Dislocation based phenomenological model	Attempt to predict the flow curve of a DP steel and compare micromechanical simulations between uniaxial tensile loading and shear loading.
ZHENG et al. (2020)	Constitutive equation proposed by SIRIVASTAVA et al. (2016) for DP steels	Demonstrate that the imposed deformation filed (homogenous or heterogenous) implies in different mechanical response in multiphase materials.

Another important aspect of microstructural mechanical behavior in a continuum mechanics approach is the input of individual phase properties. In previous sections some methods to obtain individual phase behavior were discussed, such as nanoindentation. Also, some micromechanical mathematical models were presented. However, in Table 5, one may notice that the most widely used method to obtain the individual flow curves derives from dislocation-based phenomenological models. Although there may be some variations on the parameters of the equation, a very usual form is presented in Equation 26 according to RODRIGUEZ and GUTIERREZ [107]:

$$\sigma = \sigma_0 + \Delta\sigma + \alpha M \mu \sqrt{\boldsymbol{b}} \sqrt{\frac{1 - \exp\left(M_T k_r \varepsilon\right)}{k_r L}} \tag{26}$$

where σ is the flow stress; σ_0 is a function of chemical composition and considers the Peierls stress and solid solution effects (Equation 26a); $\Delta\sigma$ is the incremental strengthening due to carbon in solution (Equations 26b and 26c); the third term is related to dislocation strengthening as well as work softening due to recovery; μ is the shear modulus; **b** is the Burger's vector; α is a constant; M_T is the Taylor factor; k_r is an adjusting parameter that was found to inversely depend on ferrite grain size, expressed as mean linear intercept [82] – Equation 26d; L is dislocation mean free path; and ε is strain.

$$\begin{aligned}\sigma_0(MPa) = 77 + 750(\%P) + 60(\%Si) + 80(\%Cu) + 45(\%Ni) \\ + 60(\%Cr) + 80(\%Mn) + 11(\%Mo) + 50(\%N_{ss})\end{aligned} \tag{26a}$$

$$\Delta\sigma(MPa) = 30.65\ x\ \%C_{ss}^{m} - 161 \tag{26b}$$

$$\Delta\sigma(MPa) = 50\ x\ \%C_{ss}^{f} \tag{26c}$$

$$k_r = 10^{-5} {d_f}^{-1} \tag{26d}$$

where $\%C_{ss}^{m}$ is the weight percentage of carbon in martensite and $\%C_{ss}^{f}$ is the weight percentage of carbon in ferrite. The abbreviation *ss* indicates solid solution. d_f is ferrite grain size expressed as mean linear intercept.

Some examples of insights which can be obtained from an RVE-FE approach are:

- KIM et al. [5] observed that there is strain localization between the tips of two closely located martensite islands (Figure 38). In these regions, ferrite is continuous around the strain concentration area. This, in turn, indicates that a

martensite volume fraction that is neither too high nor too low will favor strain localization. Another relevant observation in this study is that in domains of higher martensite than ferrite volume fraction, hence, where ferrite is the particle and martensite is the matrix, the strain in ferrite is usually lower than the average strain.

- TASAN et al. [3] observed that the strain in many ferritic regions were concentrated in bands oriented at about 45° to 50° with the loading direction. This observation was validated experimentally through μDIC (micro digital image correlation). The localization of strain between close martensite islands reported by KIM et al. [5] was also observed in the μDIC analysis. The authors report, however, some divergences between the strain concentration regions in the simulations and the experiments (Figure 39). This problem is partly attributed to the two-dimensional approach.
- ZHOU et al. [92] were able to successfully predict the macroscale behavior using constitutive equations based on the dislocation model for individual phase properties (Figure 40). The authors used the average response of ten fields of view to obtain a representative element response.

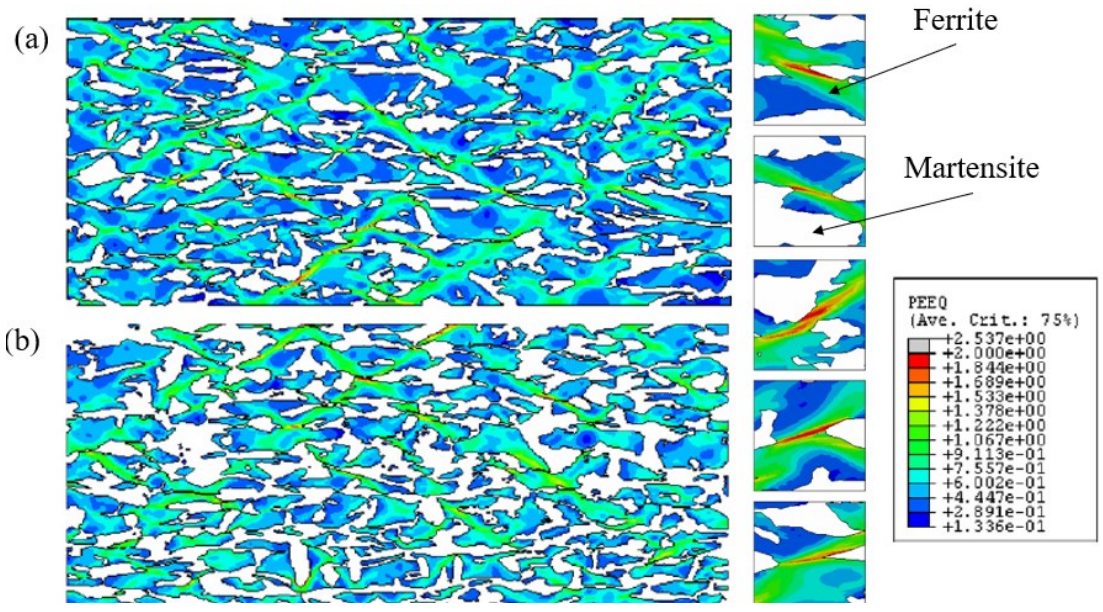

Figure 38 – Equivalent strain distribution. (a) Steel A, 34%MVF; (b) Steel B, 49%MVF. (adapted from [5]).

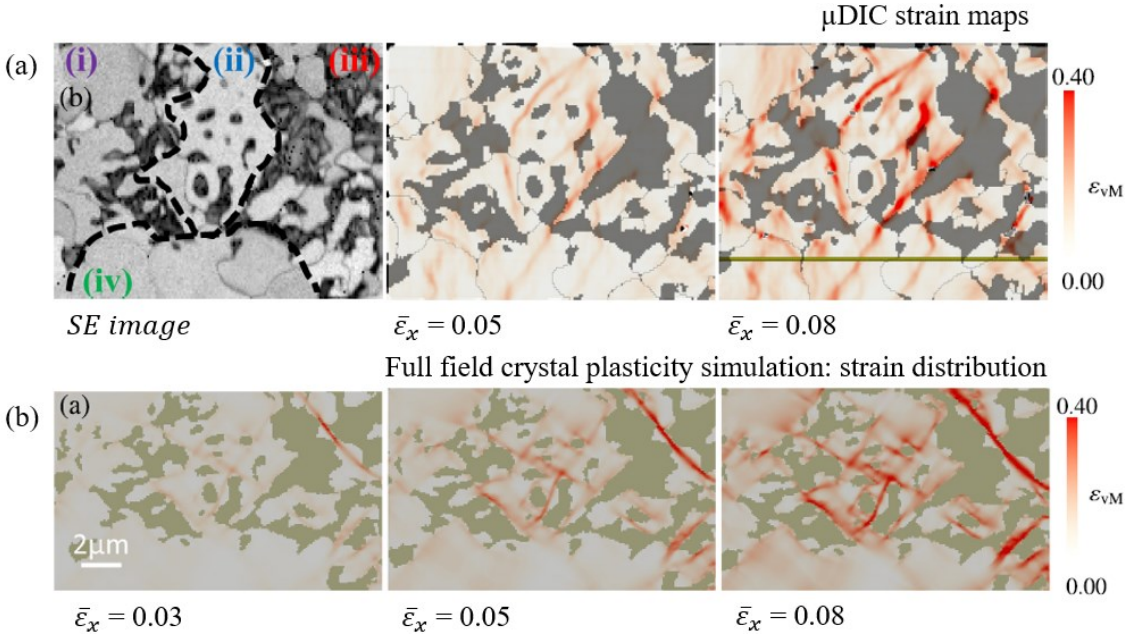

Figure 39 - (a) Left: Scanning electron (SE) microscope image – secondary electrons; center: μDIC strain map for average strain ($\bar{\varepsilon}_x$) 0.05; μDIC strain map for average strain ($\bar{\varepsilon}_x$) 0.08. (b) Full field crystal plasticity simulation strain distribution; left: $\bar{\varepsilon}_x$ = 0.03; center: $\bar{\varepsilon}_x$ = 0.05; right: $\bar{\varepsilon}_x$ = 0.08. Lighter areas correspond to ferritic regions. Darker areas correspond to martensite (adapted from [3]).

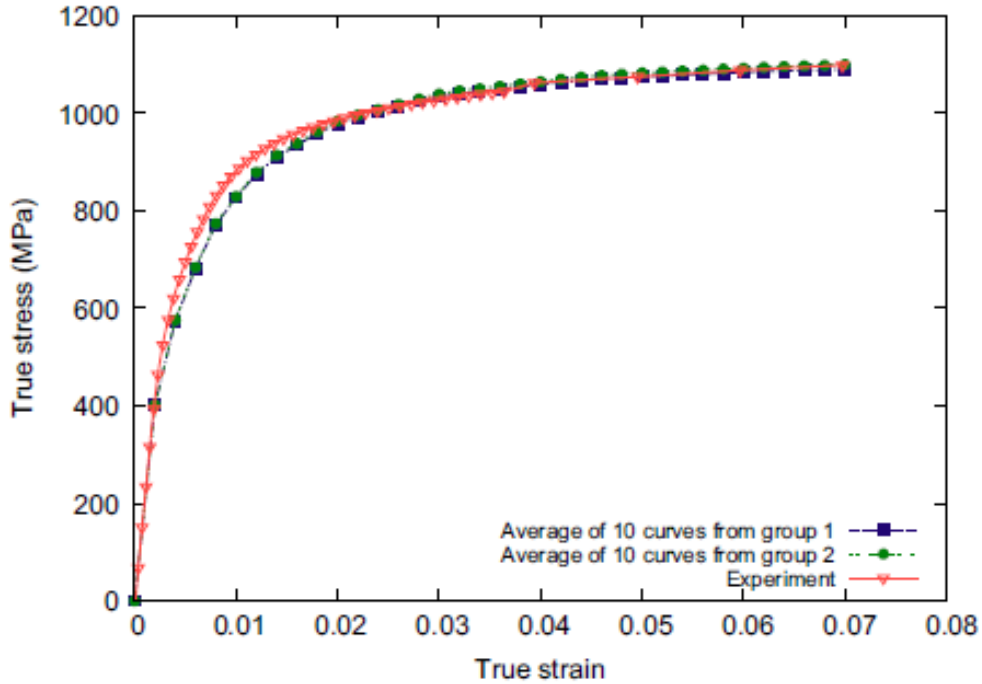

Figure 40 - Flow curves: experimental (red triangles); average response of 10 fields of view (blue squares); average response of another 10 fields of view (green circles) [92].

3.7.5- CONCLUDING REMARKS

In this section, some aspects of numerical analysis using the finite element method applied to microstructural modeling were presented. The discussion was focused on generalities associated with this field of research. The process for a finite element analysis was outlined, as well as the concept of representative volume element. The two possible approaches for mesh assembly – using real and virtual microstructure – were clarified and emphasis was given on real microstructures. It is evident that this approach is useful; however, caution must be exerted not only when building the model but also interpreting the results. In this matter, the works of TASAN et al. [3] and ZHOU et al. [92] ought to be highlighted. TASAN et al. [3] explored strain partitioning using not only numerical analysis, but also micro digital image correlation. This technique can validate or not the observed simulation results, shedding light on the model's limitations and how to improve it. Also, it provides better understanding of the mechanical behavior which is the actual goal from a metallurgical point of view. ZHOU et al. [92] performed two dimensional simulations on a simple model. Their work elucidates questions about technicalities regarding the model assembly, such as the appropriate type of element in a 2D approach. Furthermore, in line with the critique presented by BONG et al. [93], the ideal approach of microstructure modelling is to use actual micro properties as input flow curves. In this manner, the results may actually give hints about the working micromechanisms.

However, obtaining these parameters is no trivial task and empirical adjustments to the model with no regard to actual physical properties aiming at a better fitting do eventually occur. Klaus Bathe's commentary on mathematical models should once again be reminded: "the finite element solution will solve only the selected mathematical model" and "(…) all assumptions in this model will be reflected in the predicted response" [87].

4- METHODOLOGY

- Materials

The selected material for this work is a DP600, commercially produced, which was provided as thin sheets of 1.25 mm thickness. Optical spectrometry was used to determine chemical composition which is presented in Table 6.

Table 6 - Nominal chemical composition of the dual-phase steel (DP600) used in this study.

	C	Si	Mn	P	S	N
%wt.	0.0820	0.5406	2.0000	0.0279	0.0030	0.0130

- Procedures

The methodology in this work can be divided into three main steps: (1) microstructural characterization, (2) mechanical testing (Figure 41), and (3) numerical modeling (Figures 41 and 42).

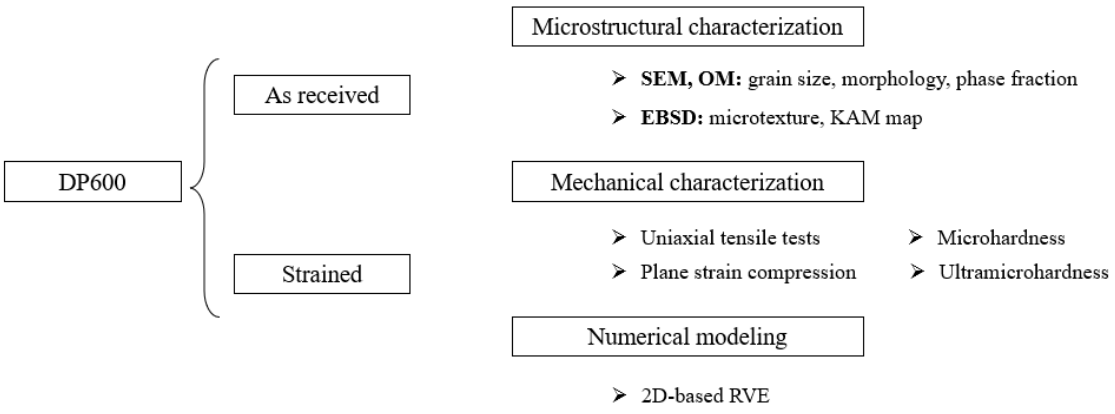

Figure 41 – Schematic representation of the project structure.

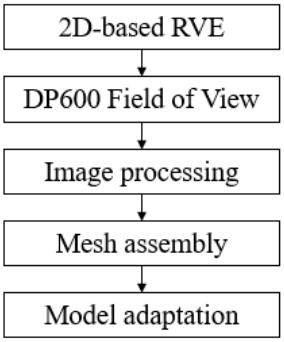

Figure 42 – Schematic representation of the steps involved in the numerical method.

Further details of each step are subsequently presented:

- Mechanical characterization of the as received material:

Uniaxial tensile specimens were machined according to ASTM A370 for a first mechanical characterization (Figure 43) with gauge lengths, widths, and thicknesses of 25, 6.25, and 1.25 mm, respectively. A universal testing machine INSTRON 5288 was used. Vickers microhardness was measured in a mesh-like arrangement on polished surfaces (ground and polishing to 1 μm diamond paste) using a Future-Tech FM700 microhardness tester. Ultramicrohardness was assessed with a Shimadzu DUH-W201S ultramicrohardness tester also in a mesh-like arrangement. In this first step, macro properties such as yield strength, ultimate tensile strength, micro, and ultramicrohardness were obtained from three workpieces.

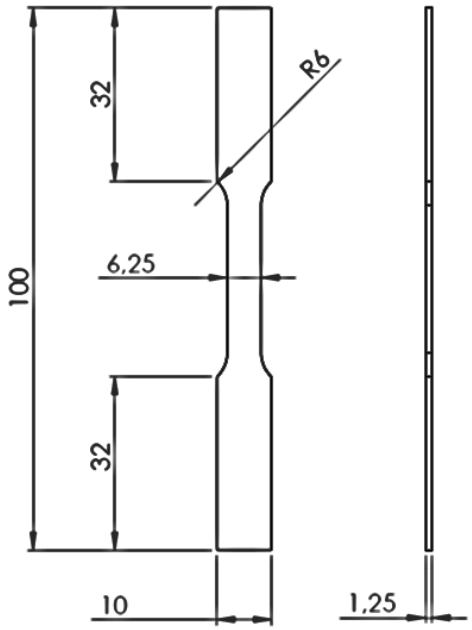

Figure 43 - Uniaxial tensile specimen geometry according to ASTM A370 standards.

- Microstructural characterization of the as received material:

Metallographic preparation was carried out down to 1 μm diamond paste and etching with 2% nital. Microstructural characterization was performed using a scanning electron microscope (SEM, secondary electrons; Inspect S50 FEI microscope) to assess martensite volume fraction (ASTM E562, point count method), grain size (ASTM E112-10, linear intercept, 20 fields of view), distribution, and morphology. Martensite volume fraction

was assessed from 20 fields of view of 60µm x 60µm and 100-point grids. Further polishing assisted with a Minimet automatic polisher was carried out in a colloidal silica dispersion for electron back scatter analysis (EBSD, EDAX TSL data acquisition system) to assess microtexture of the initial microstructure. An area of 50µm x 50µm was scanned with a minimum step size of 0.25µm and BCC cell indexing. It should be highlighted that the author was aware of likely false positive indications of martensite as ferrite and has taken this into consideration along the analysis. Also, regarding the specific area size, a larger and a smaller domain (100µm x 100µm and 25µm x 25µm) were previously scanned to determine a minimum ideal size for the analysis.

- Strain progression in plane strain compression:

To assess the effects of strain progression and partitioning, three sets of samples (total of 15 workpieces) were submitted to plane strain compression tests (Figure 44) up to certain levels of equivalent strain, namely: 0.08, 0.15, 0.50, 1.05, and 1.65. Workpiece geometrical parameters are 16 mm length, 16 mm width, and 1.25 mm thickness.

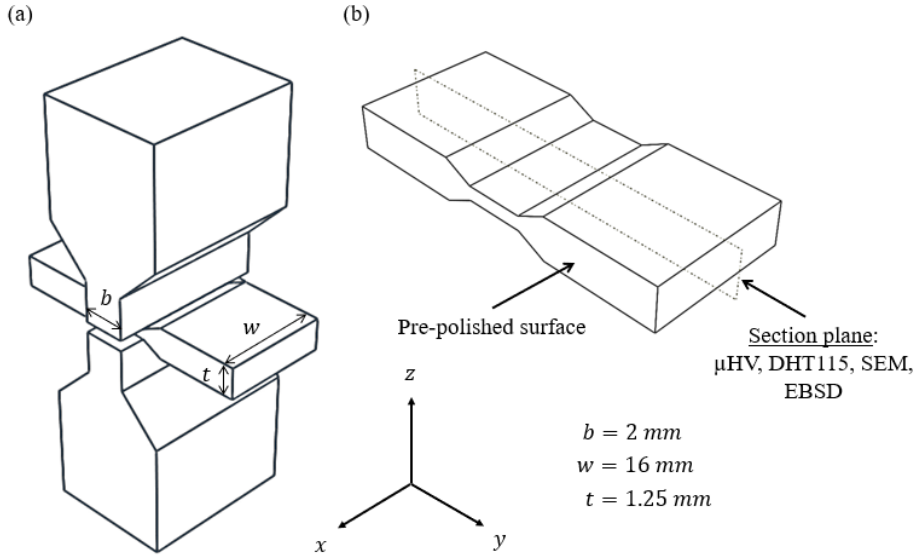

Figure 44 - Schematic representation of the plane strain compression (a) setup and (b) strained workpiece.

To assess surface effects of strain, one of these sets had a thickness surface previously submitted to grinding and polishing to a mirror-like quality, see Figure 44b. Before testing, the upper and lower surfaces were lubricated with Molybdenum Disulphide (MoS_2). Afterwards, each specimen was positioned between the dies (Figure 44a) and the upper die was pressed downwards with a crosshead speed of 1.25 x 10^{-3} mm/s (10^{-3} s^{-1}

strain rate) to impose deformation in the through-thickness direction. Loading was interrupted approximately every 5000N to re-lubricate the surfaces thus minimizing frictional effects.

The vertical load recorded immediately before each test interruption and the thickness of the deformed volume after unloading, as measured using a digital calliper with a resolution of 0.02 mm, were used to assess the relationship between equivalent stress (σ) and equivalent plastic strain (ε) during plane strain compression using Equations 27 and 28:

$$\sigma = {\sqrt{3}F}/{2A} \tag{27}$$

$$\varepsilon = -{2}/{\sqrt{3}} \ln\left(\frac{t_f}{t_i}\right) \tag{28}$$

where F is the applied load, A is the contact area between die and workpiece, t_i is the initial thickness, and t_f is the final thickness of the specimen. Tests were performed in triplicate according to the total amount of imposed strain.

The specimens with the pre-polished surfaces were immediately submitted to SEM analysis. Topographic contrast imposed by strain allowed capturing the onset of surface phenomena.

A second set of samples was cut in half parallel to the polished surface (Figure 44b) and submitted to further metallographic preparation (grinding, polishing, and etching) in both sides for microhardness and ultramicrohardness measurements in a mesh-like arrangement, as previously performed in initial state samples.

A third set was also cut in half parallel to the polished surface for SEM analysis of the internal state of deformation. One half was used for morphological analysis with secondary electrons. The other half was finished on a colloidal silica dispersion for EBSD analysis. The same parameters were used as in the initial state scanning (50 µm x 50 µm area, minimum step size of 0.25 µm, and BCC cell indexing). The obtained data was treated using the MATLAB MTEX toolbox [108,109].

- Finite element model:

A numerical model was built from real microstructure images. The microstructure was scanned to find three fields of view with distinct MVF (namely 9.7%, 22.9%, and 25.4%), which were chosen for mesh assembly. The software OOF2 [99], developed by the National Institute of Standards and Technology (NIST, USA), hosted at NanoHub platform [110] was used to build the finite element meshes and define the phase per element based on the image pixels. Simulations of plane strain compression were carried out in commercial software Abaqus [111] (Dassault Systemes). Boundary conditions are illustrated in Figure 45, along with (a) a macro view of the FE mesh, (b) the volume element phases without mesh contour, and (c) a zoomed in view of mesh details. It should be noted that the original assembly is two-dimensional, but the simulated model is a three-dimensional thin sheet of 3 elements in thickness. Total number of elements was approximately 110000 for the three volume elements (VEs) assessed.

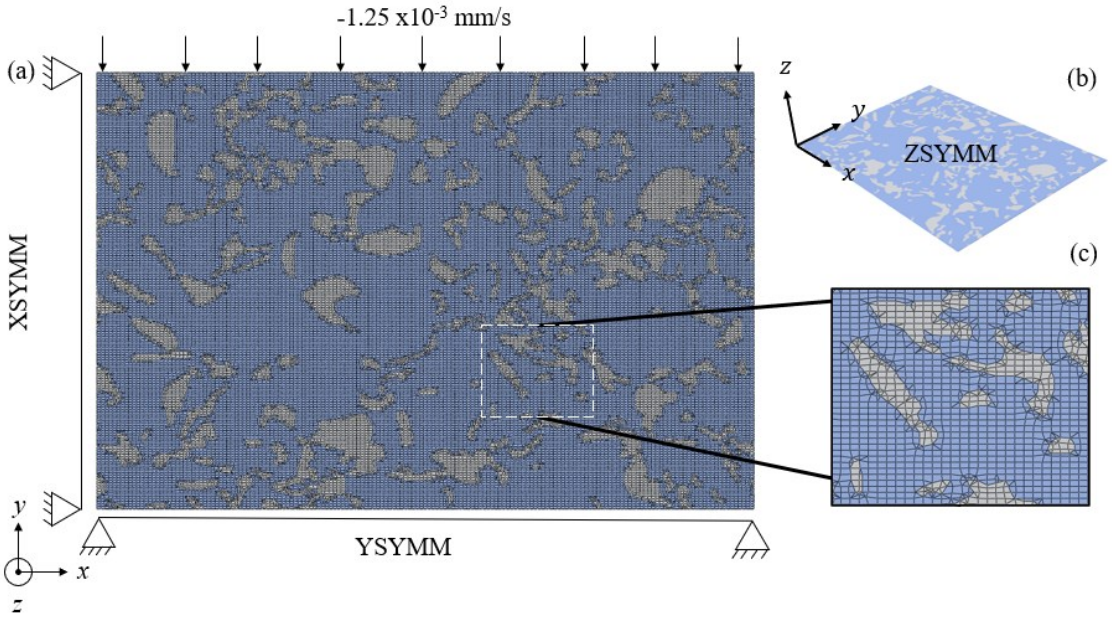

Figure 45 - Representation of the (a) FE mesh and boundary conditions, (b) volume element phases without mesh contour, and (c) zoomed in view mesh details. White: martensite, blue: ferrite.

To force plane strain condition in the 3D-model, symmetry was considered in the YZ and XZ planes, as well as in the front and back planes (ZSYMM, Figure 44b), parallel to the XY plane. A velocity of 1.25 x 10^{-3} mm/s was applied in the top nodes to impose compression.

Input flow curves of ferrite and martensite were calculated with a dislocation-based phenomenological model presented by Rodriguez and Gutierrez [107] (Equation 26).

This model is derived from the Mecking-Kocks formalism in the assessment of work hardening in FCC metals [112].

$$\sigma = \sigma_0 + \Delta\sigma + \alpha M \mu \sqrt{\boldsymbol{b}} \sqrt{\frac{1 - \exp\left(M_T k_r \varepsilon\right)}{k_r L}} \tag{26}$$

The parameters used in this model are presented in Table 7 and justified by a set of hypotheses elaborated afterwards.

Table 7 - Parameters for the flow curve input of ferrite and martensite.

Parameter	Ferrite	Martensite
σ_0	200MPa	475MPa
$\Delta\sigma$	0	414.9
α	0.33	0.33
M	3	3
μ	80000MPa	80000MPa
b	2.5 x 10^{-10}m	2.5 x 10^{-10}m
k_r	1.6949	47
L	5.9µm	0.035 µm

The first parameter in Table 7 (σ_0) regards the effects of lattice friction and nitrogen solid solution and can be calculated using previously presented Equation 26a.

$$\begin{aligned}\sigma_0(MPa) = 77 + 750(\%P) + 60(\%Si) + 80(\%Cu) + 45(\%Ni) \\ + 60(\%Cr) + 80(\%Mn) + 11(\%Mo) + 5000(\%N_{ss})\end{aligned} \tag{26a}$$

The following considerations are made: (1) all nitrogen content is considered to be in solid solution and equipartitioned; (2) P content is also considered equipartitioned; (3) Partitioning of Mn and Si were estimated by means of reverse analysis using Thermocalc® software. By measuring the MVF, we can estimate the previous austenite content and thus the initial temperature in quenching that produced the dual-phase structure. We can then consider that martensite and ferrite chemical compositions after this procedure are that of

ferrite and austenite at this initial temperature. It should thus be noted that Mn segregation was disregarded.

With these hypotheses, σ_0 for martensite is reasonable: 475MPa. For ferrite, however, there seems to be an overestimation (357MPa), which would render (along with martensite) a larger yield strength than the dual-phase structure (375MPa). Taking advantage of a broad literature review, we recur to Figure 3b, in which we plot MVF x yield strength and extrapolate the data to MVF tending to 0 (which would be pure ferrite) and thus obtain an approximate value of 200MPa for ferrite yield strength. So, one may assume $\sigma_0 + \Delta\sigma$ to be 200MPa.

The second parameter $\Delta\sigma$ is the carbon contribution to solid solution. With previous considerations regarding its partitioning, this parameter could be readily determined. However, the processing of this steel involves a tempering procedure at 180°C for 20min. After which, carbon content in ferrite tends to 0 (thus $\Delta\sigma = 0$, for ferrite) and carbon content in martensite can be estimated using a mathematical model proposed by MALHEIROS et al. [113], Equation 29:

$$C_{\alpha'} = C_{initial} - C_{initial}(0.000048T(13 + \log(t)) + 0.1275) \quad (29)$$

Where $C_{\alpha'}$ is the carbon content in martensite after tempering, $C_{initial}$ the carbon content before tempering (both in %weight), T is temperature (K), and t is time (s). From the inverse analysis using Thermocalc, $C_{initial}$ is 0.3595% wt. Martensite carbon content $C_{\alpha'}$ is thus 0.1879% wt. It should be noted that precipitation hardening was not considered.

The constant α and Taylor's factor (M) are used accordingly with Gutierrez [114] to maintain consistency with the fitting exercise of this previous author. Mean free path in ferrite is the average ferrite grain size [107], while for martensite it approximates 0.035 μm for carbon content below 0.21% [107]. The parameter k_r for ferrite is a function of its grain size, according to Equation 26d [114]. For martensite, this parameter was extrapolated from the range of values with carbon content proposed by Rodriguez and Gutierrez [115].

5- RESULTS

5.1 INITIAL STATE

Metallographic preparation and characterization were carried out in samples in the as received state. Figure 46 shows a field of view of the dual-phase microstructure. The darker regions correspond to ferrite, while the lighter regions are martensite domains. Besides these two phases, retained austenite and bainite, which can be mistaken for martensite, can also be found. To simplify the numerical model, the presence of bainite and retained austenite was disregarded. Average ferrite grain size is approximately 6 μm ± 3 μm and martensite volume fraction is ≈ 21% ± 8%.

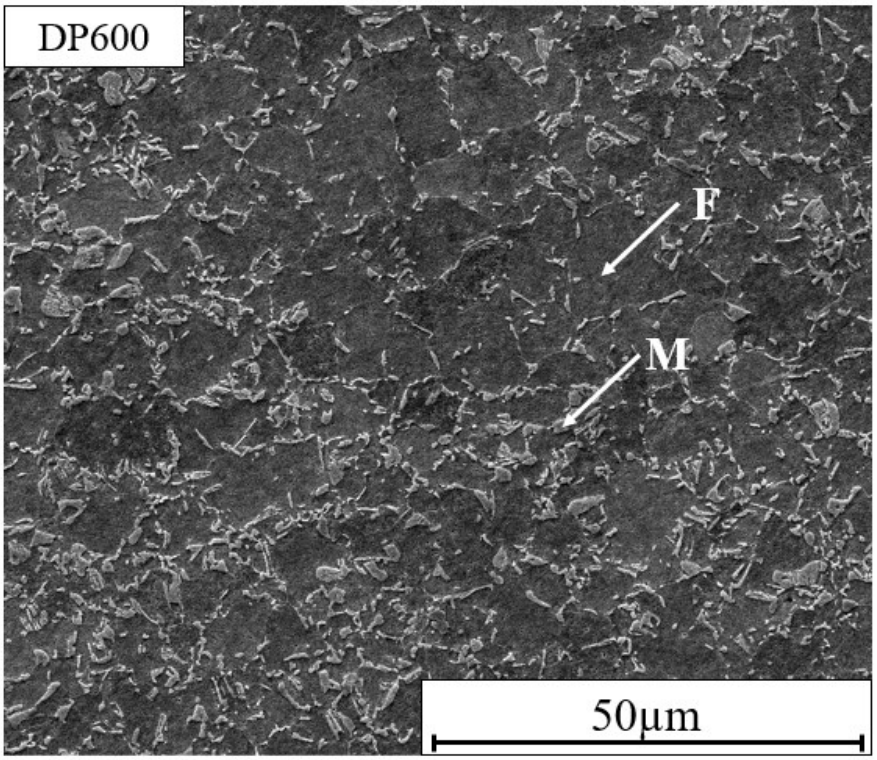

Figure 46 – DP600 microstructure. SEM, secondary electrons. Nital 2% etchant.

Mechanical characterization of the as received state was performed via uniaxial tensile test, plane strain compression, microhardness, and ultramicrohardness. The last two will only be presented in the following section along with measurements from strained specimens. Figure 47 presents the flow curves for both strain paths. One may note that the uniaxial tensile curve seems continuous, while the plane strain compression one is discrete. Both are in fact discrete. The difference is due to the interval from which data was gathered. It should be reminded that the plane strain compression tests were carried out with repeated interruptions (every 5000N) to re-lubricate the specimens.

It is evident that the corrected measurements (equivalent stress and equivalent strain) from the plane strain compression tests match well with that of the uniaxial tension. Evidently, an important difference is that the tension specimen undergoes necking at relatively low strains, thus making it unreliable to provide further information on the plastic flow. The plane strain compression one, on the other hand, achieves considerably larger strains due to the hydrostatic compressive stresses favoring the closing of cracks that may nucleate. The average engineering responses were 376 MPa ± 11MPa yield stress, 651 MPa ± 17 MPa ultimate tensile stress, 0.19 ± 0.01 uniform elongation, and 0.32 ± 0.02 total strain. Such UTS along with a ferrite-martensite microstructure characterizes a DP600. The hardening behavior seems parabolic in both strain paths up to $\varepsilon \approx 0.3$ and approximately linear from ~0.30 to 1.65, for plane strain compression.

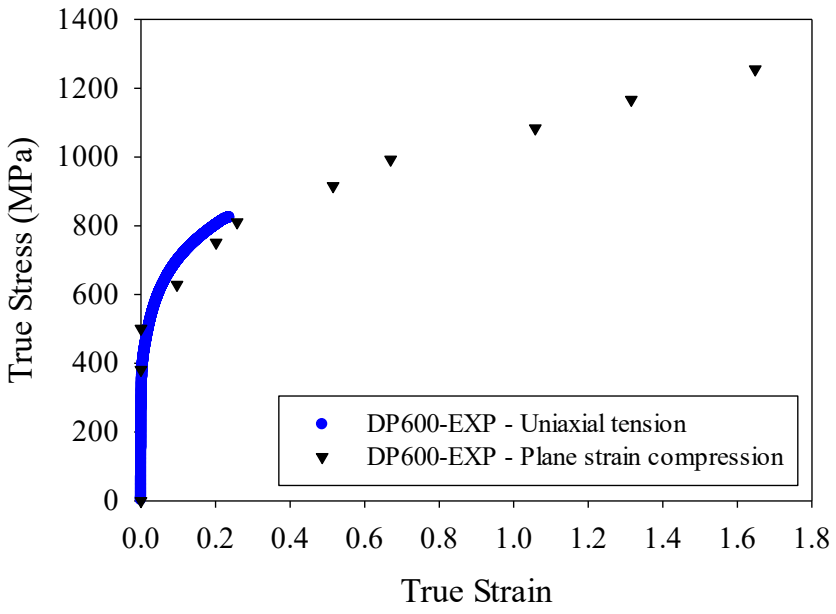

Figure 47 – Flow curves: plane strain compression and uniaxial tension. DP600, $\dot{\varepsilon} = 10^{-3}s^{-1}$. Room temperature.

5.2 STRAIN PROGRESSION UNDER PLANE STRAIN COMPRESSION

As previously mentioned, three sets of specimens were submitted to plane strain compression up to certain levels of equivalent strain (0.08, 0.15, 0.50, 1.05, and 1.65). One of these sets had a thickness surface submitted to polishing to a mirror-like quality prior to testing. Afterwards, these surfaces were immediately analysed via SEM to examine the onset of macrostrain features. These features provide topographic contrast that could be captured with secondary electrons. The first set of results is presented in Figure 48.

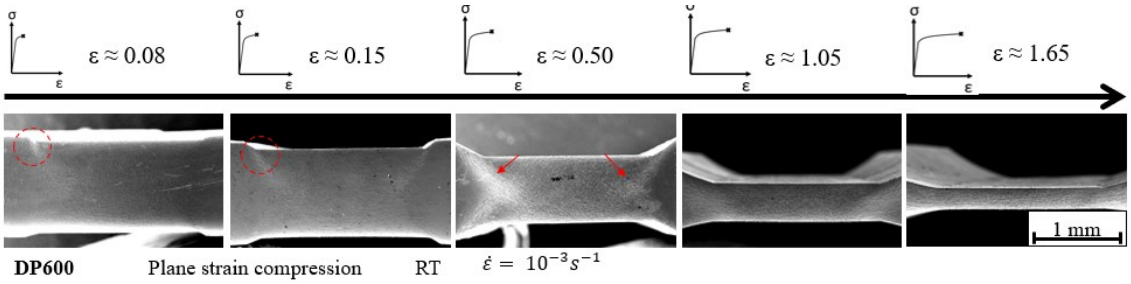

Figure 48 – SEM images of strained pre-polished surfaces. Plane strain compression, DP600. Equivalent strains of 0.08, 0.15, 0.50, 1.05, and 1.65. RT: room temperature, $\dot{\varepsilon} = 10^{-3}s^{-1}$.

It is possible to observe shear bands beginning to form in an equivalent strain of 0.08. These bands originate in the corner region of the specimens in contact with the die and are characteristic of plane strain compression. They are thus macro-scale shear bands and will be referred to as MSBs. As the strain progresses, these MSBs become more evident and take the shape of a double X, that can be clearly distinguished for 0.50 strain. After further deformation, the overlapping of shear bands makes the double X shape indistinguishable likely due to the superposition of several MSBs.

Since the MSB regions have undergone further work hardening than the rest of the specimen, indirect indications of their presence by means of hardness measurements are expected. In Figure 49, measurements of (left) microhardness and (right) ultramicrohardness performed in another set of specimens that were sectioned in the middle (see Figure 44, section plane) are presented.

Microhardness measurements show clear indications of harder regions until an equivalent strain of 0.50. After that, measurements become uniform due to the overlapping of MSBs at the center of the compressed region. Nevertheless, in the transitioning portion, which is deformed, but not directly in contact with the dies, there remains indications of MSBs. Ultramicrohardness color coded maps are shown on the right side of Figure 49. There is, however, no clear indication of said shear bands, which are on a macro-level. It should be noted that micro-indentations are in the order of 55 μm, while ultra-micro-indentations are in the order of 10 μm. This is the same order of magnitude as the ferrite grain size. It is thus likely that a higher variability in measurements occurs due to varying contribution of each phase instead.

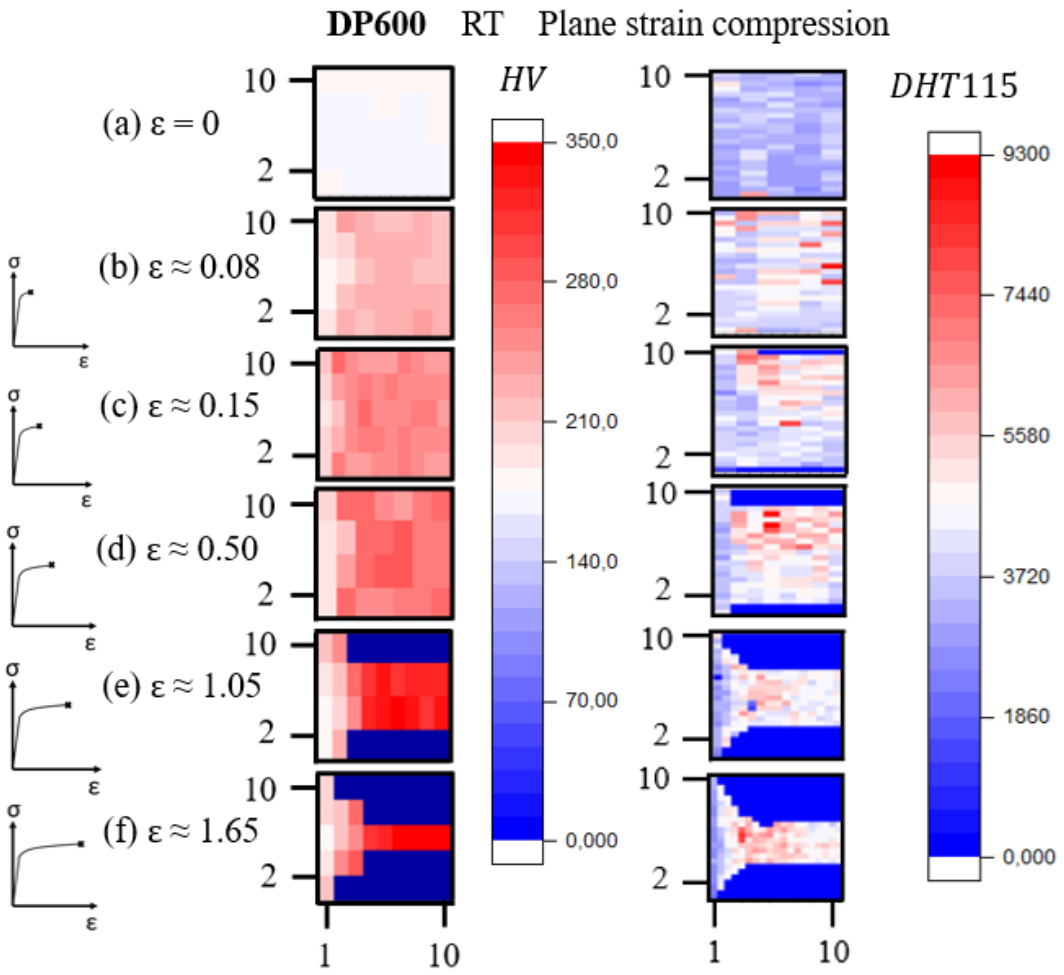

Figure 49 – Microhardness (left) and ultramicrohardness (right) color maps for different equivalent strains (0, 0.15, 0.50, 1.05, 1.65). DP600, plane strain compression. RT: Room temperature, $\dot{\varepsilon} = 10^{-3}s^{-1}$.

Figure 50 presents surface effects in a lower scale. As indicated by the (a) set of Figure 50, the (b) set illustrates regions of crossing MSBs. For an equivalent strain of 0.08, one may observe the onset of step formation in the surface. These steps become more evident for 0.15 and 0.50 strain. In this last level, dips which are possibly martensite domains that did not deform outward as much as ferrite are also evident. As strain progresses, these dips are closed as outwardly deformed ferrite grains are compressed against them. Considering the scale of analysis, these phenomena seem to have originated not only within grains but also from micro-scale shear bands formed due to contrasting mechanical properties, distribution, and morphology of the constituent phases. Further insights regarding the latter will be discussed with the FE model.

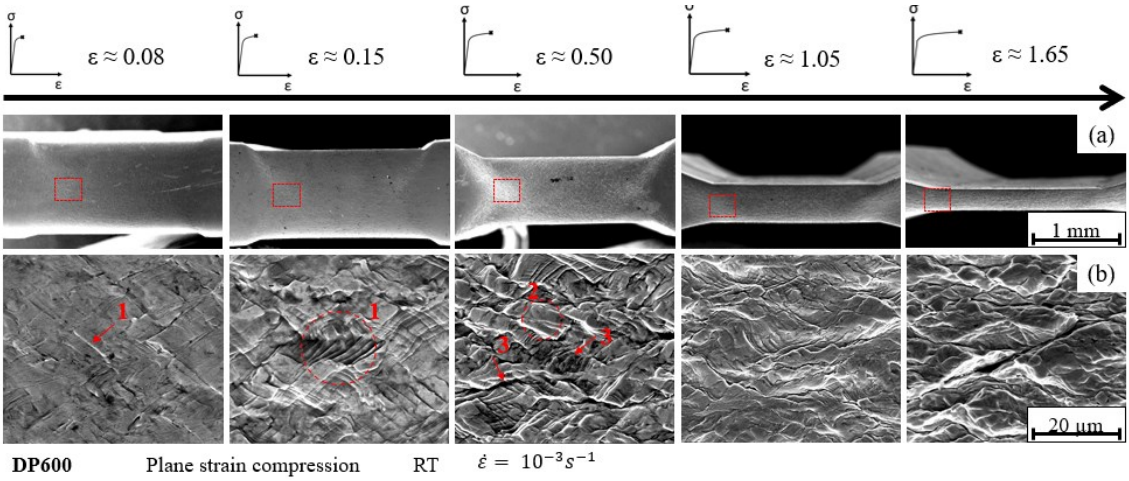

Figure 50 – a) Strained pre-polished surface; b) Strained pre-polished surface in higher magnification. DP600, plane strain compression. Equivalent strains of 0.08, 0.15, 0.50, 1.05, 1.65. Indications: (1) – Steps; (2) Ferrite domain; (3) Dips. RT: room temperature. $\dot{\varepsilon} = 10^{-3}s^{-1}$.

On a similar scale, Figure 51 presents SE images of the internal surface submitted to metallographic preparation after testing (see Figure 44, section plane). The etched surface allows observing the overall size and shape of the constituents. It is difficult to spot significant changes from equivalent strains of 0.08 to 0.50. From 0.50 to 1.65, ferritic regions become flattened, and martensite islands can be clearly seen in alignment perpendicular to the loading direction. For 1.65 equivalent strain, the microstructure takes a wave-like pattern of ferrite around martensite islands that seem to be strained as well.

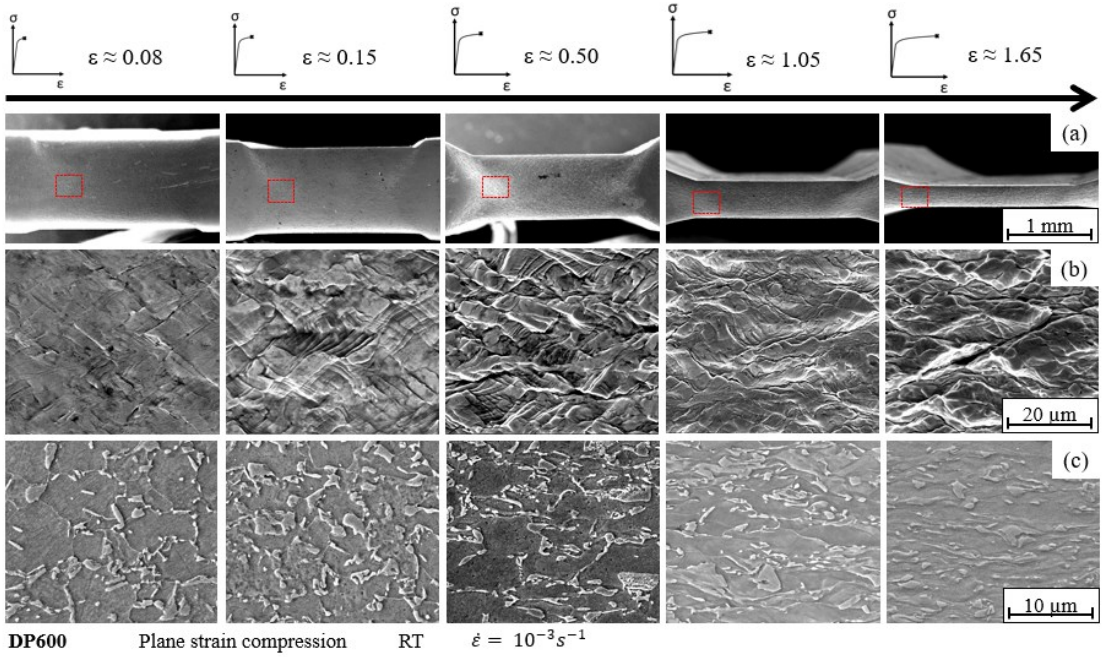

Figure 51 – a) Strained pre-polished surface; b) Strained pre-polished surface in higher magnification; c) Internal section of strained specimens (nital 2%). DP600, plane strain compression. Equivalent strains of 0.08, 0.15, 0.50, 1.05, 1.65. RT: room temperature. $\dot{\varepsilon} = 10^{-3}s^{-1}$. A magnified version of Figure 51 is presented in the Appendix.

The smallest features assessed in this study were provided by the EBSD analysis. Figure 52 presents in the left side image pole figures (IPF) and, in the right side, kernel average misorientation (KAM) maps. One may note that not all previously assessed strain levels are presented, which is due to the difficulty in properly indexing the excessively strained specimens. The analysis was thus limited to 0.50 equivalent strain.

The IPFs of the strained specimens (b-d) strongly indicate that fragmentation takes place at severely strained areas within the original ferrite grains. Nevertheless, grain orientations seem randomly distributed suggesting that there is no apparent association of the most strained areas with any particular orientation, as reported by HAN et al. [116]. This is an indication that strain concentration is most likely more correlated to the distribution, size, and shape of the microconstituents.

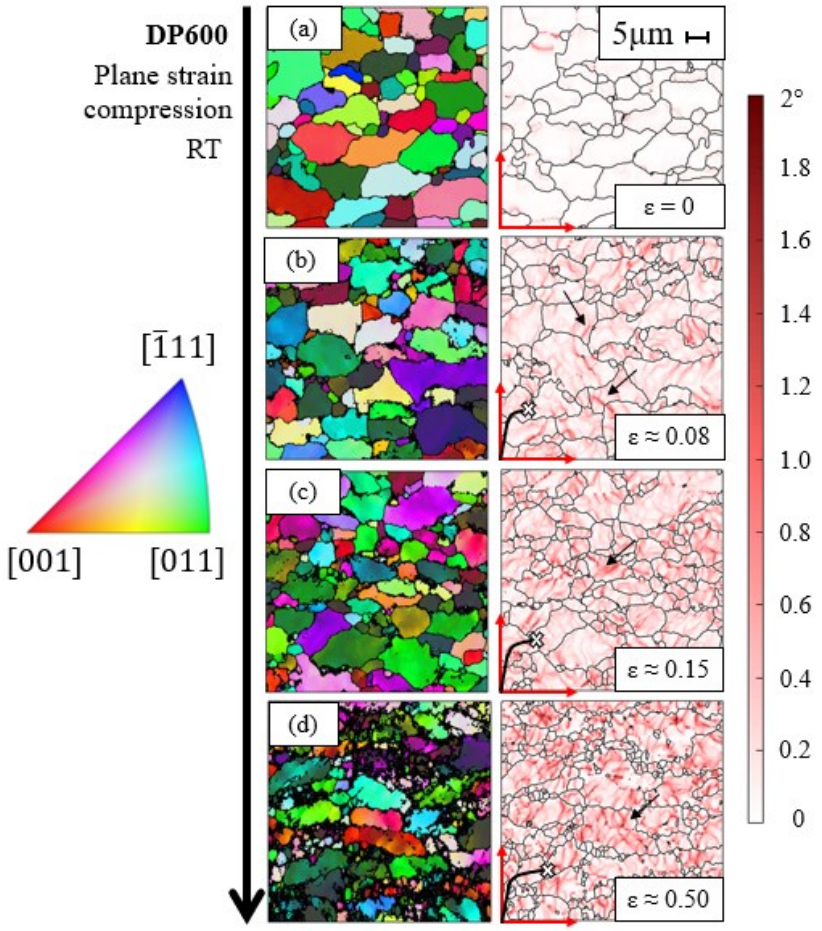

Figure 52 - EBSD: Inverse pole figure (left) and kernel average misorientation (right) maps for the initial state and different levels of strain: (a) as-received, (b) 0.08, (c) 0.15, (d) 0.50. Black arrows indicate slip bands. DP600, plane strain compression. RT: room temperature. $\dot{\varepsilon} = 10^{-3}s^{-1}$.

The associated KAM maps are presented in the right side of Figure 52. There aren't highly misoriented regions in the unstrained specimen. However, for ε ≈ 0.08, 0.15, and 0.50

slip bands (or deformation bands) are evident. The progression of strain leads to more profuse misoriented regions and to higher levels of misorientation, indicated by the increasing number of slip bands and more intense shades of red. Since the analysis was based on BCC cell indexing, it is difficult to distinguish ferrite and martensite domains. It is thus not clear whether there are preferential sites for these slip bands. However, they seem to be arranged mostly inclined with 45° and 135° slope to the loading direction. It should also be noted that these deformation bands within the grains can manifest surface effects such as the small steps observed in Figure 51b.

5.3 RVE ANALYSIS

Static simulations were carried out in three fields of view of approximately 45µm x 30µm and different martensite volume fractions, namely 9.7%, 22.9%, and 25.4%. The obtained flow curves (Von Mises equivalent stress versus plastic equivalent strain) are presented in Figure 53, along with the experimental DP flow curves and the input data for ferrite and martensite from the previously discussed dislocation-based model. One may verify a reasonable fit between the 22.9% MVF volume element (VE) and the experimental results, which thus allows one to consider this a representative volume element. The same cannot be said about the 9.7% and 25.4% MVF VEs, which underestimate and overestimate the experimental response, respectively.

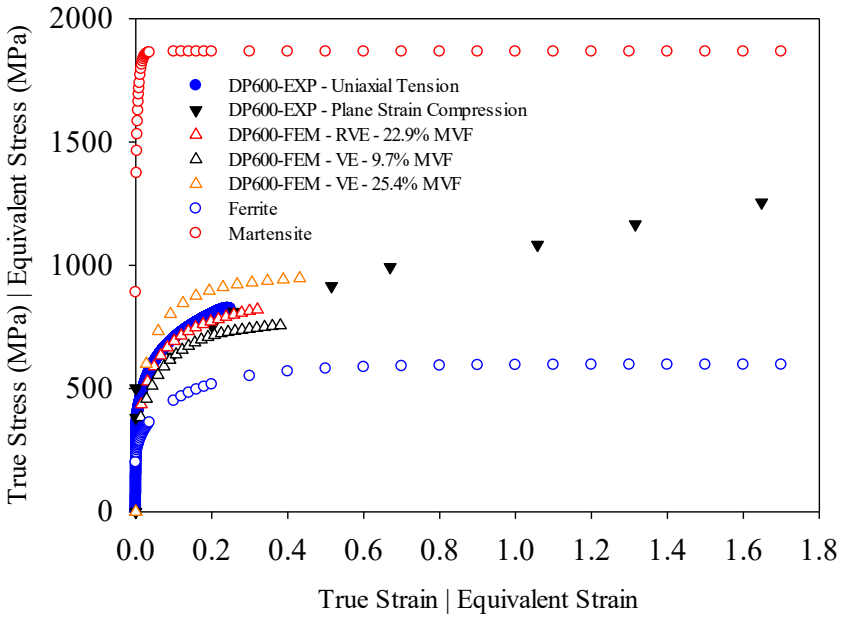

Figure 53 - Experimental, numerical, and input flow curves. DP600, uniaxial tension (experimental) and plane strain compression (experimental and numerical). Ferrite and martensite input flow curves for the numerical model (dislocation-based hardening model). Volument elements of 9.7%, 22.9% and 25.4% MVF.

After defining a representative volume element, a reliable assessment of other outputs obtained from this simulation can be made. Figure 54 presents (left) Von Mises equivalent stress in a mirrored image of the (right) plastic equivalent strain for (a and b) 0.08, (c and d) 0.15, and (e and f) 0.30 equivalent strain.

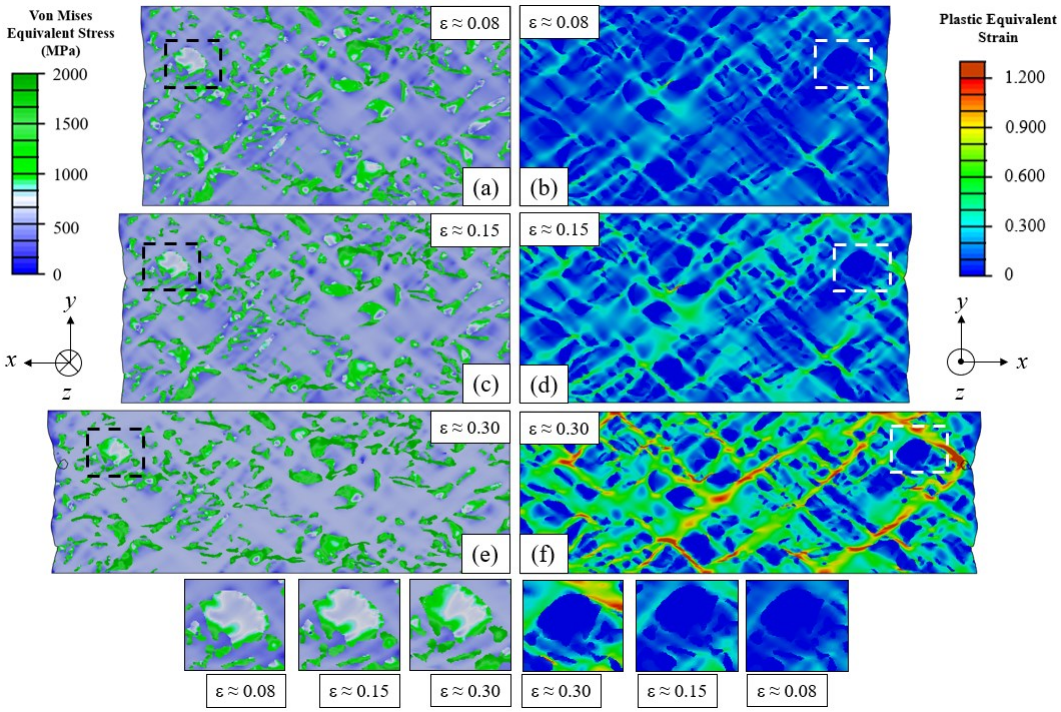

Figure 54 – (Left) Von Mises equivalent stress and (right) plastic equivalent strain. DP600, plane strain compression. Global equivalent plastic strain levels - (a) and (b): 0.08; (c) and (d): 0.15; (e) and (f): 0.30. Below: zoomed in view of (left) Von Mises equivalent stress and (right) plastic equivalent strain.

The formation of shear bands is evident in ferritic regions especially between martensite islands with a 45° or 135° slope with the loading direction (see Figures 55b, 55d and 55f, which show plastic equivalent strain of ferrite only). These shear bands will be referred to as micro-shear bands due to their origin from microstructural features. Preferential sites for strain concentration may lead to small deviations in the micro-shear bands from their optimal slope, since the bands remain mostly in ferrite.

In terms of stress, bands can also be observed in ferrite. However, higher absolute levels are naturally observed in martensite. Qualitatively, one may argue that stress concentrates mostly in martensite, while ferrite accommodates most strain. If one observes the zoomed in images in the left side of Figure 55, one may note the progression of stress within a martensite island. A comparison with the zoomed in images of the right side of Figure 55, which show the equivalent plastic strain in the same region, reveals that the outer portion of the martensite island which reaches higher levels of stress first is closer to a

shear band crossing a ferrite region. Hence, stress concentration in martensite occurs along with strain concentration in adjacent ferrite.

Although these micro-scaled bands occur mostly in ferrite, numerical results indicate that thin martensite plates can be locally submitted to considerably high strains when in the path of a shear band through ferrite (see zoomed in images in the bottom left side of Figure 55). There is also clear strain concentration in ferrite regions situated between close martensite islands as reported by previous authors [3,5].

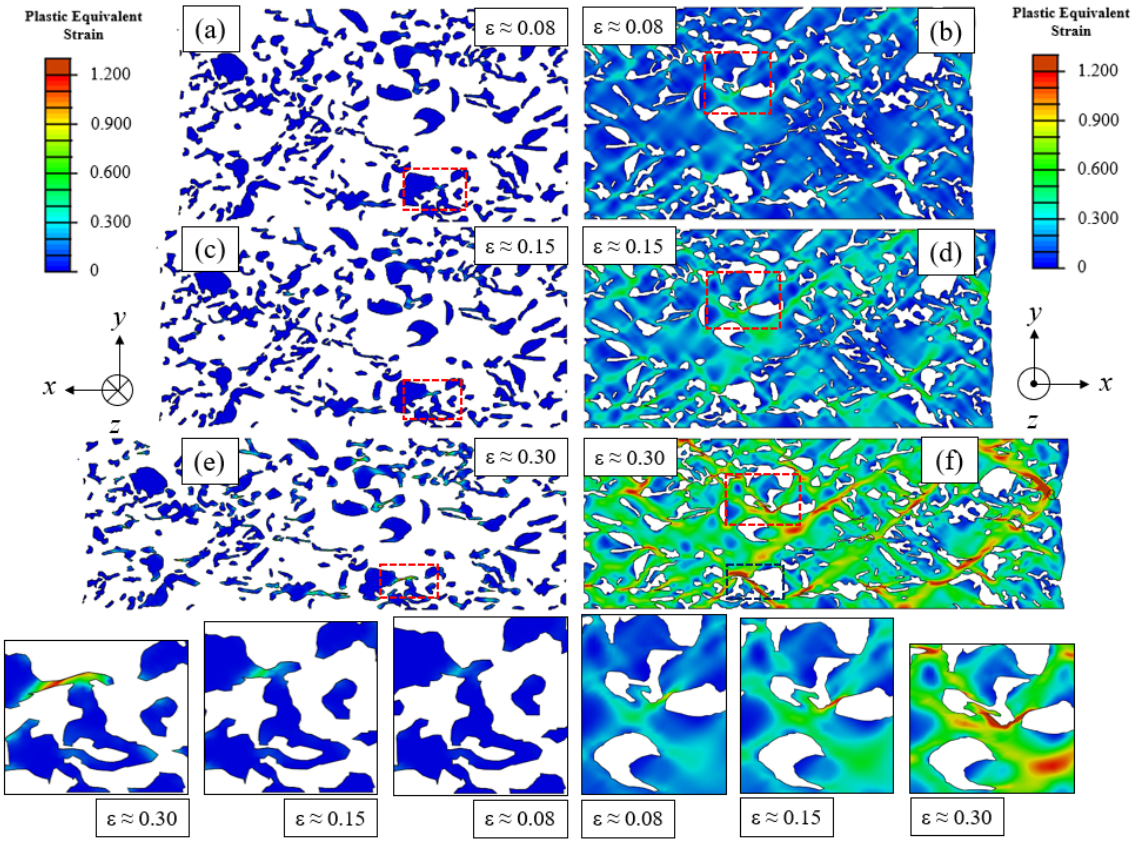

Figure 55 – Plastic equivalent strain in (left) martensite and (right) ferrite. DP600, plane strain compression. Global plastic equivalent strain – (a) and (b): 0.08; (c) and (d): 0.15; (e) and (f): 0.30. Below: zoomed in views of (left) martensite and (right) ferrite.

Evidence of micro-shear bands can be spotted in the surface of the specimens, as shown in Figure 56, which compiles SE images of the pre-polished surface of strained specimens from Figure 50b and plastic strain maps from Figure 54.

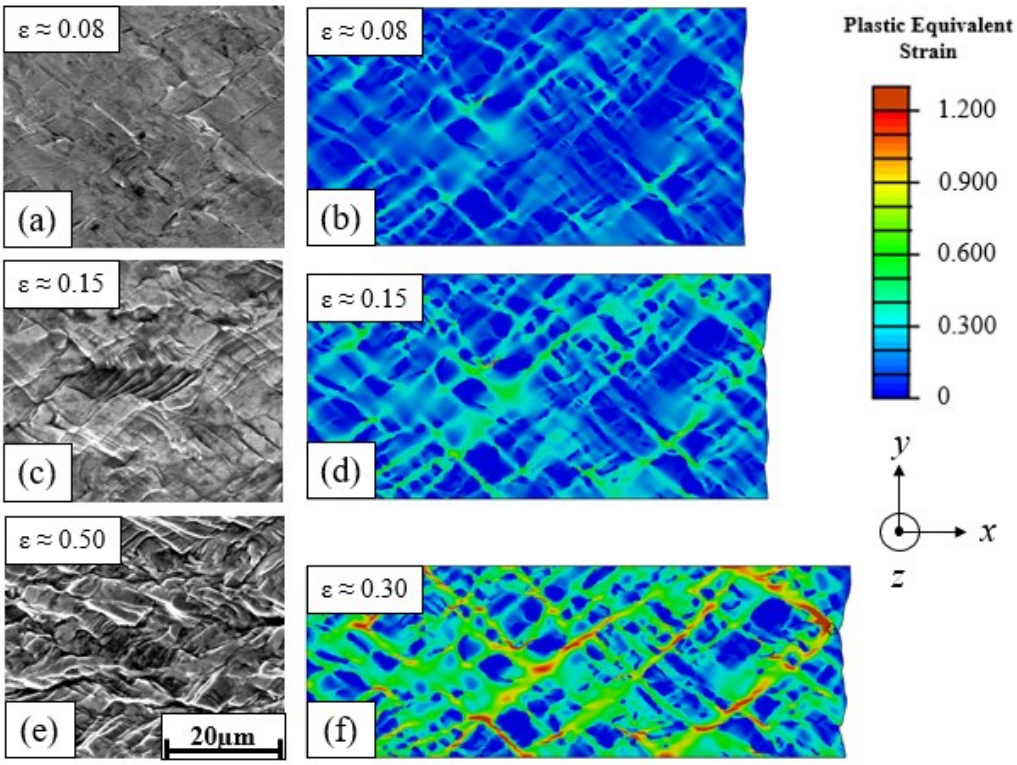

Figure 56 – Left: Pre-polished surface of plane strain compression strained specimens. Equivalent strains of (a) 0.08, (c) 0.15, and (e) 0.50. Right: plastic equivalent strain of 22.9% MVF – RVE for global equivalent strains of (b) 0.08, (d) 0.15, and (f) 0.30.

6- DISCUSSION

6.1- DUAL-PHASE BEHAVIOR UNDER LARGE STRAIN

As previously mentioned, the strain path of plane strain compression compared to uniaxial tension allows the achievement of significantly higher deformation levels. This is due to the hydrostatic stresses suppressing crack nucleation and propagation. The hardening behaviors observed in Figure 47 are similar until the onset of necking of the uniaxial tension specimen, which then fails to provide reliable information regarding the flow curve. Still, the dual-phase steel continues to deform up to $\varepsilon \approx 1.65$ without visible cracks. It therefore allows an investigation of the microstructural evolution in the same strain path encountered in cold rolling.

The approximately linear hardening behavior that follows the seemingly parabolic behavior could be simply attributed to friction effect, despite the pauses for re-lubrication. However, the IPFs (Figure 52, left) clearly indicate progressive increase in the density of high angle grain boundaries up to $\varepsilon \approx 0.50$. This could be due to the difficulty indexing overly strained regions. However, the KAM maps (Figure 52, right) reveal misoriented domains especially at the surroundings of the original grain boundaries. It may thus be

inferred that the progression of strain leads to increasing the number and misorientation of slip bands. Eventually, their mutual intersection leads to the development of new refined grains like in Severe Plastic Deformation (SPD) procedures such as Multi-Directional Forging [117–120], Equal-Channel Angular-Pressing [121], and High-Pressure Torsion [122].

This hypothesis is supported by KORZEKWA et al. [53] who, as previously mentioned, demonstrated the progression of dislocation arrangement under uniaxial tension for a DP steel by means of TEM. Figure 20 clearly shows the formation of dislocation tangles and developed cellular structure for a 7% true strain, which is much lower than the average 0.50 equivalent strain.

Although this level of strain may not suffice to promote considerable grain refinement through SPD processes, the FE model indicates that strains of more than 4 times the average values obtained using Equation 28 can be achieved within shear bands.

Further investigation is due since such grain refinement may result in promising bimodal grain structures and the necessary strain path can be achieved using conventional rolling facilities.

6.2- STRAIN PROGRESSION UNDER A FRACTAL PERSPECTIVE

The concept of fractal was proposed by Benoit Mandelbrot to encompass “disorder and cases of intractable irregularity” [8] observed in nature. Fractality is, according to the author, a measure of roughness. An example of this can be shown in the plasticity of solid structures. Bearing this in mind, a strain progression analysis under a fractal perspective aims at separating strain related phenomena according to their scale and stablishing the inter-relations between them.

Our analysis began with the larger scale phenomena represented by the superficial effects illustrated in Figure 48, and indirectly indicated by microhardness measurements in Figure 49. As previously described, these superficial effects are what we have defined as macro-scale shear bands (MSBs), and they originated from the stress concentrators in the corner regions of the die. Hence, these bands are there regardless of the dual-phase microstructure.

In a lower scale one may also observe in the pre-polished surface of the strained specimens (Figure 50) steps which become progressively more pronounced along with

straining. These steps originate both from dislocations in deformation bands within grains and also from small shear bands, which have been defined as micro-scale shear bands. These arise from the strain partitioning due to contrasting mechanical properties of the individual phases. This latter claim is backed by the numerical analysis which indicates this partitioning of strain in a representative volume element (Figures 55, 56, and 57) through a model that completely disregards grain orientation, grain boundary effects, and any other discontinuity or heterogeneity other than distribution and individual phase properties. Further discussion about the limitations of such simplifications in the numerical analysis will be made in the following section. At this point, it has to be stressed that these micro-scale shear bands are perhaps the most important manifestation linked to the behavior of dual-phase steels under different loading paths. On the one hand, micro-scaled shear bands are intimately associated with premature failure of these steels in stretch-flange operations, as evidenced by means of hole-expansion testing [5] or under a heterogeneous stress field, as highlighted by ZHENG et al. [96]. On the other, as reported in this work, under plane strain compression these bands may be associated with local grain refinement resulting in a bimodal grain distribution.

A summarizing schematic representation of the fractal analysis is presented in Figure 57.

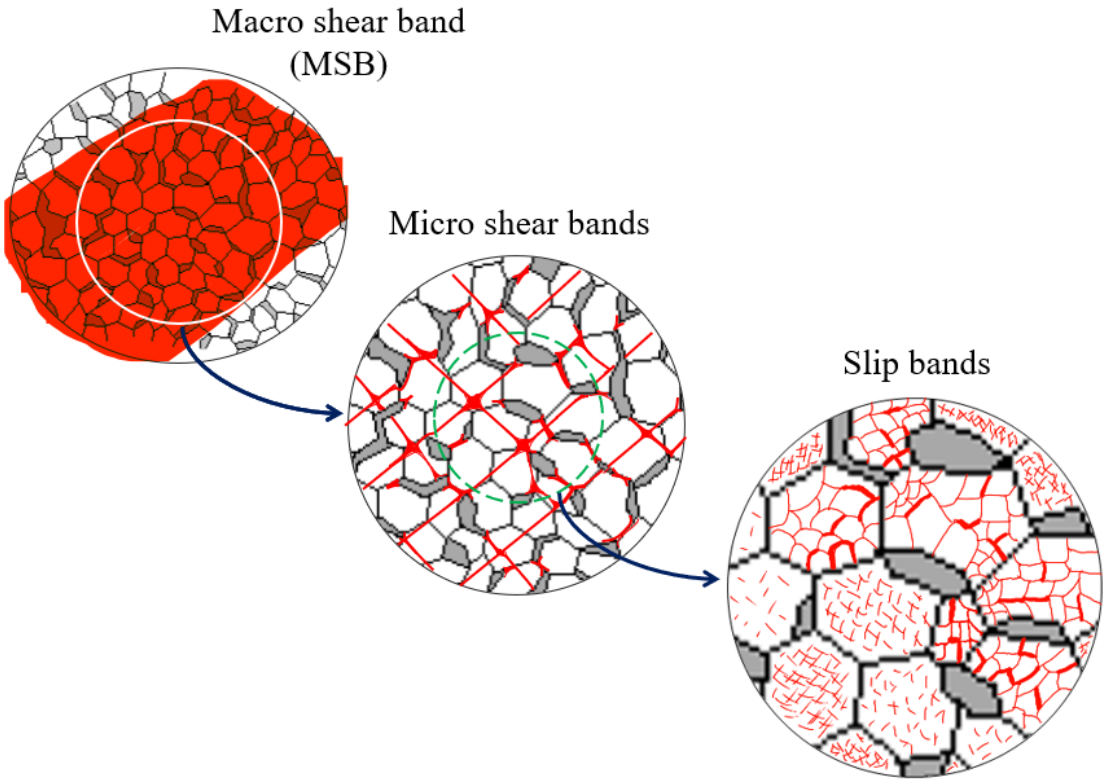

Figure 57 - Schematic representation of macro shear bands, micro shear bands and slip bands.

6.3- 2D-BASED RVE ANALYSIS

The 2D-based RVE approach in the study of strain partitioning, as previously described, relies on some fundamental assumptions which are known to be untrue. BONG et al. [93] highlighted the hypotheses that discrete interactions between defects can be disregarded, which is relevant, however is far from being the only simplification. These models are in fact fundamentally based on continuity. The only sources of discontinuity which approximate to the reality of the studied problem are the distinct properties attributed to the constituent phases, which thus encompasses distribution and morphology effect. Input flow curves are based on an averaged modeling of monophase alloys behavior. Still, the fact that a model is limited does not mean that it can't be useful. Simplifications are thoroughly necessary in the process of advancing the understanding in any field of knowledge. It should be stressed the need that these limitations are clarified, carefully considered along any analysis, and eliminated, when possible and necessary.

Having made these considerations, we may proceed to discussing the obtained results. Regarding the representativity of the volume element, usually, the dual-phase numerical flow curve is compared to the empirical one. It has been demonstrated that a representative volume element must have a similar phase fraction compared to the global proportion and the flow curve extraction method must represent the simulated volume element. The applied boundary conditions guarantee that the assessed field of view undergoes the same strain path as in the experiments. But the input flow curves were not empirically obtained and the presence of bainite and retained austenite was disregarded. Hence, for this comparison, one can only say that a combination of the input ferrite and martensite properties with a typical morphology of the studied steel and an approximate volume fraction renders a similar behavior under plane strain compression and uniaxial tension to the studied dual-phase steel. This is the farther we can go claiming numerical validity by such means. Further validation ought to be sought out from other empirical results.

As already mentioned, the effect of crystal plasticity, grain boundaries, and the actual progression of dislocation density increase and pile up in cells or planar structures is disregarded. So, the obtained results (such as the reasonable flow curve fitting) can only make sense if these variables and their fluctuation are not showing predominant effect in this scale of analysis. The term "fluctuation" is stressed here from a statistical perspective since it is related to structural discontinuity. Hence, the regions of strain concentration

observed in the FE model cannot be slip bands, even if they are within what would be a single a grain, because there is no such distinction. So, they ought to be shear bands. But their origin is linked to microscopic stress concentrators derived from morphology and different plastic properties between the constituent phases, thus making them micro-shear bands. These can be empirically verified, though indirectly, by their surface effects presented in Figure 50.

Furthermore, as indicated by typical IPFs from the EBSD analysis, it seems that grain orientation has little to no influence in determining domains of concentrating strain. Hence, the simplification of the RVE-FE model regarding grain orientation is more than justified. Also, the implicit assumption in the input flow curves and uniform behavior throughout the domain of each phase does not seem to impose any problem in the current analysis.

Therefore, considering the dominating micro-mechanisms in dual-phase strain progression and their correlation to macroscopic mechanical response under a non-cyclic monotonic loading path, the 2D-RVE-FEM approach has definitely not been exhausted by its limitations. The fundamental matter is that of properly situating the studied scale of analysis and outlining its borders regarding sub-micro phenomena, which would demand considering crystallography, grain boundaries, phase boundaries, and prior dislocation distribution among other factors in the numerical model.

7- CONCLUSÕES

Este trabalho é uma análise ampla da progressão de deformação de um aço *dual-phase* sob compressão no estado plano de deformação baseada em uma abordagem integrada empírica e numérica. A avaliação da progressão dos fenômenos associados à deformação foi feita sob uma perspectiva fractal. Em outras palavras, esses fenômenos foram estudados de acordo com sua escala dimensional com o objetivo de estabelecer como se relacionam na progressão da deformação. Uma análise por elementos finitos de uma região representativa foi utilizada e criticamente discutida elucidando limitações. As principais conclusões são enumeradas:

1. A análise fractal da compressão em estado plano de deformação do aço DP600 revela macro bandas de cisalhamento originadas de concentradores de tensão macroscópicos. Micro bandas de cisalhamento se formam principalmente dentro dessas bandas em decorrência de micro concentradores de tensão, como pontas de ilhas de martensita separadas por um pequeno domínio ferrítico.
2. Altos níveis de deformação atingidos na compressão em estado plano parecem indicar a ocorrência de refino de grão, como em processos de deformação severa. Isso pode ocorrer dentro de micro bandas de cisalhamento, nas quais, de acordo com o modelo numérico, valores 4 vezes maiores do que a deformação média da chapa podem ser atingidos. Destaca-se particular relevância a esse fenômeno, uma vez que refino de grão local pode resultar em distribuições bimodais com propriedades mecânicas economicamente interessantes. Além disso, o estado de deformação em estado plano de deformação pode ser obtido em instalações convencionais de laminação a frio.
3. A análise numérica baseada num campo visual bidimensional pode ser implementada com sucesso em uma escala acima da submicrométrica. O modelo prevê com sucesso a ocorrência de micro bandas de cisalhamento devido ao contraste entre as propriedades mecânicas das fases constituintes.

Essas observações são de caráter fundamental, podendo ser úteis para o processamento mecânico de aços *dual-phase* e para um melhor entendimento do comportamento dessas ligas em sua aplicação final.

7.1- CONCLUSIONS

This work is a thorough analysis of strain progression of a dual-phase steel under plane strain compression based on an integrated empirical and numerical approach. The assessment of strain related phenomena was structured from a fractal standpoint. In other words, these phenomena were studied according to their dimensional scale with the goal of establishing relationships between different scales of analysis. A 2D-based RVE-FE model was used and critically assessed. The main conclusions are outlined as follows:

- The fractal analysis of plane strain compression reveals that the strain progression of a DP600 shows macro shear bands originated from macroscopic stress concentrators. Micro-scaled shear bands are formed mostly within these bands from microscopic stress concentrators, such as acute martensite islands separated by a small ferritic domain.
- Large strains achieved by means of plane strain compression seems to lead to grain refinement as in SPD processes. It is proposed that this occurs within micro-shear bands, which can reach about 4 times the average strain values, according to the numerical model. This is particularly relevant since the local grain refinement may result in bimodal grain structures with promising mechanical properties. Also, the strain path of plane strain compression can be obtained in conventional rolling facilities.
- The 2D-based RVE-FE model can be successfully implemented in a scale of analysis above that of the submicrometric level. The model successfully predicts the formation of micro-shear bands due to the contrasting mechanical properties of ferrite and martensite domains.

These are fundamental insights, which can be useful in the processing of dual-phase steels, and that enhance the understanding of the mechanical behavior of these microstructures in their final use.

8- LIST OF REFERENCES

[1] R. Kuziak, R. Kawalla, S. Waengler, Advanced high strength steels for automotive industry: A review, Arch. Civ. Mech. Eng. 8 (2008) 103–117. https://doi.org/10.1016/s1644-9665(12)60197-6.

[2] C.C. Tasan, M. Diehl, D. Yan, M. Bechtold, F. Roters, L. Schemmann, C. Zheng, N. Peranio, D. Ponge, M. Koyama, K. Tsuzaki, D. Raabe, An Overview of Dual-Phase Steels: Advances in Microstructure-Oriented Processing and Micromechanically Guided Design, Annu. Rev. Mater. Res. 45 (2015) 391–431. https://doi.org/10.1146/annurev-matsci-070214-021103.

[3] C.C. Tasan, M. Diehl, D. Yan, C. Zambaldi, P. Shanthraj, F. Roters, D. Raabe, Integrated experimental-simulation analysis of stress and strain partitioning in multiphase alloys, Acta Mater. 81 (2014) 386–400. https://doi.org/10.1016/j.actamat.2014.07.071.

[4] A. Alaie, S. Ziaei Rad, J. Kadkhodapour, M. Jafari, M. Asadi Asadabad, S. Schmauder, Effect of microstructure pattern on the strain localization in DP600 steels analyzed using combined in-situ experimental test and numerical simulation, Mater. Sci. Eng. A. 638 (2015) 251–261. https://doi.org/10.1016/j.msea.2015.04.071.

[5] J.H. Kim, M.G. Lee, D. Kim, D.K. Matlock, R.H. Wagoner, Hole-expansion formability of dual-phase steels using representative volume element approach with boundary-smoothing technique, Mater. Sci. Eng. A. 527 (2010) 7353–7363. https://doi.org/10.1016/j.msea.2010.07.099.

[6] G. Cheng, K.S. Choi, X. Hu, X. Sun, Predicting Deformation Limits of Dual-Phase Steels Under Complex Loading Paths, Jom. 69 (2017) 1046–1051. https://doi.org/10.1007/s11837-017-2333-7.

[7] P.B. Barcelos, Análise da Conformabilidade do Aço Ferrita Bainita, Comparativamente aos Aços Dual Phase e Microligado das Classes de 600MPa de Limite de Resistência., Federal University of Minas Gerais, 2019. http://hdl.handle.net/1843/31434.

[8] B.B. Mandelbrot, The Fractal Geometry of Nature, Henry Holt and Company, 1983.

[9] T.B. Hilditch, T. de Souza, P.D. Hodgson, Properties and automotive applications of advanced high-strength steels (AHSS), in: Weld. Join. Adv. High Strength Steels, Elsevier Ltd, 2015: pp. 9–28. https://doi.org/10.1016/B978-0-85709-436-0.00002-3.

[10] C.M. Tamarelli, AHSS 101: The Evolving Use of Advanced High-Strength Steels for Automotive Applications, 2011.

[11] S. Keeler, M. Kimchi, P.J. Mooney, Advanced High-Strength Steels Guidelines Version 6.0, 2017. https://www.worldautosteel.org/projects/advanced-high-strength-steel-application-guidelines/.

[12] J.G. Speer, F.C. Rizzo Assunção, D.K. Matlock, D. V. Edmonds, The "quenching and partitioning" process: Background and recent progress, Mater. Res. 8 (2005) 417–423. https://doi.org/10.1590/S1516-14392005000400010.

[13] O. Bouaziz, H. Zurob, M. Huang, Driving force and logic of development of advanced high strength steels for automotive applications, Steel Res. Int. 84 (2013) 937–947. https://doi.org/10.1002/srin.201200288.

[14] H.K.D.H. HONEYCOMBE, R.W.K. BHADESHIA, Steels: Microstructure and Properties, 3rd ed., Elsevier Ltd, 2006.

[15] M.S. Rashid, Dual Phase Steels, Ann. Rev. Mater. Sci. 11 (1981) 245–66. www.annualreviews.org.

[16] N.J. Kim, G. Thomas, Effects of morphology on the mechanical behavior of a dual phase Fe/2Si/0.1C steel, Metall. Trans. A. 12 (1981) 483–489. https://doi.org/10.1007/BF02648546.

[17] A. Bag, K.K. Ray, E.S. Dwarakadasa, Influence of martensite content and morphology on the toughness and fatigue behavior of high-martensite dual-phase steels, Metall. Mater. Trans. A. 30 (1999) 1193–1202. https://doi.org/10.1007/s11661-001-0196-5.

[18] D. Das, P.P. Chattopadhyay, Influence of martensite morphology on the work-hardening behavior of high strength ferrite-martensite dual-phase steel, J. Mater. Sci. 44 (2009) 2957–2965. https://doi.org/10.1007/s10853-009-3392-0.

[19] J. Zhang, H. Di, Y. Deng, R.D.K. Misra, Effect of martensite morphology and

volume fraction on strain hardening and fracture behavior of martensite-ferrite dual phase steel, Mater. Sci. Eng. A. 627 (2015) 230–240. https://doi.org/10.1016/j.msea.2015.01.006.

[20] S. Sun, M. Pugh, Manganese partitioning in dual-phase steel during annealing, Mater. Sci. Eng. A. 276 (2000) 167–174. https://doi.org/10.1016/s0921-5093(99)00261-0.

[21] C. Tamura, I. Sekine, H. Tanaka, T. Ouchi, Thermomechanical Processing of High-Strength Low-Alloy Steels, Butterworth & Co., 1988. https://doi.org/10.1016/c2013-0-04163-1.

[22] D.H. Shin, W.G. Kim, J.Y. Ahn, K.T. Park, Y.S. Kim, Ultrafine Grained Dual Phase Steels Fabricated by Equal Channel Angular Pressing, Mater. Sci. Forum. 503–504 (2006) 447–454. https://doi.org/10.4028/www.scientific.net/msf.503-504.447.

[23] P. Movahed, S. Kolahgar, S.P.H. Marashi, M. Pouranvari, N. Parvin, The effect of intercritical heat treatment temperature on the tensile properties and work hardening behavior of ferrite-martensite dual phase steel sheets, Mater. Sci. Eng. A. 518 (2009) 1–6. https://doi.org/10.1016/j.msea.2009.05.046.

[24] R.G. Davies, Influence of martensite composition and content on the properties of dual phase steels, Metall. Trans. A. 9 (1978) 671–679. https://doi.org/10.1007/BF02659924.

[25] M. Calcagnotto, D. Ponge, D. Raabe, Ultrafine grained ferrite/martensite dual phase steel fabricated by large strain warm deformation and subsequent intercritical annealing, ISIJ Int. 48 (2008) 1096–1101. https://doi.org/10.2355/isijinternational.48.1096.

[26] M. Asadi, B.C. De Cooman, H. Palkowski, Influence of martensite volume fraction and cooling rate on the properties of thermomechanically processed dual phase steel, Mater. Sci. Eng. A. 538 (2012) 42–52. https://doi.org/10.1016/j.msea.2012.01.010.

[27] H. Ashrafi, M. Shamanian, R. Emadi, N. Saeidi, Correlation of Tensile Properties and Strain Hardening Behavior with Martensite Volume Fraction in Dual-Phase Steels, Trans. Indian Inst. Met. 70 (2017) 1575–1584.

https://doi.org/10.1007/s12666-016-0955-z.

[28] A.R. Marder, Deformation characteristics of dual-phase steels, Metall. Trans. A. 13 (1982) 85–92. https://doi.org/10.1007/BF02642418.

[29] C. Peng-Heng, A.G. Preban, The effect of ferrite grain size and martensite volume fraction on the tensile properties of dual phase steel, Acta Metall. 33 (1985) 897–903. https://doi.org/10.1016/0001-6160(85)90114-2.

[30] Z. Jiang, Z. Guan, J. Lian, Effects of microstructural variables on the deformation behaviour of dual-phase steel, Mater. Sci. Eng. A. 190 (1995) 55–64. https://doi.org/10.1016/0921-5093(94)09594-M.

[31] G. Rosenberg, I. Sinaiová, Ľ. Juhar, Effect of microstructure on mechanical properties of dual phase steels in the presence of stress concentrators, Mater. Sci. Eng. A. 582 (2013) 347–358. https://doi.org/10.1016/j.msea.2013.06.035.

[32] M.D. Zhang, J. Hu, W.Q. Cao, H. Dong, Microstructure and mechanical properties of high strength and high toughness micro-laminated dual phase steels, Mater. Sci. Eng. A. 618 (2014) 168–175. https://doi.org/10.1016/j.msea.2014.08.073.

[33] Q. Lai, L. Brassart, O. Bouaziz, M. Gouné, M. Verdier, G. Parry, A. Perlade, Y. Bréchet, T. Pardoen, Influence of martensite volume fraction and hardness on the plastic behavior of dual-phase steels: Experiments and micromechanical modeling, Int. J. Plast. 80 (2016) 187–203. https://doi.org/10.1016/j.ijplas.2015.09.006.

[34] M. Sarwar, R. Priestner, Influence of ferrite-martensite microstructural morphology on tensile properties of dual-phase steel, J. Mater. Sci. 31 (1996) 2091–2095. https://doi.org/10.1007/BF00356631.

[35] L.F. Ramos, D.K. Matlock, G. Krauss, On the deformation behavior of dual-phase steels, Metall. Trans. A. 10 (1979) 259–261. https://doi.org/10.1007/BF02817636.

[36] Y. Bergström, Y. Granbom, D. Sterkenburg, A Dislocation-Based Theory for the Deformation Hardening Behavior of DP Steels: Impact of Martensite Content and Ferrite Grain Size, J. Metall. 2010 (2010) 1–16.

https://doi.org/10.1155/2010/647198.

[37] E. Ahmad, T. Manzoor, K.L. Ali, J.I. Akhter, Effect of microvoid formation on the tensile properties of dual-phase steel, J. Mater. Eng. Perform. 9 (2000) 306–310. https://doi.org/10.1361/105994900770345962.

[38] A.F. SZEWCZYK, J. GURLAND, Study of the Deformation and Fracture of a Dual-Phase Steel., Met. Trans A. V 13A (1982) 1821–1826. https://doi.org/10.1007/bf02647838.

[39] P. Tsipouridis, L. Koll, C. Krempaszky, E. Werner, On the strength of grain and phase boundaries in ferritic-martensitic dual-phase steels, Int. J. Mater. Res. 102 (2011) 674–686. https://doi.org/10.3139/146.110519.

[40] H. Ghassemi-Armaki, R. Maaß, S.P. Bhat, S. Sriram, J.R. Greer, K.S. Kumar, Deformation response of ferrite and martensite in a dual-phase steel, Acta Mater. 62 (2014) 197–211. https://doi.org/10.1016/j.actamat.2013.10.001.

[41] K.T. Park, Y.K. Lee, D.H. Shin, Fabrication of ultrafine grained ferrite/martensite dual phase steel by severe plastic deformation, ISIJ Int. 45 (2005) 750–755. https://doi.org/10.2355/isijinternational.45.750.

[42] H. Azizi-Alizamini, M. Militzer, W.J. Poole, Formation of ultrafine grained dual phase steels through rapid heating, ISIJ Int. 51 (2011) 958–964. https://doi.org/10.2355/isijinternational.51.958.

[43] M.P. Rao, V.S. Sarma, S. Sankaran, Development of high strength and ductile ultra fine grained dual phase steel with nano sized carbide precipitates in a V-Nb microalloyed steel, Mater. Sci. Eng. A. 568 (2013) 171–175. https://doi.org/10.1016/j.msea.2012.12.084.

[44] A. Karmakar, A. Karani, S. Patra, D. Chakrabarti, Development of bimodal ferrite-grain structures in low-carbon steel using rapid intercritical annealing, Metall. Mater. Trans. A Phys. Metall. Mater. Sci. 44 (2013) 2041–2052. https://doi.org/10.1007/s11661-012-1556-z.

[45] M. Papa Rao, V. Subramanya Sarma, S. Sankaran, Processing of Bimodal Grain-Sized Ultrafine-Grained Dual Phase Microalloyed V-Nb Steel with 1370 MPa Strength and 16 pct Uniform Elongation Through Warm Rolling and Intercritical

Annealing, Metall. Mater. Trans. A Phys. Metall. Mater. Sci. 45 (2014) 5313–5317. https://doi.org/10.1007/s11661-014-2478-8.

[46] E.O. Hall, The deformation and ageing of mild steel: II Characteristics of the Lüders deformation, Proc. Phys. Soc. Sect. B. 64 (1951) 742–747. https://doi.org/10.1088/0370-1301/64/9/302.

[47] N.J. Petch, The cleavage strength of polycrystals, J. Iron Steel Inst. 174 (1953) 25–28. https://doi.org/10.1007/BF01972547.

[48] M. Calcagnotto, D. Ponge, E. Demir, D. Raabe, Orientation gradients and geometrically necessary dislocations in ultrafine grained dual-phase steels studied by 2D and 3D EBSD, Mater. Sci. Eng. A. 527 (2010) 2738–2746. https://doi.org/10.1016/j.msea.2010.01.004.

[49] M. Sarwar, E. Ahmad, K.A. Qureshi, T. Manzoor, Influence of epitaxial ferrite on tensile properties of dual phase steel, Mater. Des. 28 (2007) 335–340. https://doi.org/10.1016/j.matdes.2005.05.019.

[50] F. Ebrahimi, N. Saeidi, M. Raeissi, Microstructural Modifications of Dual-Phase Steels: An Overview of Recent Progress and Challenges, Steel Res. Int. 91 (2020). https://doi.org/10.1002/srin.202000178.

[51] M.F. Ashby, The deformation of plastically non-homogeneous materials, Philos. Mag. A J. Theor. Exp. Appl. Phys. 21 (1970) 399–424. https://doi.org/10.1080/14786437008238426.

[52] D.A. Korzekwa, R.D. Lawson, D.K. Matlock, G. Krauss, Consideration of Models Describing the Strength and Ductility of Dual-Phase Steels., Scr. Metall. 14 (1980) 1023–1028. https://doi.org/10.1016/0036-9748(80)90379-8.

[53] D.A. Korzekwa, D.K. Matlock, G. Krauss, Dislocation substructure as a function of strain in a dual-phase steel, Metall. Trans. A. 15 (1984) 1221–1228. https://doi.org/10.1007/BF02644716.

[54] H. Mughrabi, Dual role of deformation-induced geometrically necessary dislocations with respect to lattice plane misorientations and/or long-range internal stresses, Acta Mater. 54 (2006) 3417–3427. https://doi.org/10.1016/j.actamat.2006.03.047.

[55] J. Kadkhodapour, S. Schmauder, D. Raabe, S. Ziaei-Rad, U. Weber, M. Calcagnotto, Experimental and numerical study on geometrically necessary dislocations and non-homogeneous mechanical properties of the ferrite phase in dual phase steels, Acta Mater. 59 (2011) 4387–4394. https://doi.org/10.1016/j.actamat.2011.03.062.

[56] Z. Fan, Microstructure and Mechanical Properties of Multiphase Materials, University of Surrey, 1993.

[57] S.T. Mileiko, The tensile strength and ductility of continuous fibre composites, J. Mater. Sci. 4 (1969) 974–977. https://doi.org/10.1007/BF00555312.

[58] H.K.D.H. Bhadeshia, D. V. Edmonds, Analysis of mechanical properties and microstructure of high-silicon dual-phase steel, Met. Sci. 14 (1980) 41–49. https://doi.org/10.1179/030634580790426328.

[59] N.C. Goel, S. Sangal, K. Tangri, A theoretical model for the flow behavior of commercial dual-phase steels containing metastable retained austenite: Part I. derivation of flow curve equations, Metall. Trans. A. 16 (1985) 2013–2021. https://doi.org/10.1007/BF02662402.

[60] S. Kuang, Y. lin Kang, H. Yu, R. dong Liu, Stress-strain partitioning analysis of constituent phases in dual phase steel based on the modified law of mixture, Int. J. Miner. Metall. Mater. 16 (2009) 393–398. https://doi.org/10.1016/S1674-4799(09)60070-4.

[61] Y. Tomota, K. Kuroki, T. Mori, I. Tamura, Tensile deformation of two-ductile-phase alloys: Flow curves of α-γ FeCrNi alloys, Mater. Sci. Eng. 24 (1976) 85–94. https://doi.org/10.1016/0025-5416(76)90097-5.

[62] H. Hollomon, Tensile deformation., Aime Trans ,. 12 (1945) 1–22,.

[63] P. Ludwik, Elemente der Technologischen Mechanik, Springer Berlin Heidelberg GmbH, Berlin, Heidelberg, 1909. https://doi.org/10.1007/978-3-662-40293-1.

[64] H.W. Swift, Plastic instability under plane stress, J. Mech. Phys. Solids. 1 (1952) 1–18. https://doi.org/10.1016/0022-5096(52)90002-1.

[65] E. Voce, The relationship between stress and strain for homogeneous deformations, J Inst Met. 74 (1948) 537–562.

[66] C. Crussard, B. Jaoul, Contribution à l'étude de la forme des courbes de traction des métaux et à son interprétation physique, Rev. Métallurgie. 47 (1950) 589–600. https://doi.org/10.1051/metal/195047080589.

[67] B. Jaoul, Etude de la forme des courbes de deformation plastique, J. Mech. Phys. Solids. 5 (1957) 95–114.

[68] A. Gouldstone, N. Chollacoop, M. Dao, J. Li, A.M. Minor, Y.L. Shen, Indentation across size scales and disciplines: Recent developments in experimentation and modeling, Acta Mater. 55 (2007) 4015–4039. https://doi.org/10.1016/j.actamat.2006.08.044.

[69] M. Delincé, P.J. Jacques, T. Pardoen, Separation of size-dependent strengthening contributions in fine-grained Dual Phase steels by nanoindentation, Acta Mater. 54 (2006) 3395–3404. https://doi.org/10.1016/j.actamat.2006.03.031.

[70] M.D. Taylor, K.S. Choi, X. Sun, D.K. Matlock, C.E. Packard, L. Xu, F. Barlat, Correlations between nanoindentation hardness and macroscopic mechanical properties in DP980 steels, Mater. Sci. Eng. A. 597 (2014) 431–439. https://doi.org/10.1016/j.msea.2013.12.084.

[71] G. Cheng, F. Zhang, A. Ruimi, D.P. Field, X. Sun, Quantifying the effects of tempering on individual phase properties of DP980 steel with nanoindentation, Mater. Sci. Eng. A. 667 (2016) 240–249. https://doi.org/10.1016/j.msea.2016.05.011.

[72] A.H. Jahanara, Y. Mazaheri, M. Sheikhi, Correlation of ferrite and martensite micromechanical behavior with mechanical properties of ultrafine grained dual phase steels, Mater. Sci. Eng. A. 764 (2019) 138206. https://doi.org/10.1016/j.msea.2019.138206.

[73] J. Choi, B.W. Seo, D.H. Yoo, J.Y. Jang, Predicting macroscopic plastic flow of high-performance, dual-phase steel through spherical nanoindentation on each microphase, J. Mater. Res. 24 (2009) 816–822.

[74] F. Zhang, A. Ruimi, P.C. Wo, D.P. Field, Morphology and distribution of martensite in dual phase (DP980) steel and its relation to the multiscale mechanical behavior, Mater. Sci. Eng. A. 659 (2016) 93–103. https://doi.org/10.1016/j.msea.2016.02.048.

[75] G. Sundararajan, M. Roy, Hardness Testing, in: P.V. K.H. Jürgen Buschow, Robert W. Cahn, Merton C. Flemings, Bernhard Ilschner, Edward J. Kramer, Subhash Mahajan (Ed.), Encycl. Mater. Sci. Technol., Second, Elsevier, 2001: pp. 3728–3736. https://doi.org/https://doi.org/10.1016/B0-08-043152-6/00665-3.

[76] E. Werner, W. Prantl, Slip transfer across grain and phase boundaries, Acta Metall. Mater. 38 (1990) 533–537. https://doi.org/10.1016/0956-7151(90)90159-E.

[77] D. Tabor, The Hardness of Metals, Oxford University Press, London, 1951.

[78] W.C. Oliver, G.M. Pharr, Measurement of hardness and elastic modulus by instrumented indentation: Advances in understanding and refinements to methodology, J. Mater. Res. 19 (2004) 3–20. https://doi.org/10.1557/jmr.2004.19.1.3.

[79] K.L. Johnson, The correlation of indentation experiments, J. Mech. Phys. Solids. 18 (1970) 115–126. https://doi.org/10.1016/0022-5096(70)90029-3.

[80] W.D. Nix, H. Gao, Indentation size effects in crystalline materials: A law for strain gradient plasticity, J. Mech. Phys. Solids. 46 (1998) 411–425. https://doi.org/10.1016/S0022-5096(97)00086-0.

[81] G. Cheng, K.S. Choi, X. Hu, X. Sun, Determining individual phase properties in a multi-phase Q&P steel using multi-scale indentation tests, Mater. Sci. Eng. A. 652 (2016) 384–395. https://doi.org/10.1016/j.msea.2015.11.072.

[82] R. Rodríguez, I. Gutierrez, Correlation between nanoindentation and tensile properties influence of the indentation size effect, Mater. Sci. Eng. A. 361 (2003) 377–384. https://doi.org/10.1016/S0921-5093(03)00563-X.

[83] J.L. Bucaille, S. Stauss, E. Felder, J. Michler, Determination of plastic properties of metals by instrumented indentation using different sharp indenters, Acta Mater. 51 (2003) 1663–1678. https://doi.org/10.1016/S1359-6454(02)00568-2.

[84] O.R. Jardim, W.P. Longo, K.K. Chawla, Fracture behavior of a tempered dual phase steel, Metallography. 17 (1984) 123–130. https://doi.org/10.1016/0026-0800(84)90016-8.

[85] A. Neumaier, Mathematical Model Building, in: J. Pardalos, Panos M. Hearn,

Donald W. KALLRATH (Ed.), Model. Lang. Math. Optim., 1st ed., Kluwer Academic Publishers, 2004: pp. 37–43. https://doi.org/10.1007/978-1-4613-0215-5.

[86] S.S.L. G. R. QUEK, The Finite Element Method: A practical course, 1st ed., Elsevier Science Ltd., 2003. https://www.sciencedirect.com/book/9780080983561/the-finite-element-method.

[87] K.J. Bathe, Finite Element Procedures, 2nd ed., Prentice Hall, Pearson Education, Inc., Watertown, 1996. http://www.amazon.com/Finite-Element-Procedures-Part-1-2/dp/0133014584.

[88] F. Roters, P. Eisenlohr, T.. Bieler, D. Raabe, Crystal Plasticity Finite Element Methods, WILEY-VCH Verlag GmbH & Co. KGaA, 2010.

[89] A.R. Khoei, Extended Finite Element Method, John Wiley & Sons, Ltd., 2015.

[90] R. Hill, Elastic properties of reinforced solids: Some theoretical principles, J. Mech. Phys. Solids. 11 (1963) 357–372. https://doi.org/10.1016/0022-5096(63)90036-X.

[91] A. Ramazani, K. Mukherjee, U. Prahl, W. Bleck, Modelling the effect of microstructural banding on the flow curve behaviour of dual-phase (DP) steels, Comput. Mater. Sci. 52 (2012) 46–54. https://doi.org/10.1016/j.commatsci.2011.05.041.

[92] J. Zhou, A.M. Gokhale, A. Gurumurthy, S.P. Bhat, Realistic microstructural RVE-based simulations of stress-strain behavior of a dual-phase steel having high martensite volume fraction, Mater. Sci. Eng. A. 630 (2015) 107–115. https://doi.org/10.1016/j.msea.2015.02.017.

[93] H.J. Bong, H. Lim, M.G. Lee, D.T. Fullwood, E.R. Homer, R.H. Wagoner, An RVE procedure for micromechanical prediction of mechanical behavior of dual-phase steel, Mater. Sci. Eng. A. 695 (2017) 101–111. https://doi.org/10.1016/j.msea.2017.04.032.

[94] N.H. Abid, R.K. Abu Al-Rub, A.N. Palazotto, Micromechanical finite element analysis of the effects of martensite particle size and ferrite grain boundaries on the overall mechanical behavior of dual phase steel, J. Eng. Mater. Technol. 139

(2017). https://doi.org/10.1115/1.4036687.

[95] G.C. Barbosa, L.P. Moreira, L.B. da Silveira, F.R.F. da Silva, M.C. Cardoso, Micromechanical modeling of dual-phase dp600 steel sheet plastic behavior based on a representative volume element defined from the real microstructure, Mater. Sci. Forum. 930 MSF (2018) 293–298. https://doi.org/10.4028/www.scientific.net/MSF.930.293.

[96] X. Zheng, H. Ghassemi-Armaki, A. Srivastava, Structural and microstructural influence on deformation and fracture of dual-phase steels, Mater. Sci. Eng. A. 774 (2020) 138924. https://doi.org/10.1016/j.msea.2020.138924.

[97] J.H. Kim, M.G. Lee, R.H. Wagoner, A boundary smoothing algorithm for image-based modeling and its application to micromechanical analysis of multi-phase materials, Comput. Mater. Sci. 47 (2010) 785–795. https://doi.org/10.1016/j.commatsci.2009.11.004.

[98] S. Li, C. Guo, L. Hao, Y. Kang, Y. An, Microstructure-Based Modeling of Mechanical Properties and Deformation Behavior of DP600 Dual Phase Steel, Steel Res. Int. 90 (2019) 1–10. https://doi.org/10.1002/srin.201900311.

[99] A.C.E. Reid, S.A. Langer, R.C. Lua, V.R. Coffman, S.I. Haan, R.E. García, Image-based finite element mesh construction for material microstructures, Comput. Mater. Sci. 43 (2008) 989–999. https://doi.org/10.1016/j.commatsci.2008.02.016.

[100] N.H. Abid, R.K. Abu Al-Rub, A.N. Palazotto, Micromechanical Finite Element Analysis of the Effects of Martensite Particle Size and Ferrite Grain Boundaries on the Overall Mechanical Behavior of Dual Phase Steel, J. Eng. Mater. Technol. 139 (2017). https://doi.org/10.1115/1.4036687.

[101] B. Karlsson, B.O. Sundström, Inhomogeneity in plastic deformation of two-phase steels, Mater. Sci. Eng. 16 (1974) 161–168. https://doi.org/10.1016/0025-5416(74)90150-5.

[102] V. Uthaisangsuk, U. Prahl, W. Bleck, Stretch-flangeability characterisation of multiphase steel using a microstructure based failure modelling, Comput. Mater. Sci. 45 (2009) 617–623. https://doi.org/10.1016/j.commatsci.2008.06.024.

[103] S. Sodjit, V. Uthaisangsuk, Microstructure based prediction of strain hardening behavior of dual phase steels, Mater. Des. 41 (2012) 370–379. https://doi.org/10.1016/j.matdes.2012.05.010.

[104] A. Ramazani, A. Schwedt, A. Aretz, U. Prahl, W. Bleck, Characterization and modelling of failure initiation in DP steel, Comput. Mater. Sci. 75 (2013) 35–44. https://doi.org/10.1016/j.commatsci.2013.04.001.

[105] A. Ramazani, K. Mukherjee, H. Quade, U. Prahl, W. Bleck, Correlation between 2D and 3D flow curve modelling of DP steels using a microstructure-based RVE approach, Mater. Sci. Eng. A. 560 (2013) 129–139. https://doi.org/10.1016/j.msea.2012.09.046.

[106] O. Çavuşoğlu, S. Toros, H. Gürün, Microstructure based modelling of stress–strain relationship on dual phase steels, Ironmak. Steelmak. 46 (2019) 313–319. https://doi.org/10.1080/03019233.2017.1371959.

[107] R. Rodriguez, I. Gutierrez, Unified formulation to predict the tensile curves of steels with different microstructures, Mater. Sci. Forum. 426–432 (2003) 4525–4530. https://doi.org/10.4028/www.scientific.net/msf.426-432.4525.

[108] G. Nolze, R. Hielscher, Orientations - Perfectly colored, J. Appl. Crystallogr. 49 (2016) 1786–1802. https://doi.org/10.1107/S1600576716012942.

[109] F. Bachmann, R. Hielscher, H. Schaeben, Texture analysis with MTEX- Free and open source software toolbox, Solid State Phenom. 160 (2010) 63–68. https://doi.org/10.4028/www.scientific.net/SSP.160.63.

[110] K. Madhavan, L. Zentner, V. Farnsworth, S. Shivarajapura, M. Zentner, N. Denny, G. Klimeck, NanoHUB.org: Cloud-based services for nanoscale modeling, simulation, and education, Nanotechnol. Rev. 2 (2013) 107–117. https://doi.org/10.1515/ntrev-2012-0043.

[111] Abaqus, Abaqus 6.11 User Manual, IV (2013).

[112] U.F. Kocks, H. Mecking, Physics and phenomenology of strain hardening: The FCC case, Prog. Mater. Sci. 48 (2003) 171–273. https://doi.org/10.1016/S0079-6425(02)00003-8.

[113] L.R.C. Malheiros, E.A.P. Rodriguez, A. Arlazarov, Mechanical behavior of

tempered martensite: Characterization and modeling, Mater. Sci. Eng. A. 706 (2017) 38–47. https://doi.org/10.1016/j.msea.2017.08.089.

[114] I. Gutierrez, Modelling the Mechanical Behaviour of Steels with Mixed Microstructures, Metal. J. Metall. 11 (2005) 201–214.

[115] U.L. S. V. Parker, J. Wadsworth, I. Gutiérrez, R. Rodríguez, L. Vandenberghe, Property Models for Mixed Microstructures, Europace. (2003) 1–284.

[116] Q. Han, Y. Kang, P.D. Hodgson, N. Stanford, Quantitative measurement of strain partitioning and slip systems in a dual-phase steel, Scr. Mater. 69 (2013) 13–16. https://doi.org/10.1016/j.scriptamat.2013.03.021.

[117] N.G.S. Almeida, P.H.R. Pereira, C.G. De Faria, M.T.P. Aguilar, P.R. Cetlin, Mechanical behavior and microstructures of aluminum processed by low strain amplitude multi-directional confined forging, J. Mater. Res. Technol. 9 (2020) 3190–3197. https://doi.org/10.1016/j.jmrt.2020.01.065.

[118] P.C.A. Flausino, M.E.L. Nassif, F. de Castro Bubani, P.H.R. Pereira, M.T.P. Aguilar, P.R. Cetlin, Microstructural evolution and mechanical behavior of copper processed by low strain amplitude multi-directional forging, Mater. Sci. Eng. A. 756 (2019) 474–483. https://doi.org/10.1016/j.msea.2019.04.075.

[119] P.C.A. Flausino, M.E.L. Nassif, F. de C. Bubani, P.H.R. Pereira, M.T.P. Aguilar, P.R. Cetlin, Influence of Strain Amplitude on the Microstructural Evolution and Flow Properties of Copper Processed by Multidirectional Forging, Adv. Eng. Mater. 22 (2020) 1–13. https://doi.org/10.1002/adem.201901510.

[120] N.A. Neres da Silva, P.H.R. Pereira, E.C. Siqueira Corrêa, M.T. Paulino Aguilar, P.R. Cetlin, Microstructural evolution and mechanical properties in a Zn–Al–Cu–Mg hypoeutectic alloy processed by multi-directional forging at room temperature, Mater. Sci. Eng. A. 801 (2021). https://doi.org/10.1016/j.msea.2020.140420.

[121] R.Z. Valiev, T.G. Langdon, Principles of equal-channel angular pressing as a processing tool for grain refinement, Prog. Mater. Sci. 51 (2006) 881–981. https://doi.org/10.1016/j.pmatsci.2006.02.003.

[122] D. Geist, C. Rentenberger, H.P. Karnthaler, Extreme structural inhomogeneities

in high-pressure torsion samples along the axial direction, Acta Mater. 59 (2011) 4578–4586. https://doi.org/10.1016/j.actamat.2011.04.003.

APÊNDICE / APPENDIX

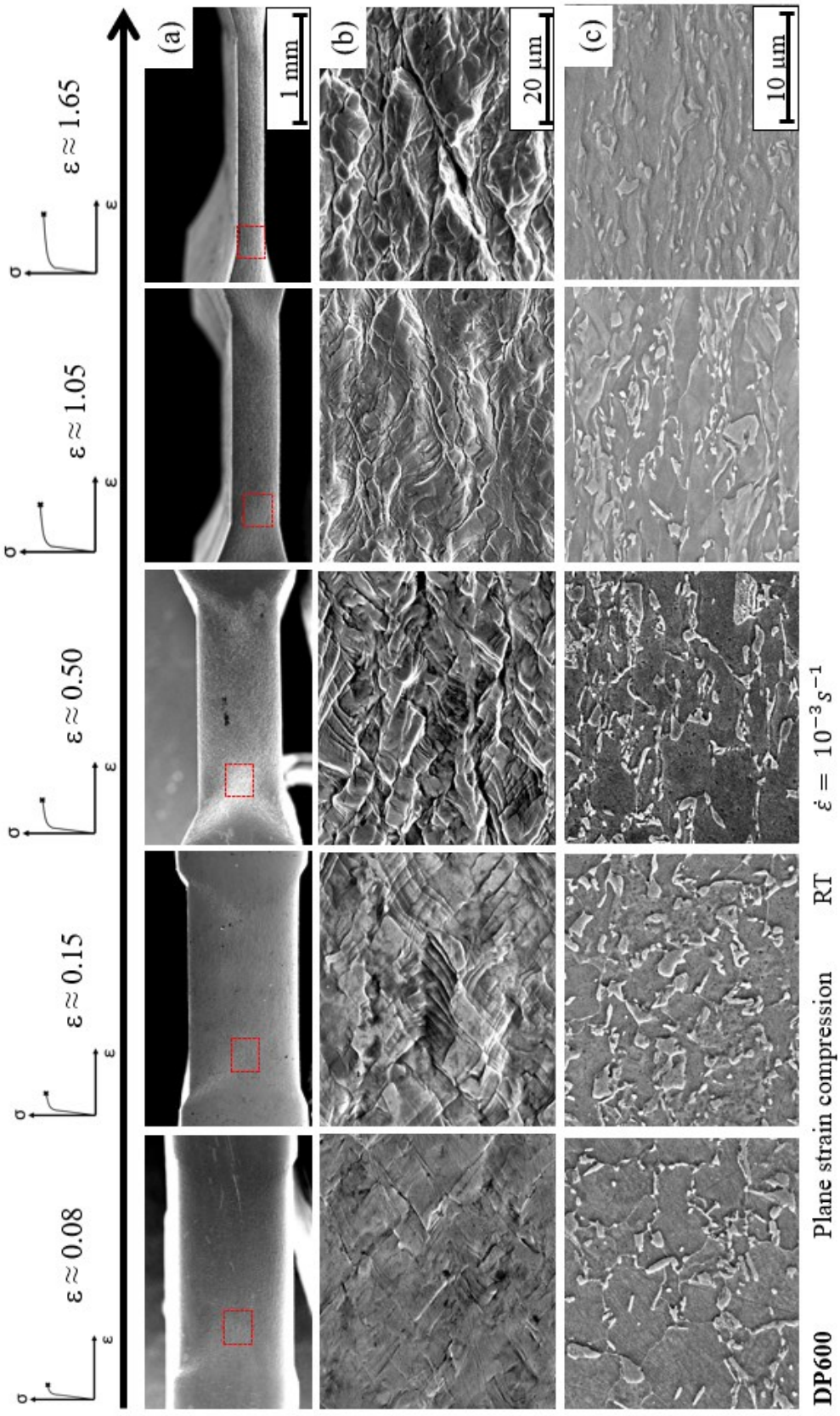

Ampliação da Figura 51 (Figure 51 magnified).